ABSTRACT

Title of Thesis: FABRICATION, WIND TUNNEL TESTING, AND FREEWHEELING ANALYSIS OF 4.75-FT DIAMETER COMPOSITE TILTROTOR BLADES
Amy Marie Morin,
Master of Science, 2021

Thesis Directed by: Professor Anubhav Datta
Department of Aerospace Engineering

The Maryland Tiltrotor Rig (MTR) is a new test facility for the development of next-generation high-speed tiltrotors. This thesis describes the development of the first set of Froude-scale tiltrotor blades for the MTR. The blades have a $-37°$ twist/span, a VR-7 profile, a D-spar, and $\pm 45°$ quasi-isotropic plies of carbon fiber. Titanium leading-edge weights bring the center of gravity to near the pitch axis at 0.25 c. The root cutout is until 0.263 R. The stiffness properties loosely follow the NASA-Bell XV-15 aircraft. The blades were instrumented and then integrated on the MTR in the Glenn L Martin Wind Tunnel and powered check out tests were conducted up to 2400 RPM ($M_{tip} = 0.53$) to test for tracking, balance, and structural integrity. Zero torque freewheeling tests were conducted to simulate future whirl flutter conditions. These tests produced 0-1500 RPM for $\theta_{75} = 0 - 8°$ at various tunnel speeds. A flexible flapping rotor analysis was developed to understand the freewheeling condition and to predict the test data. The freewheeling condition is unique to proprotors and is where wind tunnel tests are traditionally performed for

whirl flutter, so it was the principal focus of the analysis. Proprotor freewheeling, unlike helicopter autorotation, occurs at high inflow but zero thrust. There were two collectives for a given RPM, and it was discovered that the collectives tested during the initial check-out were the lower set of collectives, which was not representative of a full-scale tiltrotor in cruise. Thus, the analysis provided guidance for proper operating collectives in future tests. In addition, the low collective set provided a unique, interesting, and challenging validation case where the airfoils operated in negative stall. Accurate negative angle of attack stall data was crucial to predicting these collectives. It was shown that the in-house 2D C81 deck extracted with TURNS code in fact gave more consistent data predictions than the US government C81 deck from NASA Ames, likely due to differences in Reynolds number. The flexible flapping analysis also predicted blade bending moments and strains, but correlation with test data was cut short due to the COVID-19 shutdown. There is a vast and broad range of research to be conducted in the next five to ten years. It is hoped that the method developed and the blades fabricated here will provide a good baseline to assess all future advances.

FABRICATION, WIND TUNNEL TESTING, AND FREEWHEELING ANALYSIS OF 4.75-FT DIAMETER COMPOSITE TILTROTOR BLADES

by

Amy Marie Morin

Thesis submitted to the Faculty of the Graduate School of the
University of Maryland, College Park in partial fulfillment
of the requirements for the degree of
Master of Science
2021

Advisory Committee:
Professor Anubhav Datta, Advisor
Professor Inderjit Chopra
Professor James Baeder

© Copyright by
Amy Marie Morin
2021

Acknowledgments

I could not have completed this thesis and degree without the help of my fellow coworkers in the tiltrotor group, my supportive coworkers in the cube farm, my professors, and my advisor, Dr. Anubhav Datta. I cannot thank you all enough. Dr. Datta is a great professor and advisor who truly cares about his students, and I am very thankful for his continued support. I would also like to thank my other committee members, Dr. Inderjit Chopra and Dr. James Baeder, for the help I received both through classes and through research.

Additionally, I could not have made it through my degree without the emotional and moral support (and love) from my family and friends, both at home and at UMD. I am thankful for all of the dogs of coworkers and friends who have provided me with joy, and especially my own dog, Harley. I loved my time with the UMD Women's Ice Hockey team, and I loved being a part of Women in Aeronautics and Astronautics (WIAA). I was extremely proud to be a member of both, and I am so thankful for my teammates and club members for their continued friendships.

This work was carried out at the Alfred Gessow Rotorcraft Center, University of Maryland at College Park under the Army/Navy/NASA Vertical Lift Research Center of Excellence (VLRCOE) grant number W911W61120012 with technical monitoring from Dr Mahendra Bhagwat and POCs Tom Parham (Bell), Hyeonsoo Yeo (Army), Cecil Acree (NASA), and Wayne Johnson (NASA). Additional

funding for blade fabrication hardware was provided by Naval Air Warfare Center Aircraft Division (NAWCAD) seed grant with technical monitoring from Ronald Barry Walden (2018-2019). The carbon fiber material used to fabricate the blades were donated by the Boeing Company.

Table of Contents

List of Tables

List of Figures

Chapter 1: Introduction

The objective of this thesis is the fabrication of model-scale tiltrotor blades for testing on the Maryland Tiltrotor Rig (MTR). The University of Maryland has a long history of fabricating model-scale helicopter blades. But tiltrotor blades are special; they have high twist, and therefore require a different fabrication method. This thesis establishes that method.

1.1 Objectives

A new tiltrotor test facility is being developed at the University of Maryland: the Maryland Tiltrotor Rig (MTR). The purpose of this rig is to provide a test bed for basic research on the aeromechanics of high-speed tiltrotors. The vision for the future is to enable 400 kt flutter-free cruise with a turboprop-like thin wing (14% thickness to chord ratio) and a light-weight low-vibration high-performance proprotor. The vision for the MTR is to allow systematic parametric variation of blades, hub, and wing to enable that future. The dimensions are loosely 1/5.26 scale XV-15 or 1/8 V-22 even though the MTR is a research rig, not a scaled down version of a particular aircraft. This thesis is devoted to developing model-scale tiltrotor blades for this new rig.

Tiltrotors are a special class of aircraft driven by proprotors. Proprotors are not propellers; they allow blade flapping and cyclic controls to enable flight in helicopter mode. When tilted forward in cruise, they act as propellers, but the flapping motion introduces a special instability—whirl flutter. Proprotor whirl flutter is a phenomena unique to tiltrotors, with a mechanism distinct from classical propeller whirl flutter, with complex interplays of rotor flap and lag flexibility and the wing-pylon motion. Whirl flutter involves symmetric wing bending and torsion modes, hence a semi-span model suffices. The flutter speed is lower for a freewheeling rotor, so an unpowered model suffices; however, a powered model is needed for performance and loads in helicopter mode conversion flight. The MTR can operate in both powered and unpowered modes. A static tilt mechanism can tilt the pylon from 90° (helicopter mode) to 0° (airplane mode) at increments of 5° allowing testing in hover, conversion (steady state), and cruise. The freewheeling condition is unique to tiltrotor testing. The analysis portion of this thesis is therefore devoted to this condition.

The pre-COVID-19 plan also included wind tunnel testing of the blades as an objective. This plan had to be shelved for the future. Nevertheless, the fabricated blades were spun up to 2300 RPM at 55 knots during a loads check-out test in the Glenn L. Martin Wind Tunnel in September 2019. This test established the structural integrity of the blades. The limited freewheeling data obtained during the check-out test also proved quite valuable. The data and analysis developed revealed the correct collective range where flutter tests should be performed in the future. Thus, the fabrication of model-scale tiltrotor blades and explanation of

freewheeling are the principal contributions of this work.

1.2 Motivation

Over five decades of extensive research has converged today to a particular rotor and hub configuration. Modern tiltrotors are flutter free up to 360 knots (V-22), but at the price of a 23% thick wing and a complex flexure-coned stiff in-plane gimballed hub. The thick wing produces high compressibility drag that cuts into the very promise of high speed. A thinner wing triggers whirl flutter. Practical cruise speeds are limited to $250 - 275$ knots (V-22). The stiff in-plane rotors, with high positive pitch-flap coupling (negative δ_3 of $-15°$) realized through offset pitch links, are heavily loaded (severe chord-wise loads, particularly in maneuvers), fatigue prone, maintenance intensive, and space constrained to admit only three blades (higher vibration than four blades). The configuration is based essentially on the seminal works of Hall [1] and Gaffey [2] in the 1960s. The premise of this research is that with significant advances in materials, manufacturing, and controls over the last 30 years, a thinner wing and a lighter hub might be found. Since the growth of comprehensive analysis in the 1980s [3, 4], a wider design space has been explored. Several innovative possibilities were found, such as: tip anhedral [5, 6], composite tailoring [7, 8] and swept tips with inertial tuning [9, 10]. Many of these alternatives remain experimentally unverified. The objective of this facility is evaluate these, and other innovative alternatives, as well as acquire a rich source of validation data for high-fidelity (CFD/CSD) aeromechanics analysis of the future. But first, a state-of-

the-art blade set is needed to establish the baseline. That was the primary focus of this work.

1.3 Full- and Large-scale Tiltrotor Tests

Tiltrotors have a rich history of full-scale and model-scale flutter testing [11]. The first full-scale test was in September-October of 1957 on the XV-3 with a 2-bladed stiff-inplane rotor at the Ames 40- by 80-ft tunnel. It was followed by a decade of groundbreaking developments that finally converged to today's configuration: three-bladed stiff in-plane gimballed hub with positive pitch-flap coupling and a stiff, thick wing. It led to the first successful flutter-free (at the target speed) test of a Bell 25-ft diameter gimballed 3-bladed proprotor (Model 300, same rotor as XV-15) on a semi-span rig at the Ames 40- by 80-ft tunnel in 1969. In 1972, Boeing successfully conducted a 26-ft diameter hingeless 3-bladed proprotor test in the same tunnel and on the same wing-nacelle rig [12]. This was followed by successful 1/4.6 Froude-scale model tests of the Boeing Vertol research aircraft 222 in the Boeing tunnel up to 300 knots with a similar 3-bladed hingeless hub tilt-rotor [13]. The development of XV-15, and subsequently the JVX, followed by the V-22, saw the continuation of only the gimballed hub [14]. Several dramatic configurations have also been tested for tiltrotors: in 1972, a stop/fold version of the Bell 25-ft diameter rotor was tested successfully in the Ames 40- by 80-ft tunnel, and in 1994, a 1/6 scale NASA/Sikorsky variable diameter tiltrotor was tested in the UTRC large subsonic tunnel [17]. All of these recent tests have focused on one configuration — a scaled

XV-15 or V-22 like gimballed hub. NASA/Bell's new full-scale tiltrotor rig at the Ames 40- by 80-ft tunnel has also the same type of hub [19]. Only DLR/ONERA's 1/5 scale test model ERICA has a hingeless hub, but the model is really a propeller. These tests are meant for performance and loads, not flutter, and the gimballed hub was avoided due to complications of fabrication [20]. Thus, there is a lack of parametric flutter data that is not specific to a particular aircraft but compares a variety of wings, blades, and hubs systematically.

1.4 Model-scale Tiltrotor Tests

A brief history of major model tests since the 1970s Bell 25-ft test is summarized here.

The semi-span Bell 25-ft diameter unpowered full-scale gimballed rotor (Model 300) was tested in the Ames 40- by 80-ft wind tunnel between July to November 1970. The rotor was XV-15, the wing was a thinner 13.5% thickness to chord wing (compared to a likely $20-23\%$ thickness to chord of the XV-15 aircraft). In 1972, a Boeing 26-ft diameter unpowered full-scale hingeless rotor (Model 222) was also tested on the same semi-span rig. The concept of an interchangeable hub traces back to these models.

Boeing Vertol Company, Philadelphia, PA, designed and fabricated Froude-scale unpowered models of the above rotors as part of NASA Contract NAS 2-8235 (report in June 1975, not in public domain). The Bell model was designated M301. The design and fabrication of the model hardware was sub-contracted to William

F. Putnam Company, Princeton, NJ, who also prepared operation and maintenance procedures. The models were mounted on the exact same semi-span wing (like the full-scale models) and were of the exact same size (unlike the full-scale models) of 2.8125-ft diameter. Thus they were 1/9.244 scale and 1/8.889 scale models of the hingeless and gimballed rotors respectively. The models were later sent to MIT for gust loads measurements in the Wright Brothers wind tunnel [22, 23]. These were important models that are now destroyed. One of the objectives of this effort is to re-develop similar hub interchangeable models, but now powered, with a tilting pylon, and equipped with modern instrumentation for vibratory loads and flutter.

The Boeing rotor rotated clockwise and the Bell rotor rotated counter clockwise (when seen from the direction of nominal thrust). In the present model, both rotors will rotate in the same direction — counter clockwise — as in the right hand rotor of the XV-15 or V-22.

Two 1/5 scale semi-span V-22 models (three-bladed 7.6-ft diameter gimballed rotor) with powered rotors and conversion mechanisms were tested at NASA Langley TDT tunnel during mid 1980s to support the development of the V-22 aircraft [21]. These models were wall-mounted. The rotor was powered by a 19 horsepower motor mounted on the fuselage. Pylon conversion was accomplished by a remotely controlled lead screw actuator with a spring beam element mounted on the lower end to simulate full-scale actuator stiffness (unpublished). These models were tested during February-April 1984 and June-July 1984. A third model was tested in February-June 1985. The models were progressively improved over the tests. One of the models later incorporated a hydraulically-actuated swashplate control system for

use in active controls research. This modification changed the model's properties and flutter behavior considerably. The refined model later became the Wing and Rotor Aeroelastic Test System (WRATS) [15].

A 1/6 scale semi-span Variable Diameter Tilt Rotor (VDTR) model (three-bladed 8.2-ft diameter in hover and 5.4-ft diameter in cruise gimballed rotor) with a powered rotor and conversion mechanism was tested in the former UTRC Large Subsonic Wind Tunnel 18-ft octagonal section during the early 1990s [17]. The model was wall-mounted. The rotor was powered by a 30 horsepower hydraulic motor mounted in the stand pipe which drove the rotor through a drive shaft. The drive shaft passed through the wing to the tilting nacelle at the wing tip. But the wing was rigid, so it was not a flutter model (at least as published); the investigation concentrated on the dynamics and performance of rotor alone and the variable diameter mechanism.

Two 1/4 scale V-22 models — one isolated-rotor (sting mounted) and another full-span rotor-airframe — were designed and fabricated with a powered rotor and conversion mechanism during the late 1990s at NASA Ames [24]. These were the Tiltrotor Aeroacoustic Models (TRAM). The rotor-only model was tested in the German/Dutch Duits-Nederlandse Windtunnel (DNW) for performance, acoustics, airloads and structural loads. The full-span model, meant for flutter testing at the Ames 40- by 80-ft tunnel, was never tested. Hence there are no flutter data from TRAM. Each rotor was powered by a 300 horsepower permanent magnet electric motor, located not at the pylon, but at the base (tunnel or fuselage). The drive system from the motor went through a high-speed shaft to a conversion mechanism

onto a gear-box and then to the rotor.

1.5 Features of the New Rig

The new 3-bladed Maryland Tiltrotor Rig (MTR) has the following special features.

1. It has a hub with interchangeable gimballed and hingeless options.

2. It has a drive capable of powered and unpowered operations.

3. The rig and hub support loads of Mach-scale rotors of up to 4.75-ft diameter.

4. It has a pylon that can be tilted from 90° to 0° at increments of 5°.

5. It has interchangeable blades to support advanced aeromechanics designs.

The gimballed hub, representing all current generation tiltrotors, is the baseline hub. The hub was fabricated by Calspan Systems. Twisted blades with straight tips, representing all current generation tiltrotors, are the baseline blades. These blades were fabricated in this thesis.

A comparison of the general features with other models clarifies the uniqueness of the MTR. The MTR is different from the unpowered, floor mounted, semi-span, hub interchangeable models of the 1970s — model scale Boeing M222 and Bell M301 because of the following features.

1. Powered rotor.

2. Pylon tilt.

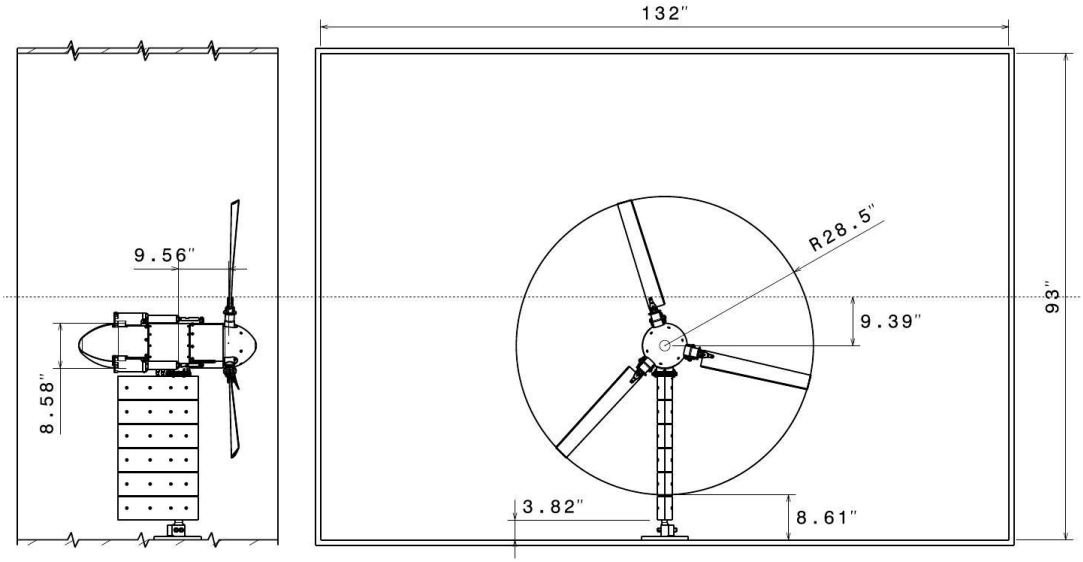

Figure 1.1: The Maryland Tiltrotor Rig (MTR) inside Glenn L. Martin wind tunnel test section (7.75- by 11-ft)

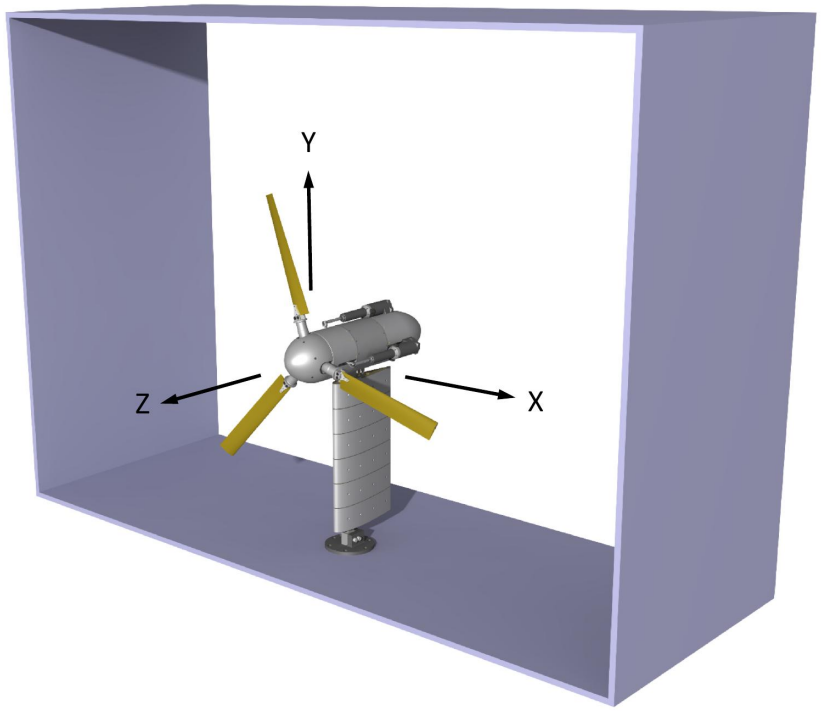

Figure 1.2: The Maryland Tiltrotor Rig (MTR) inside Glenn L. Martin test section (7.75- by 11-ft); isometric view.

3. Straight wing.

4. Modern instrumentation, including power and load cell on the pylon.

The MTR is different from the powered, wall mounted, semi-span, gimballed models — WRATS (Langley TDT), TRAM (NASA Ames) and VDTR (Sikorsky) — since then, because of the following features.

1. Interchangeable hub.

2. Motor located in pylon (simulating the engine).

3. Floor mounted.

4. Straight wing.

5. Load cell on pylon (unlike WRATS and TRAM).

6. Flutter rig (unlike TRAM and VDTR).

The extensive 1/5 scale gimballed hub Bell models tested during the 1980s were several generations of development models specific to the V-22 aircraft, and their properties and datasets are restricted and not available openly for research.

1.6 Overview of the New Rig

The rig consists of the wing frame, motor drive, rotor shaft, hubs (gimballed and, in the future, hingeless), swashplate (three-bladed), and major instrumentation hardware (see later). The blades and wing spars can be inserted in and out

depending on the nature of investigation. The blades can be Froude- or Mach-scaled; Froude- for whirl flutter and Mach- for loads. The rig is designed to allow Mach-scaled rotors, which means adequate power from the motor, and adequate structure to withstand the higher loads. The detailed design and construction of the rig is carried out by Calspan Systems. The composite blades and wing spars are designed and fabricated in-house at Maryland.

The overall specifications are given in Table 1.1.

Model Parameters	Maximum
Rotor radius R	2.375 ft
Height above ground	3.0875 ft
Rotor speed, maximum	2750 RPM
Number of blades	3
Type of hub	Gimballed and hingeless
Precone	2°
Pitch-flap δ_3	$-15°$, for gimballed only
Thrust	$300/-70$ lbf
Hub Moments	198 ft-lbf
Centrifugal retention per blade	2430 lbf
Weight of hub-pylon	65 lb
Power	Electric motor, water cooled 20 h.p. at 2660 RPM

Table 1.1: Top level MTR specifications

1.7 Size and Scale

The dimensions of the rig are shown in Figures 1.1 and 1.2 placed inside the Glenn L. Martin wind tunnel test section.

The wall clearances from the blade tip are determined by the rotor radius and

the vertical placement of the hub. Figure 1.3 shows the possible tip clearances for a given rotor radius as the hub is moved down (left of curves) or up (right of curves). The V-22 tip clearance from fuselage in cruise is around 0.105 R. With this clearance at the bottom, a radius of 2.375 ft would leave a clearance of 1.16 R at the top. The baseline position is to leave a clearance of 0.3 R at the bottom and 0.96 R at the top. This still allows a radius of clearance at the top while leaving ample space below for future needs.

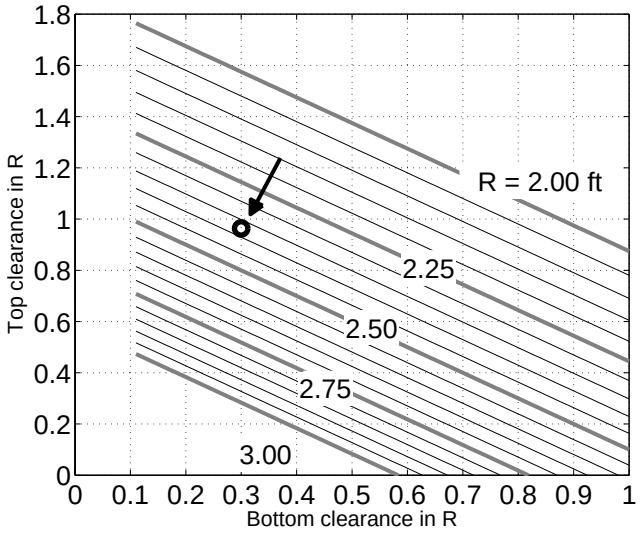

Figure 1.3: Tip clearances from top and bottom of the wind tunnel as function of rotor radius

The maximum rotor radius is presently set at $R = 2.375$ ft. So the scale factors are:

1. 1/8.00 V-22.
2. 1/2.00 TRAM (which is similar to a 1/4 scale V-22).
3. 1/5.26 full-scale Bell 25-ft diameter gimballed rotor tested at Ames 40- by 80-ft (XV-15 rotor).

4. 1/5.47 full-scale Boeing 26-ft diameter hingeless rotor tested at Ames 40- by 80- ft (Bo 105 rotor).

5. 1.69/1 of model Bell M301 gimballed and model Boeing M222 hingeless 2.8-ft diameter.

The design is anchored to Bell 25-ft gimballed (XV-15) and Boeing 26-ft hingeless (Bo 105-like) rotors where possible. The primary departure is in the pylon inertia (weight, C.G., moments of inertia). This is unavoidable because electric motors do not scale as engines, and the pylon also includes the load cell and slip ring which are components essential for model testing. The increase in inertia can be partially countered through the placement of wing frequencies but expected (and confirmed) to reduce the flutter frequencies nonetheless. Flutter at lower speeds is considered a positive feature for research purposes as long as the properties are well documented.

The MTR rotor speeds are compared to the Bell (gimballed) and Boeing (hingeless) rotors in Table 1.2.

	Scale Factor	Full-scale RPM	Froude-scale RPM	Mach-scale RPM
Bell full-scale 25-ft dia	1	458	-	-
Bell model M301 2.8-ft dia	1/8.89	-	1366	-
MTR gimballed 4.75-ft dia	1/5.26	-	1050	2409
Boeing full-scale 26-ft dia	1	386	-	-
Boeing model M222 2.8-ft dia	1/9.244	-	1174	-
MTR hingeless	1/5.47	-	903	2111

Table 1.2: MTR rotor speeds (in revolutions per minute (RPM)) compared to previous Bell (gimballed) and Boeing (hingeless) tests

For the MTR, a rotor speed of 2660 RPM will achieve the same tip Mach number ($M_T = 0.59$) as the V-22 in cruise, and a rotor speed of 3200 RPM will achieve the same tip Mach number ($M_T = 0.71$) as the V-22 in hover. The latter is deemed too high; a lower tip Mach number $M_T = 0.61$, similar to the TRAM model, is set as the maximum RPM of the MTR. This requires a lower maximum RPM of 2750.

At Froude-scale, flight speeds of 360 and 400 knots of the V-22 will translate into tunnel speeds of 130 and 140 knots respectively, which are well within the 200 knots maximum limit of the Glenn L. Martin tunnel.

1.8 Rotor

The maximum rotor radius R is 2.375 ft (0.7239 m). Airfoil profiles are assumed to begin at 0.1 R for sizing calculations but 0.263 R for the actual blades. The solidity is $\sigma = 0.1$. The blade twist is linear $-37°$: $\theta_t = \theta_{75} - 37° \, (x - 0.75)$ where $x = r/R$ and r is the radial dimension. With three blades ($N_b = 3$), and with solidity defined as projected blade area at flat pitch divided by disk area, the mean chord ($\sigma \, \pi \, R/N_b$) is 0.0759 R. Taper is zero. A single airfoil is assumed across entire span — the VR-7 with no tab.

1.9 Blades

The blades are interchangeable, and many different blade geometries will be eventually fabricated and tested on the rig. They will likely all be carbon fiber

composite blades with either rectangular or D-spars. The blades developed here are carbon fiber blades with D-spars and tungsten leading edge weights. They are twisted but uniform with no taper, sweep, or droop.

The nominal targets for blade structural properties are given in Table 1.3 based on the Bell 25-ft diameter rotor. The discontinuities near the root are due to hub connections (blade grip, pitch case, hub) and are not expected or required to be reproduced. The baseline blades developed in this thesis are for the gimballed hub and target average properties from 0.3 R to the tip. The last column gives the properties of the blades fabricated in this thesis. The mass and flap stiffness meet the targets. The chord stiffness is twice the target value, which is difficult to avoid in the model scale.

1.10 Organization of Thesis

Following the introduction, Chapter 2 describes the fabrication of the blades. Chapter 3 describes the measured blade properties. Chapter 4 describes the blade integration onto the MTR. Chapter 5 describes the rigid blade aerodynamics and flexible blade flapping analysis. Chapter 6 describes the results for the flutter system development (FSD) rig. Chapter 7 describes the results for the MTR. Finally, Chapter 8 gives the summary of the thesis and conclusions.

Property	Full scale approx	Froude scaling	Value	Mach scaling	Value	Measured value
EI_N Nm^2		s^5		s^4		
$0.1 < x < 0.3$	8×10^5		198.7		1046	
$0.3 < x < 0.5$	1.5×10^5		37.3		196.1	20.1
$0.5 < x < 1.0$	0.5×10^5		12.4		65.4	20.1
EI_C Nm^2		s^5		s^4		
$0.1 < x < 0.3$	7×10^5		173.8		915	
$0.3 < x < 0.5$	20×10^5		497		2614	937
$0.5 < x < 1.0$	12×10^5		298		1567	937
m kg/m		s^2		s^2		
$0.0 < x < 0.2$	55		1.99		1.99	
$0.2 < x < 1.0$	10		0.36		0.36	0.33

Table 1.3: Nominal stiffness and mass properties for gimballed rotor blades; EI_N and EI_C are the normal and chord-wise flexural stiffnesses and m the mass per span; 1 Nm^2 = 2.42 lbf-ft^2; full-scale values from Bell 25-ft diameter model (XV-15 rotor), x=r/R, approximate mean values are taken; s = model length/full-scale length = 1/5.26.

Chapter 2: Blade Fabrication

This chapter describes the fabrication of the model-scale tiltrotor blades. It covers materials, equipment, personal protective equipment, and then the actual procedure of blade fabrication. It also covers instrumentation with strain gauges and calibration of the gauges.

2.1 Materials

To fabricate the blades, five materials are required. These are: 1) carbon fiber, 2) foam, 3) leading edge weights, 4) root insert aluminum, and 5) adhesive. These materials are shown in Figure 2.1 in their respective parts.

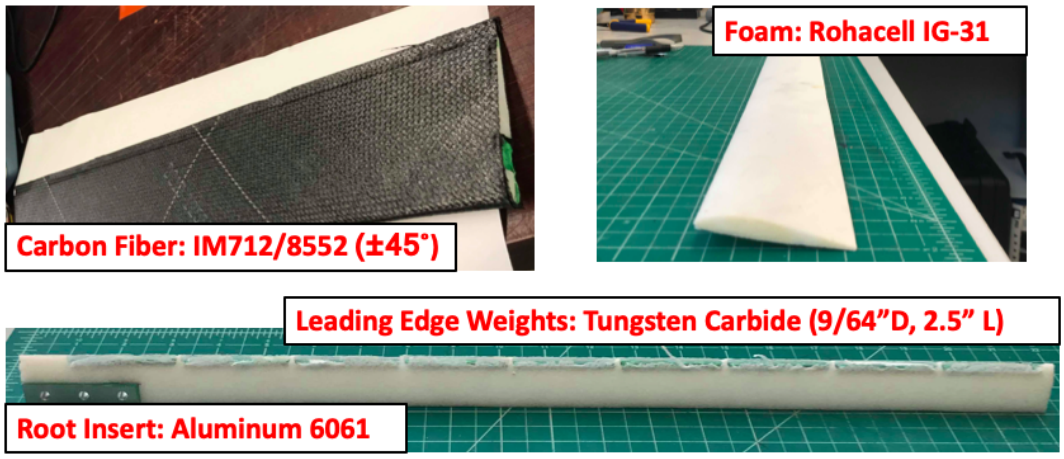

Figure 2.1: Materials used

The carbon fiber fabric used is a prepreg carbon fiber, PREPREG IM712/7552, donated by Boeing. The fabric is cut at $\pm 45°$ for use in the blades. The foam used is Rohacell IG-31. At a minimum, a piece of about 21×3.25 inches is needed with a 0.375 inch thickness, so that when it is placed in the mold it is compressed to uniform density each time. The leading edge weights, which are seven in total, are made of tungsten carbide and have dimensions of 2.5 inches in length and a 9/64 inch diameter. The root insert is machined out of Aluminum 6061, and a starting piece of $2.5 \times 1 \times 1$ inch is needed. It is easiest to fabricate in a batch of multiples at a time, so the block dimensions are increased to accommodate as many as desired. The adhesive film is Hysol PL7000, which is a 350°F capable adhesive film from Pacific Coast Composites. The adhesive is used to ensure the adherence of carbon fiber to the foam core.

2.2 Equipment

Various tools are needed to fabricate the blades. A curing oven that reaches 375°F is needed to cure the foam and the carbon fiber. A computer numerical control (CNC) machine is needed to machine the root inserts as well as foam parts. A Tormach 1100M is the CNC machine used the tiltrotor lab. It can be seen in Figure 2.2.

Figure 2.2: Tormach CNC 1100M

The drill bits used in the CNC machine are a 3/16 inch diameter bit, a 3/8 inch diameter ball mill, a 3/8 inch diameter end mill, a 9/34 inch diameter drill bit, and a 1/16 inch diameter end mill. To secure the blade molds, bolts, washers, and nuts are required. An electric wrench is needed to open and close the molds. Other tools such as a lever may be required to open the mold if it becomes stuck. A Dremel is required to shave and sand the finished blade. A soldering iron is required to wire the strain gauges. Other basic tools, such as X-ACTO knives, rulers, right angle tools, drills, wrenches, and Allen keys, are used in the process as well.

2.3 Personal Protective Equipment

To ensure fabrication safety, various personal protective equipment (PPE) is required. Whenever working with the oven, heat-proof gloves must be worn. Preferably, welder's gloves that reach up to the elbow would be used, but at the

very least, gloves covering the hands and wrists must be used. When using the CNC machine, eye goggles must be worn and the plastic safety wall must be up. The guidelines that accompany the machine and different machining techniques must be followed. When working with the adhesive film and carbon fiber before it is cured, gloves must be worn to not contaminate the materials. A proper clean layer of plastic must be placed underneath the carbon fiber while working to also ensure lack of contamination. Once the carbon fiber blade is cured and before it is sanded, protective gloves must be worn because the edges of the blade are sharp. While sanding the blade, eye goggles, N95 face mask, and gloves must be worn because carbon fiber dust is highly irritating.

2.4 Blade Molds

Presently, there are three molds for three types of blade geometries. These are shown in Figure 2.3. The twisted blade mold is the baseline.

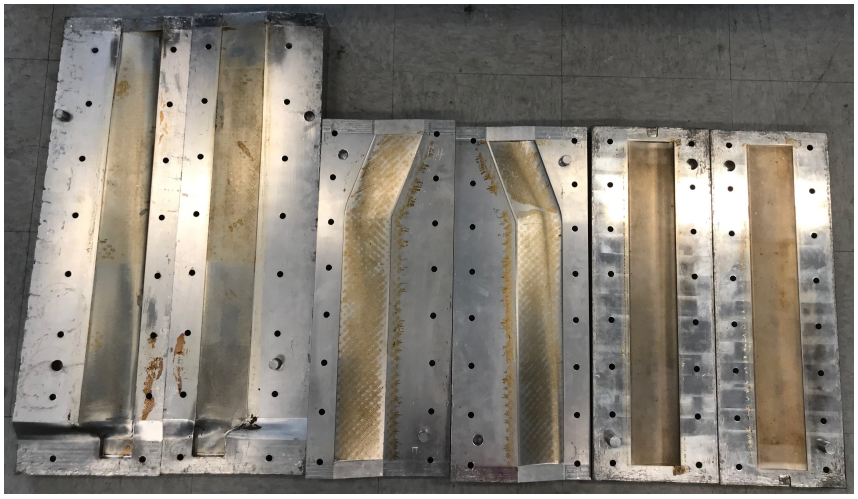

Figure 2.3: From left: twisted, twisted swept, and straight molds

The twisted blade mold is 28 inches in length, but only 21 inches are used for the blade to produce the 4.75-ft diameter rotor of the Maryland Tiltrotor Rig (MTR). The twisted swept and straight blade molds were ordered after the MTR rotor radius was decided, so they are precisely 21 inches long. The chord length for all molds is 3.15 inches. The airfoil is VR-7 with 12% thickness at 0.33 c. The twisted blade mold has a -37°/span twist rate. The molds are made of Aluminum 5083 so that it can be used repetitively without losing quality or change in shape.

The cross-sectional properties of the blades are shown in Figure 2.4.

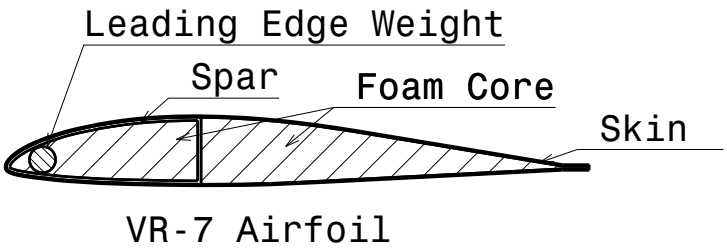

(a) Cross-sectional features

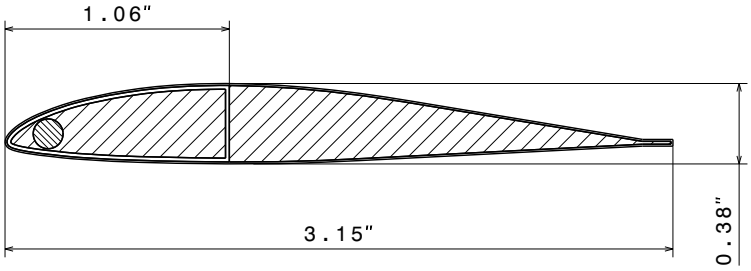

(b) Cross-sectional dimensions

Figure 2.4: Cross-sectional blade properties

2.5 Fabrication

To begin fabrication, the foam is first cut into a 21 inch $\times$ 3.25 inch piece. This piece is cut wider than the chord length (3.15 inches) because a small piece of material on each side ensures the piece stays in place in the mold. The extra material is cut off after curing to ensure the proper chord length. The foam is placed in the tip end of the mold, spanning 21 inches, leaving an empty space of 7 inches at the root end.

The mold is then clamped with bolts, nuts, and washers, using the electric wrench to ensure the top and bottom of the mold sit flush. The mold is placed on two scrap blocks of aluminum to prop up the mold so that the nuts can be tightened from underneath the mold. The bolts are tightened in a star pattern, going from the outside corners moving inwards. In addition, they should not be tightened fully at first to make sure the clamp pressure is imposed evenly. The mold is then cured in the oven for 1.5 hours at 375°F.

After cured, the mold is removed from the oven and set out to cool overnight. Once cooled, it is placed on the aluminum props so the bolts can be loosened, again using the electric wrench in the same star pattern. The top piece of the mold should be removed slowly to keep the foam from breaking or cracking. The foam is then removed, checking to make sure there was no dislocation in the curing process. The foam should be cut to the proper length if it extended while curing, and any additional overhang should be cut out as well. In addition, 1/8 inch should be cut off from the trailing edge so that the carbon fiber skin from the upper and lower

surfaces meet there and can be connected. The final foam core shape can be seen in Figure 2.5.

Figure 2.5: Blade foam core

While the foam is curing, the root insert pieces can be machined. The CAD geometry (Catia v5 used for this work) of the root insert is imported into the software SprutCam. This root insert geometry is copied and pasted into the file as many times as the number of units that can be machined out of the starting aluminum block. This makes the process more efficient since more root inserts can be created in batch. A cutting path, called a G-code, is created using this software and is uploaded with a flash drive into the CNC machine. The aluminum block is clamped in the CNC vice. A 3/8 inch steel ball mill bit is used to obtain the correct top surface curvature. A 3/8 inch end mill machines the outer dimensions. A 3/16 inch steel drill bit is used to drill the holes that will connect the root insert to the blade grip adapter.

After the foam core is cured and cut properly, it is cut into two pieces— the leading-edge and the trailing-edge. The leading-edge piece is wrapped separately for the spar. To cut the foam core into two pieces, the inner (Figure 2.6(a)) and outer (Figure 2.6(b)) dimensions of the spar are measured and marked so there is enough space for the two plies of carbon fiber that will be wrapped around the leading-edge to create the spar. The foam is clearly marked so the demarcating line

can be referenced while milling (Figure 2.6(c)).

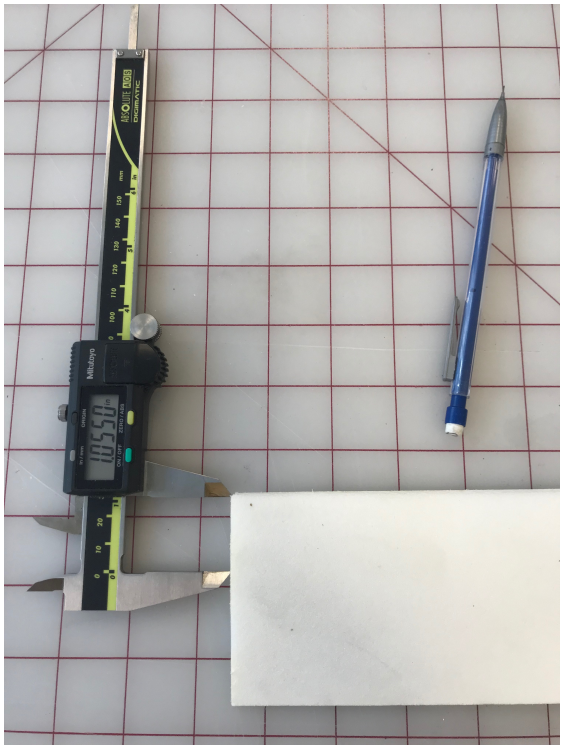

(a) Inner spar measurement

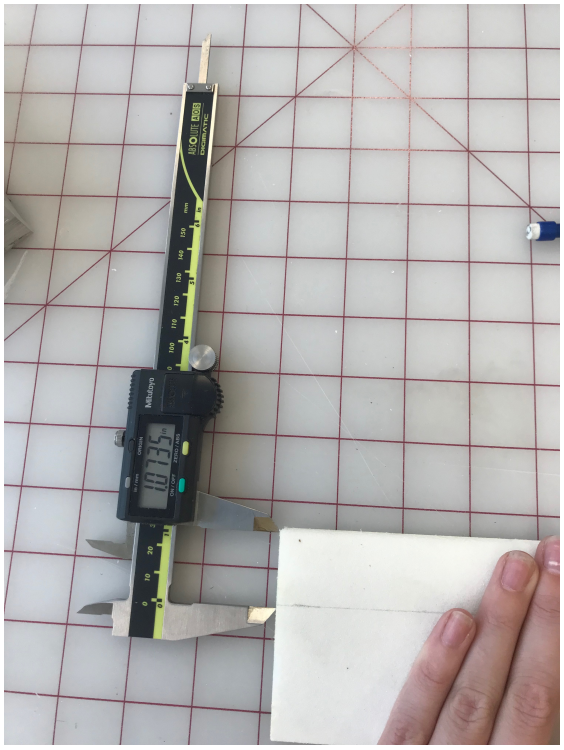

(b) Outer spar measurement

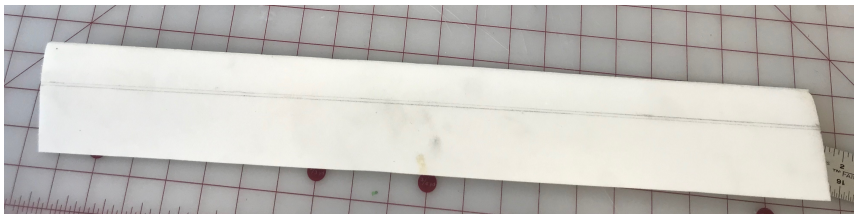

(c) Line created

Figure 2.6: Spar cut measurement

The marked foam core is mounted onto a 3D printed mold that allows the core to be clamped using the vice for milling (Figure 2.7). Even though the blade is twisted, the clamped section is be held untwisted by the mold, so cutting along the radial axis will create a straight line and cut perfectly vertical. In addition, due to the mold being shorter than the blade, the mill must be stopped once it exceeds the mold length. The mold must then be shifted along the core so the foam is never

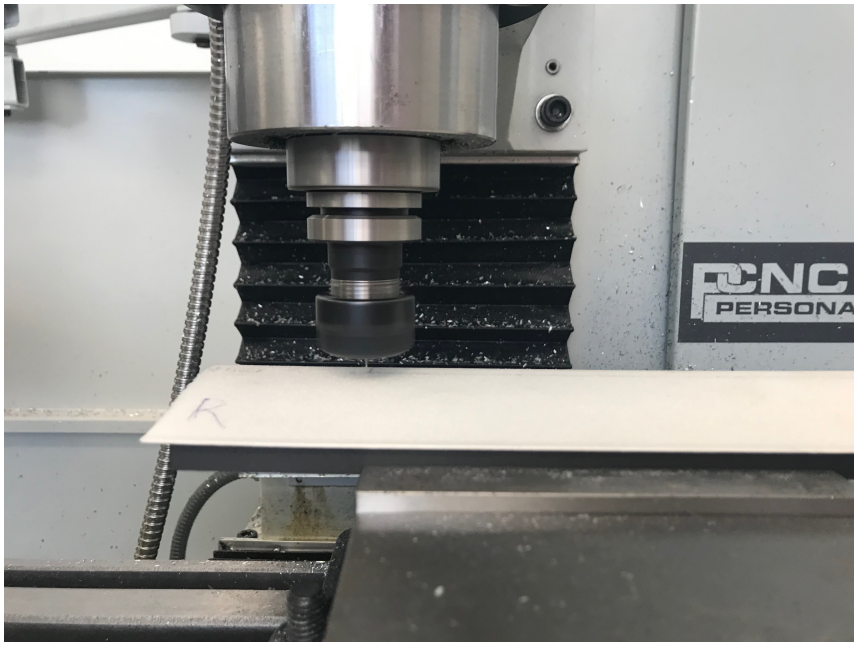

Figure 2.7: Spar cut on mill using 1/16 inch aluminum mill bit

being cut without the support of the mold. When the mold is moved, the mill must be re-zeroed in the chord and thickness directions to ensure the cut is at the correct chord location and depth. A 1/16 inch aluminum mill bit is used to cut the core.

Next, the slots for the root insert and leading edge weight are cut out and milled respectively. The root insert is placed on top of the leading-edge foam where it will be sitting and is traced. This tracing is cut with an X-ACTO knife and then sanded to get a perfect fit. It is important to cut the root insert tracing at the correct angle because it is twisted, so it cannot be cut straight down. The leading-edge foam is then placed in another 3D printed mold that holds the leading-edge piece with only the leading edge exposed. The mold is clamped into the vice with the leading edge facing up (Z direction of the CNC machine), so the leading edge weight slots can be milled out (Figure 2.8). Seven slots are cut for the leading-edge weights evenly distributed along the span. The slots are cut to a depth that allows

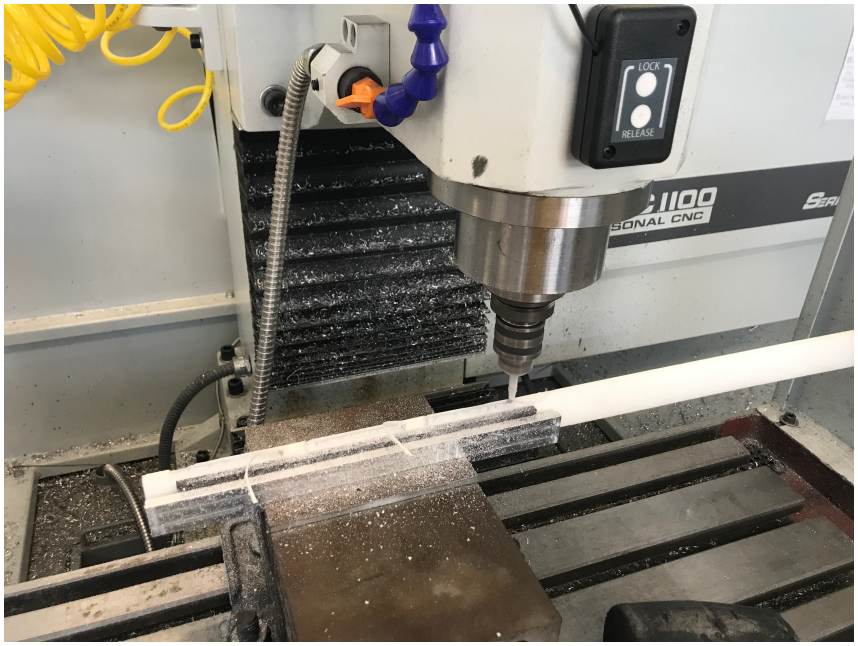

Figure 2.8: Leading-edge weight slots cut with 9/34 inch drill bit

the leading-edge weights to be placed without deforming the airfoil shape.

After the milling is completed, the leading-edge weights are wrapped in film adhesive and inserted into the leading edge slots. Gloves must be worn throughout this stage so no contaminants are introduced. The adhesive wraps around the cylinder of the leading-edge weight once (Figure 2.9). The excess adhesive is cut so extra weight is not added. Once wrapped, the weights are placed into the milled slots.

Figure 2.9: Leading-edge weight adhesive wrap

The root insert is wrapped around once in the film adhesive and placed in its slot at the root end of the leading-edge foam. The adhesive and foam will adhere

with light pressure, so the root insert is simply hand pressed into place. The adhesive is very sensitive to heat, even at room temperature, so once it is out of the freezer, it must be used quickly or else it will become too sticky to work with. If it does become too sticky to work with, place it back in the freezer and leave it for ten minutes when it can be used again.

The leading-edge piece and the trailing-edge piece are then also wrapped in around in film adhesive once. The wrapped pieces can be seen in Figure 2.10. Because the blade is twisted, the adhesive film must be cut 1 inch longer than the foam so that it can follow the blade twist and not wrinkle. The foam is centered on the piece of adhesive before it is applied. As the film is applied to the foam, it must be rolled on with a roller to eliminate any wrinkles and to guarantee adhesion between film and foam. The overhang is trimmed off after the pieces are successfully wrapped.

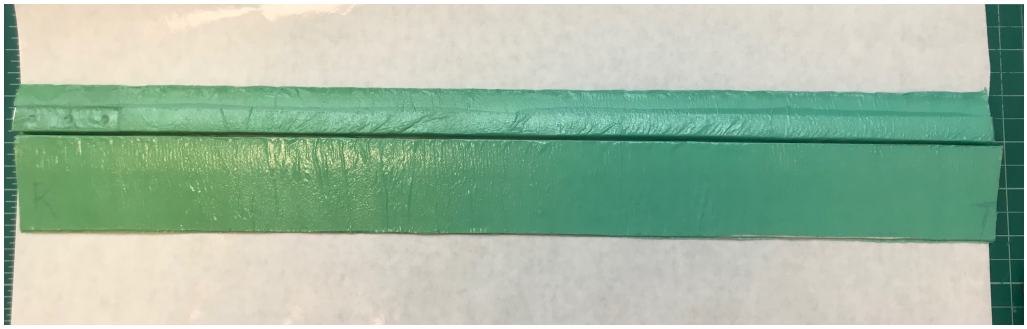

Figure 2.10: Leading-edge piece and trailing-edge piece adhesive wrap

Once the two foam pieces are wrapped in adhesive, the carbon fiber is cut. Two pieces are cut— one for the spar and one for the skin. It is easiest to cut both pieces at once because the roll of carbon fiber is already spread out and does not need to unwrapped twice. The carbon fiber for both pieces is cut at $\pm 45°$, so a right

triangle tool is placed on the edge of the fabric and the carbon fiber is cut on that angle. There is a stencil for the dimensions of both pieces, and it is placed against the right triangle to cut the width of the piece with an X-ACTO knife. The stencil is only 9 inches long, so the cut is extended with a ruler to reach the 22 inches required for the blade. The fabric is cut longer than the finished blade dimensions (21 inches) because the twist of the blade will cause the fabric to twist so there must be excess on each side.

The spar is created by wrapping the leading-edge piece twice in carbon fiber. The side of the leading-edge piece cut for the spar is aligned along one end the carbon fiber and pressed to adhere (Figure 2.11). As the fiber fabric is wrapped around the piece, it is rolled on and pulled tight but without stretching it and changing the material properties. It must be rolled down firmly to the foam core so the fiber and adhesive can bond properly and so there are no visible wrinkles or imperfections. The carbon fiber is then wrapped twice around the leading-edge piece. Using the stencil during the cutting process ensures that there will be exactly two plies around the spar; if there is less than two, the fabric was not pulled tight enough and if there is more than two, the fabric was pulled too tight and the strength is compromised.

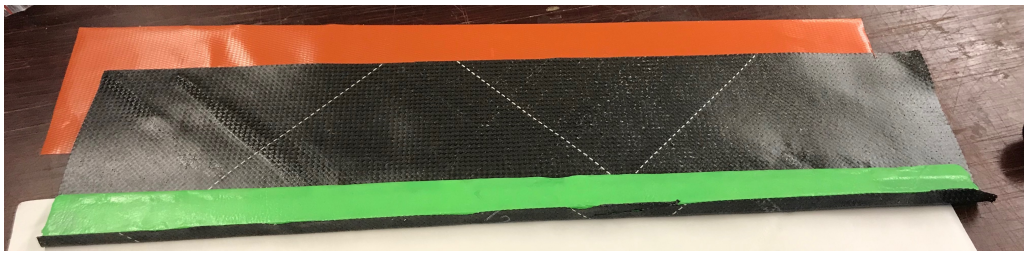

Figure 2.11: Carbon fiber spar wrap in progress

The completed spar is then lined up with the trailing-edge piece such that the

correct sides face each other chordwise and spanwise. The connection of the spar to the trailing-edge piece must be centered in the thickness direction because the spar is now thicker than the trailing edge before it is wrapped, so the center of each piece must be attached. The skin is started 1/8 inch behind the trailing edge so the plies from the top and bottom can attach on both sides of the blade (Figure 2.12(a)). The skin is rolled on over one side of the blade. Since the blade twists, the fabric must follow the curve and remain flat. It must be pulled tight around the leading-edge because a smooth leading-edge is crucial to aerodynamics. If there is too much fabric on the leading-edge, it will compress in the mold and produce local wrinkles. The ply is then rolled onto the other side of the blade and connected at the trailing edge to 1/8 inch tab of fabric started there. The excess carbon fiber at the root and tip of the blade can be cut with an X-ACTO knife (Figure 2.12(b)).

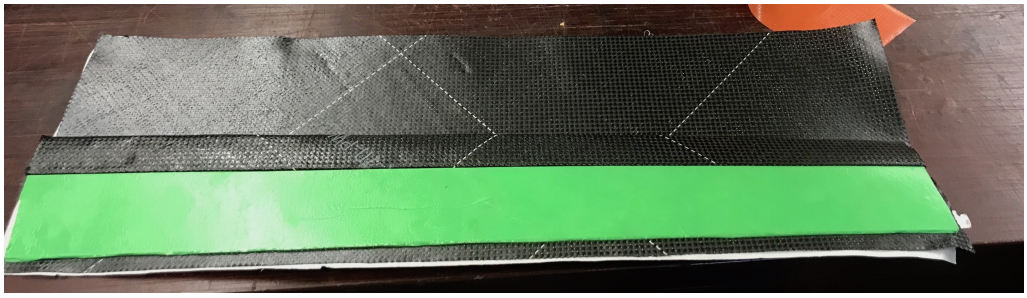

(a) Carbon fiber skin wrap in progress

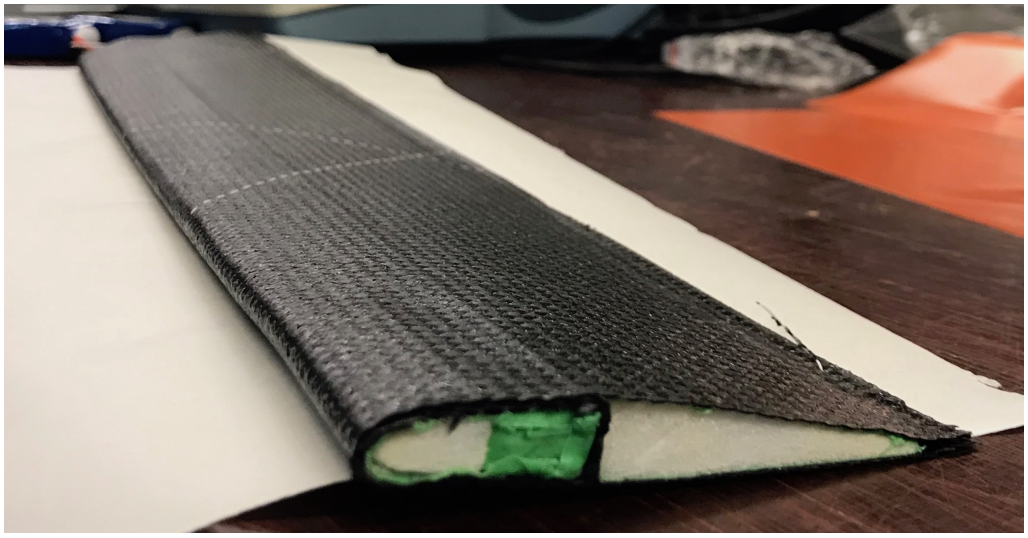

(b) Completed wrap

Figure 2.12: Carbon fiber skin wrap, straight blade shown for clarity

After the skin is wrapped, the blade layup is complete, and it is ready for curing. The blade is wrapped in release ply, which is nominally cut to the same size as the blade but with a small extra margin. The release ply is used so the resin from the carbon fiber does not stick to the mold while curing. The wrapped blade is then placed in the twisted blade mold. The mold is closed and tightened with the electric wrench until the top and bottom sit flush. The mold is then put into the oven and set to cure for 2.5 hours at 375°F. Once cured, the blade is removed from the oven and set out overnight to cool. Once cooled, it is carefully removed from the mold (Figure 2.13).

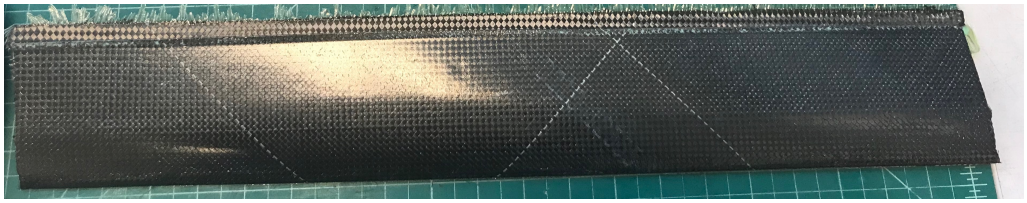

Figure 2.13: Post-cure pre-finished blade

After putting on proper gloves, goggles, and mask, the excess carbon fiber on the trailing edge is shaved off. A Dremel is used to cut the majority of the excess, and then the trailing edge is sanded until it is perfectly straight and the chord length is correct. If the length of the blade exceeds 21 inches, the root and the tip can also be hand-sanded.

To drill out the root insert holes through the skin, a wooden piece is placed under the blade so the table is not drilled onto. An extra root insert is lined up on top of the blade to follow the one through the inside, and using the smallest drill bit, the holes are drilled through. The drill bit size is increased until reaching the final 3/16 inch diameter. After all trimming and drilling is complete, the carbon fiber dust must be vacuumed with the shop vacuum and then wiped with a rag so there is no further residue. The finished blade attached to a blade grip can be seen in Figure 2.14.

Figure 2.14: Finished blade With blade grip

2.6 Sensor Installation

After the blade is completed, it must be instrumented with strain gauges. Flap bending moments are always the principal blade loads in any rotor test, so all three blades were installed with flap bending gauges. Two blades, marked Blade 1 and Blade 3, were also instrumented with torsion gauges. One blade, marked Blade 2, was left to carry only a flap gauge for the academic purpose of minimizing the impact of sensor insertion on blade properties. The flap gauges are a dual bending gauge on both the top and bottom of the blade. The torsion gauges are a dual shear gauge on both the top and the bottom of the blade. The flap bending gauges are installed at 0.25 c and 0.4 R, and the torsion gauges are installed at 0.33 c and 0.4 R. Both types of gauges are placed facing the tip in a 0/90 orientation (Figure 2.15).

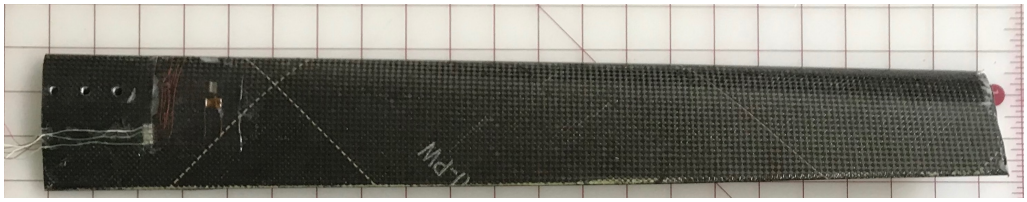

Figure 2.15: Strain gauge chordwise and radial locations

To install the strain gauges, first, the location is de-greased. Then, conditioner is applied to the location, and it is sanded with 300 gauge sandpaper. The sanding is required for the glue to properly bond with the blade. The conditioner used can be seen in Figure 2.16(a). To sand the location, a small strip of the sandpaper is wrapped around tweezers for ease of use (Figure 2.16(b)). After sanding, the area is wiped with clean gauze from the center outwards so it it not contaminated by debris. This step is then repeated with 400 gauge sandpaper.

(a) Conditioner used

(b) Area sanded with conditioner

Figure 2.16: Conditioning process to prepare for strain gauge installation

Once the surface is conditioned, the exact location of the gauge is marked in pencil, with a line on the radial dimension and a line on the chordwise dimension (Figure 2.17(a)). Neutralizer is then applied to the area, which ensures pH neutrality so the strain gauge does not corrode (Figure 2.17(b)). A cotton swab is then used to remove the neutralizer and any remaining contaminants.

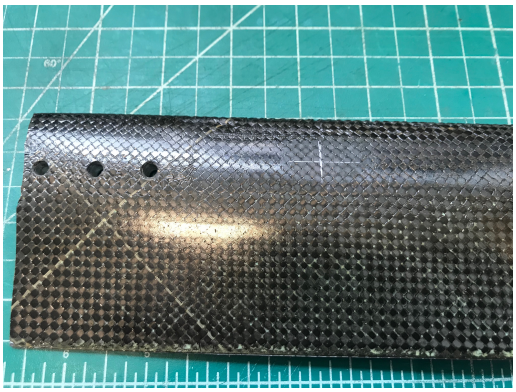

(a) Cross-section marked

(b) Neutralized area

Figure 2.17: Marking and neutralization of area to prepare for strain gauge installation

The next step is to place the selected strain gauge on a neutralized slab of glass face up. A piece of tape is placed on the glass and strain gauge and pressed down. One end of the tape is slowly peeled up such that the gauge comes off attached to the tape. This tape is then positioned and pressed on the marked location, with the center of the gauge over the chord position and the side dots on the gauge over the radial position. The front of the gauge, where the sensor is located, is placed towards the tip of the blade. The tape is then lifted again with the gauge attached such that a bonding agent can be applied to the bottom of the gauge (Figure 2.18).

Figure 2.18: Bonding agent on strain gauge

The bonding agent air-dries within a minute, after which a small dot of superglue is applied at the base of the gauge. The tape is then pressed back down, smoothing the tape and pushing out excess glue from the gauge. The glue is activated by pressure, so the gauge is pressed by a finger for approximately a minute, and then left to dry for 20 minutes (Figure 2.19). This process is repeated for all gauges.

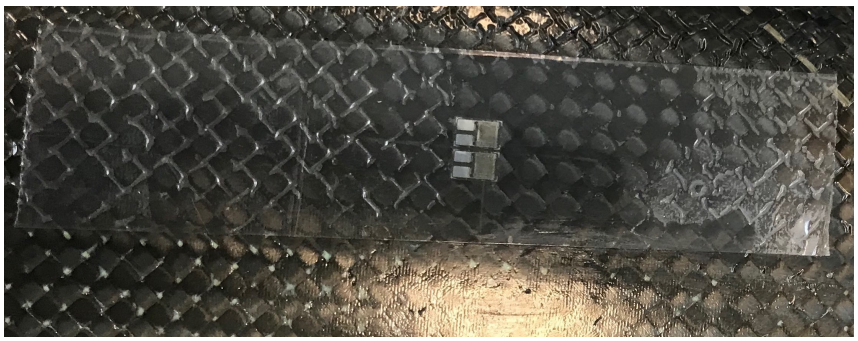

Figure 2.19: Bending Strain Gauge After Pressure Applied

Once the gauges are installed, they must be wired. Bondable terminals are applied with superglue to a location near the base of the blade but out of the way of the blade grip adapter (Figure 2.20).

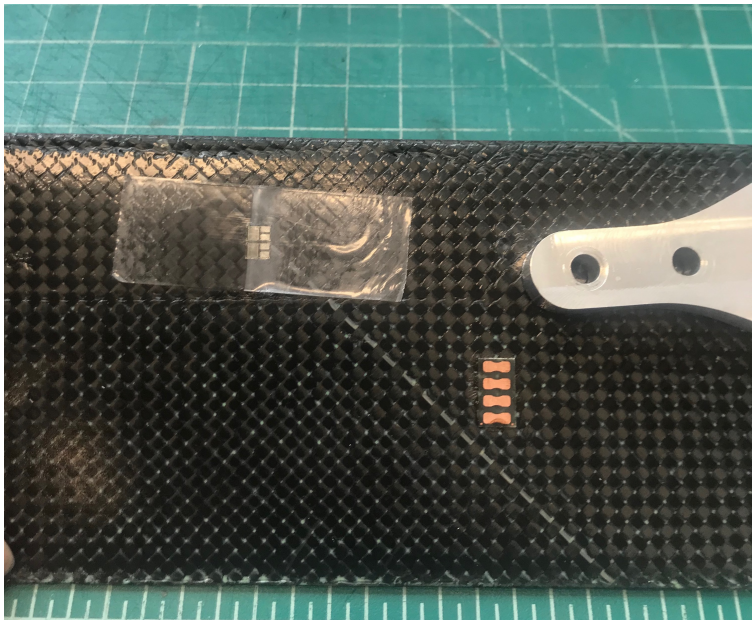

Figure 2.20: Blade root section displaying blade grip, strain gauge (under tape) and bondable terminals

For the wiring that follows, a soldering iron, solder, and flux is required. A full Wheatstone bridge is wired for both the flap bending gauge and torsion gauge, with the wires from the top and bottom gauges connecting to the appropriate bonded terminal. A full Wheatstone bridge circuit can be seen in Figure 2.21(a). Strain gauges act as the resistors, and their assigned numbers and locations on the blade for both bridges can be seen in Figure 2.21(b). The numbers 2 and 4 represent the top dual gauge, and the numbers 1 and 3 represent the bottom dual gauge.

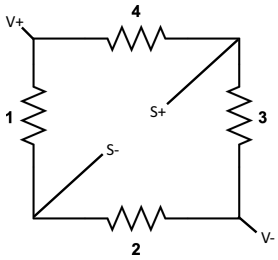

(a) Full Wheatstone bridge circuit

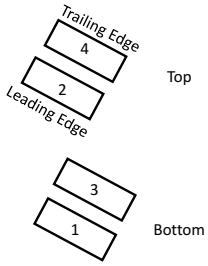

(b) Strain gauge numbers correlating to Wheatstone bridge circuit

Figure 2.21: Full Wheatstone bridge circuits

The ±V (power) and ±S (signal) points on the circuit diagram represent ports on the bondable terminals. There are a total of 4 terminals for each bridge. The physical circuits can be seen in Figure 2.22. This blade has both torsion and bending gauges, so there are two full Wheatstone bridges on the blade.

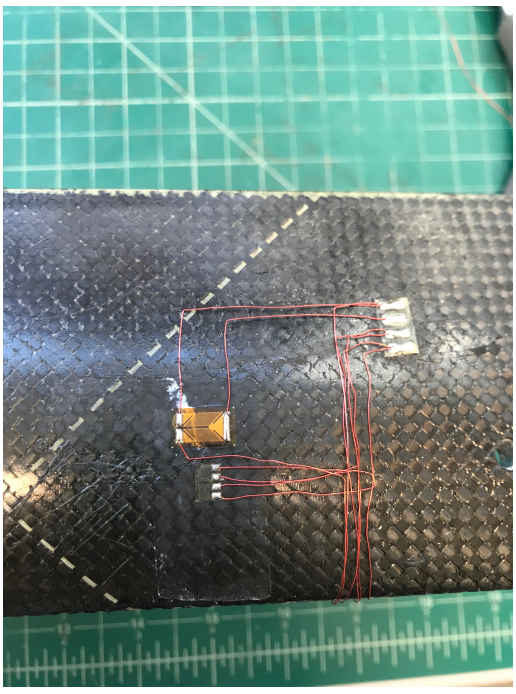

(a) Wheatstone bridges on the top of the blade

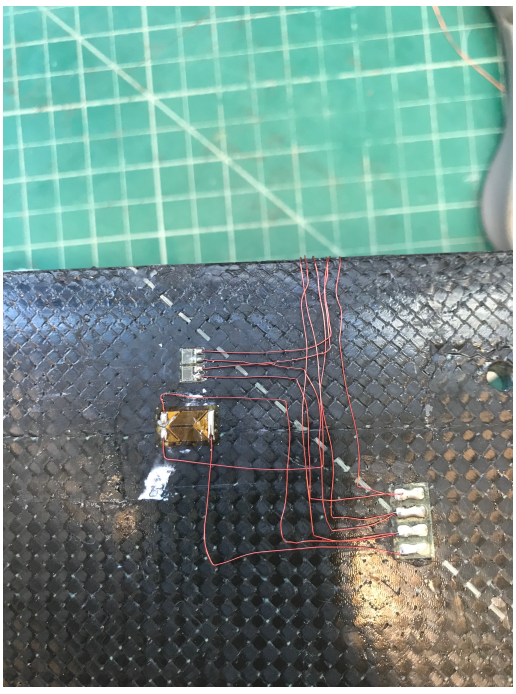

(b) Wheatstone bridges on the bottom of Blade)

Figure 2.22: Wheatstone bridge wiring

A full Wheatstone bridge is desired for maximum accuracy. The ±V and ± S terminals are wired with color coded 32 gauge wire. Red is +V, black is -V, green is +S, and white is -S. These wires are connected from the corresponding bondable terminal to the data acquisition unit (DAQ) (Figure 2.23). The DAQ is a National Instruments unit, and the corresponding software is LabView.

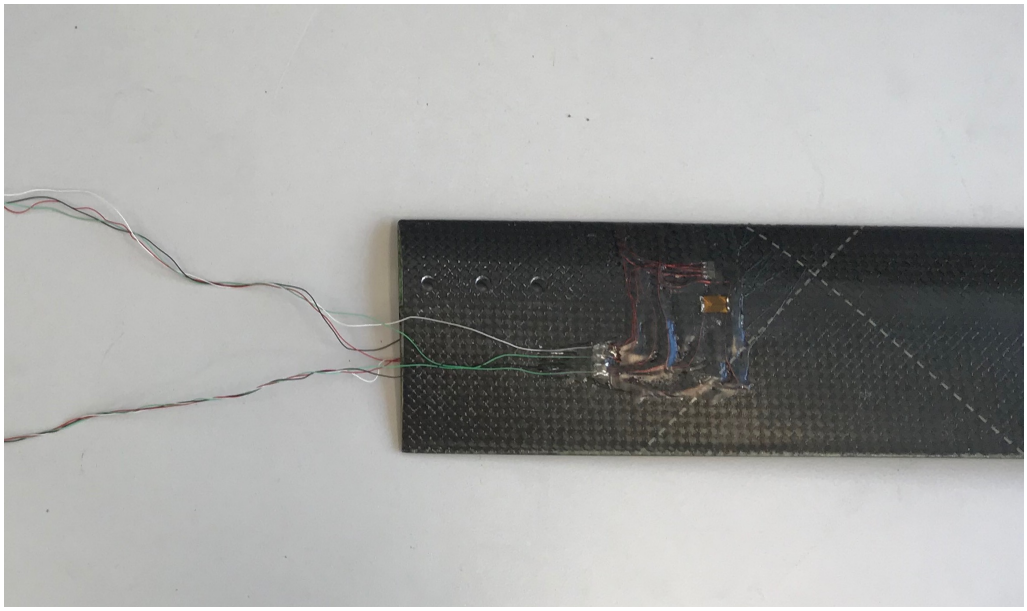

Figure 2.23: ±V power and ±S signal wiring

All wires are epoxied to the blade so they are firmly attached to the surface. The epoxy is spread with a wood tongue depressor and smoothed with tape so that it is a thin layer and is smooth around the leading edge (Figure 2.24). The epoxy needs 24 hours to cure, and only then can the tape be carefully removed. The finished instrumented blade can be seen in Figure 2.25.

Figure 2.24: Epoxy curing under tape

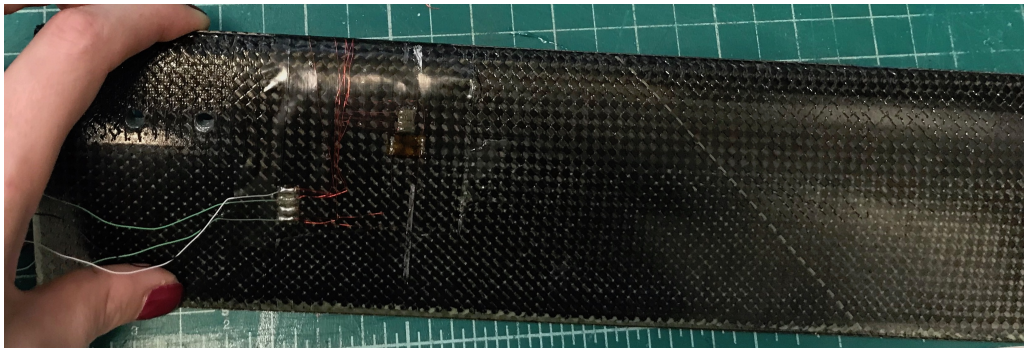

Figure 2.25: Fully instrumented blade

2.7 Sensor Calibration

To calibrate the strains to the bending or torsion moments, a rig was set up, made of 80/20 aluminum pieces with a vice at the bottom to securely clamp the blade (Figure 2.26). The sectional moments are generated by applying a tip force. The tip foce is applied using a VR-7 airfoil piece that is 3D printed and placed around the section at the tip with a string attached that can be pulled. For flap bending calibration, the string is attached at 0.25 c and loaded by a pulley with

hanging weights.

Figure 2.26: Flap bending calibration setup

Each blade is loaded and unloaded for a minimum of three trials, and the average is taken. A linear regression is performed to get the linear relationship and the R^2 value to determine how close the data fits to the line. Each blade will have

its own y-intercept due to strain gauges not being identical, but the slopes of the lines are close between blades. The calibration plot for Blade 3 is shown in Figure 2.27.

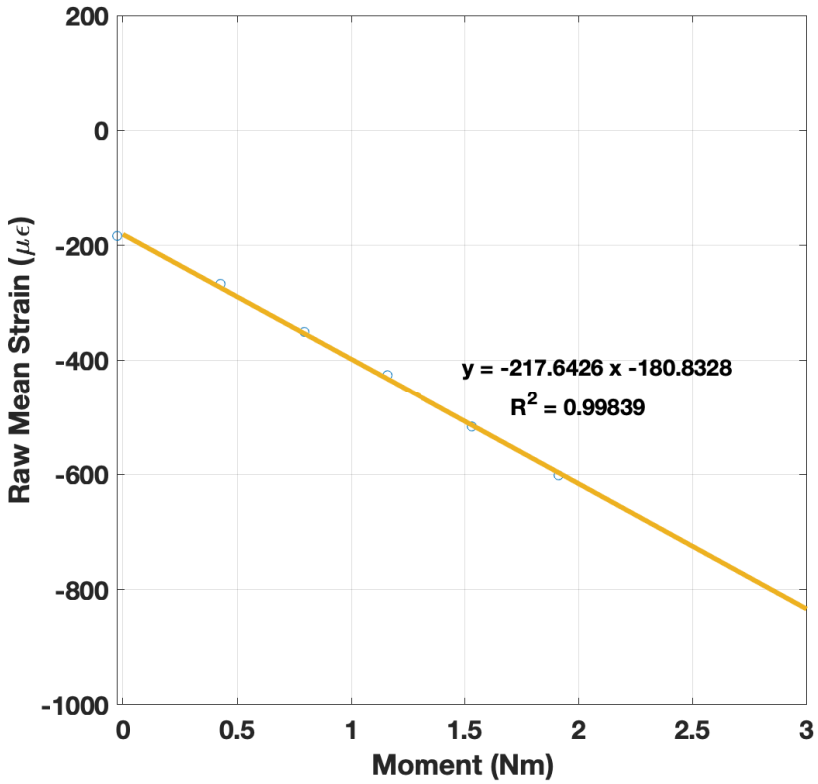

Figure 2.27: Flap bending calibration measurements for Blade 3

For torsion, a top piece shaped like a bar is attached to the blade tip (Figure 2.28(a)). A string is attached to each end of the top piece and is loaded with pulleys. With both strings applying the same load, a pure torsion moment is produced (Figure 2.28(b)).

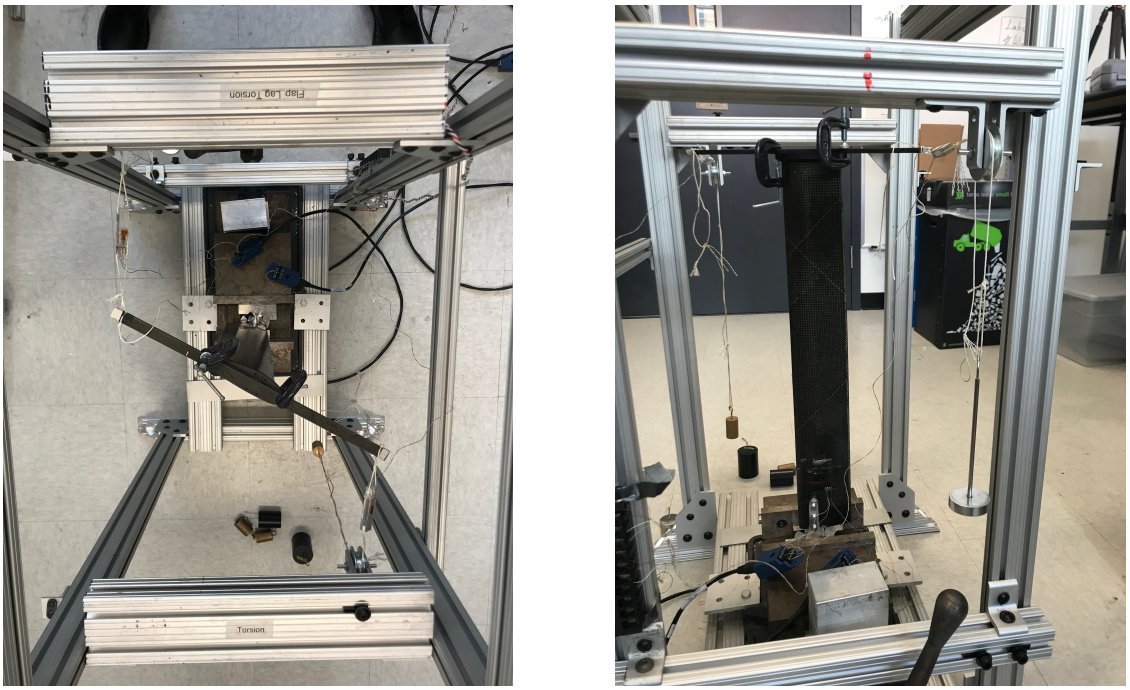

(a) Torsion moment calibration (top view)

(b) Torsion moment calibration (side view)

Figure 2.28: Torsion moment calibration

As in the bending calibration, each blade is loaded and unloaded for a minimum of three trials, and the average is taken. A linear regression is performed to get the linear relationship for all loads and the R^2 value to determine how close the data fits to the line. As can be seen in Figure 2.29, a pure torsion moment could not be achieved, and there was some coupling with flap bending moment. The correlation is not as high as in flap bending, but it is still good.

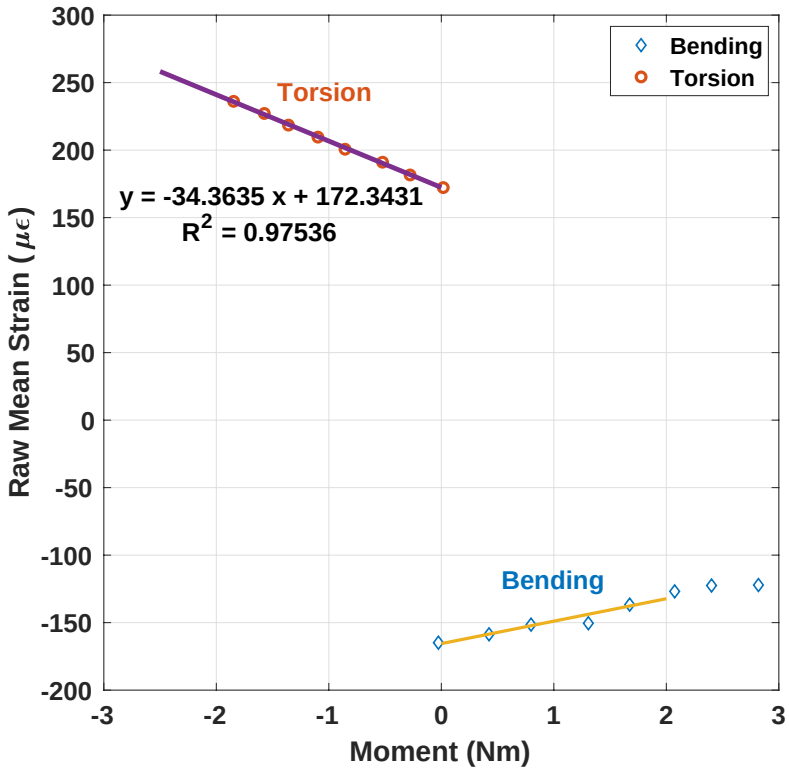

Figure 2.29: Torsion calibration measurements for Blade 3

Using the DAQ strain gauge module and LabView, the strain is measured and plotted versus moment to get the calibration relationship between the two. This relationship is linear and shown in Figure 2.29. During wind tunnel testing, this calibration is used to convert the strain measurements into moments. The moments are used to monitor the load limits.

Chapter 3: Blade Properties

This chapter describes the blade properties. It covers the blade geometries, weights, non-rotating frequencies, and stiffnesses.

3.1 Weights

Recall, the twisted blades are 21 inches long, with a 3.15 inch chord length, and 12% c thickness. The cross-section is a VR-7 Airfoil. The weights of all the blades fabricated are listed in Table 3.1.

Blade	Weight (g)	Frequency (Hz)
1	178.58	17.56
2	175.20	15.49
3	181.68	17.07
4	172.49	
5	175.11	
Mean	176.61 $\pm$ 2.87%	

Table 3.1: Blade weights and frequencies

3.2 Non-Rotating Frequencies

The non-rotating frequencies are measured for both the straight blades and twisted blades, but this section specifically discusses the measurement of the twisted blades. To measure the frequencies, the blade is clamped at the root, and the

distance from the tip to the edge of the clamp is recorded. The flap strain gauges are connected to the DAQ. The tip of the blade is pulled back and released, and the strains from the gauges are recorded versus time until the blade comes to rest. The Fast Fourier Transformation (FFT) of the strain signals is used to extract the first non-rotating frequencies. At least three trials are taken for each blade for the three blades. Only the first flap frequency is picked up.

The FFT of the strain signal for the first blade is shown in Figure 3.1. Each line represents a separate trial. The mean of the Blade 1 frequency measurement is 17.56 Hz (±0.6%).

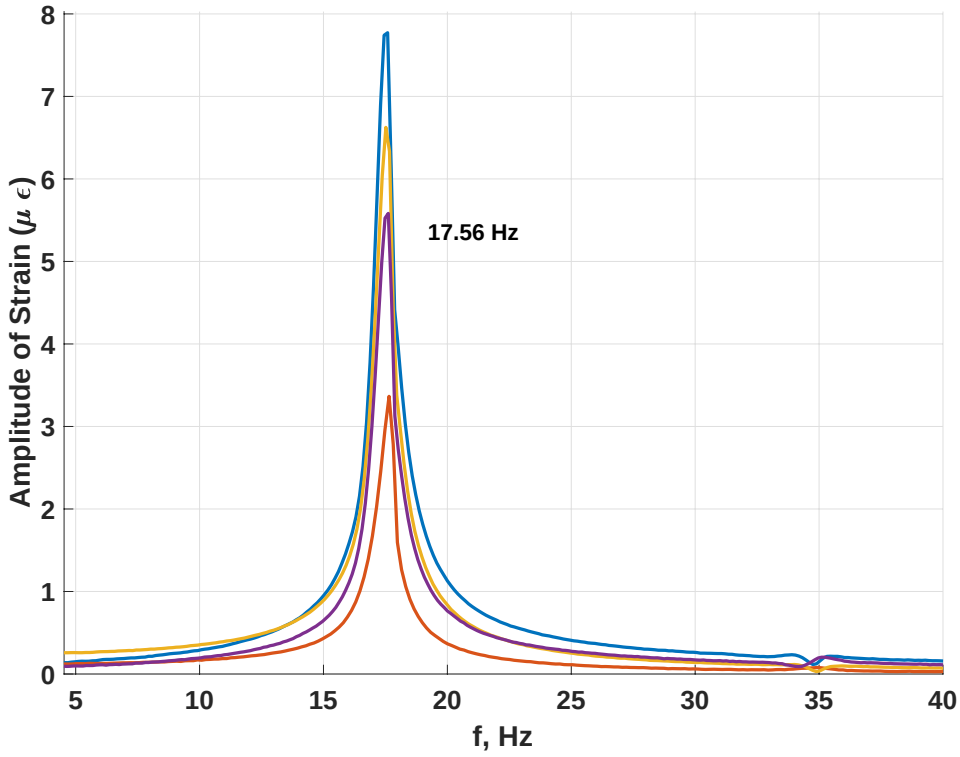

Figure 3.1: Strain magnitude versus frequency for Blade 1

Blade 2 was clamped at a longer distance from the tip, but only because the

epoxy prevented the clamp from sitting at the same location as the first and third blades. This results in a lower non-rotating frequency than the first and third blade. The mean of the frequency measurement of Blade 2 is 15.49 Hz (±1%), and the FFT of the strain signal of the second blade is shown in Figure 3.2.

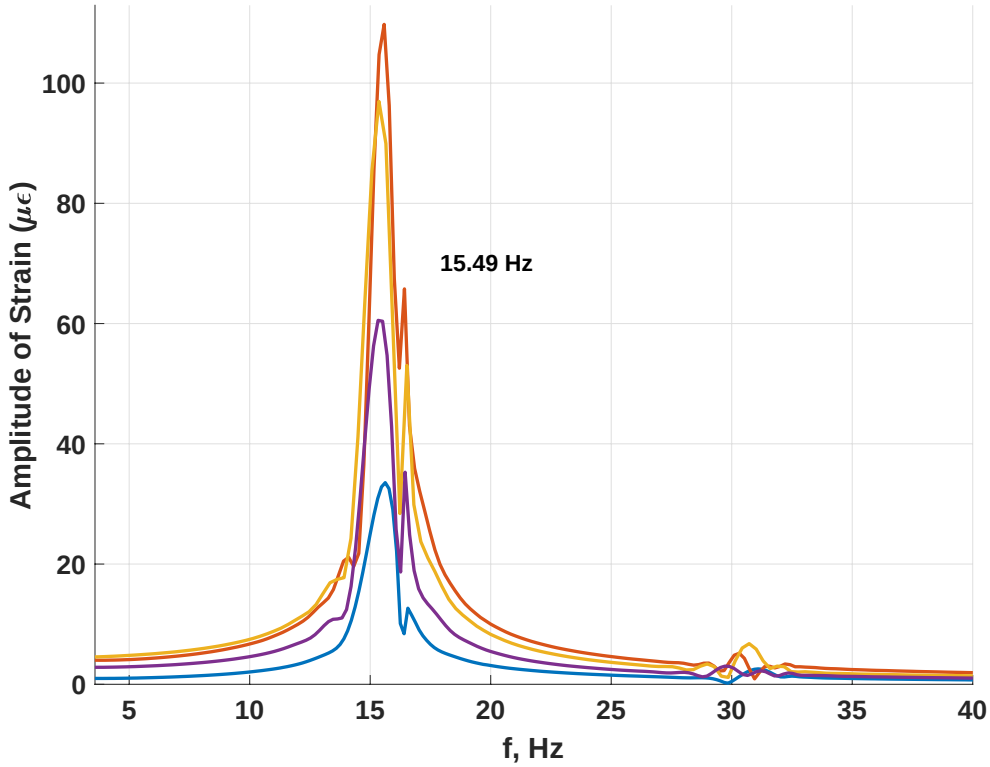

Figure 3.2: Strain magnitude versus frequency for Blade 2

The mean of the frequency measurement of Blade 3 is 17.07 Hz (±1%), and the FFT of the strain signal of the third blade is shown in Figure 3.3.

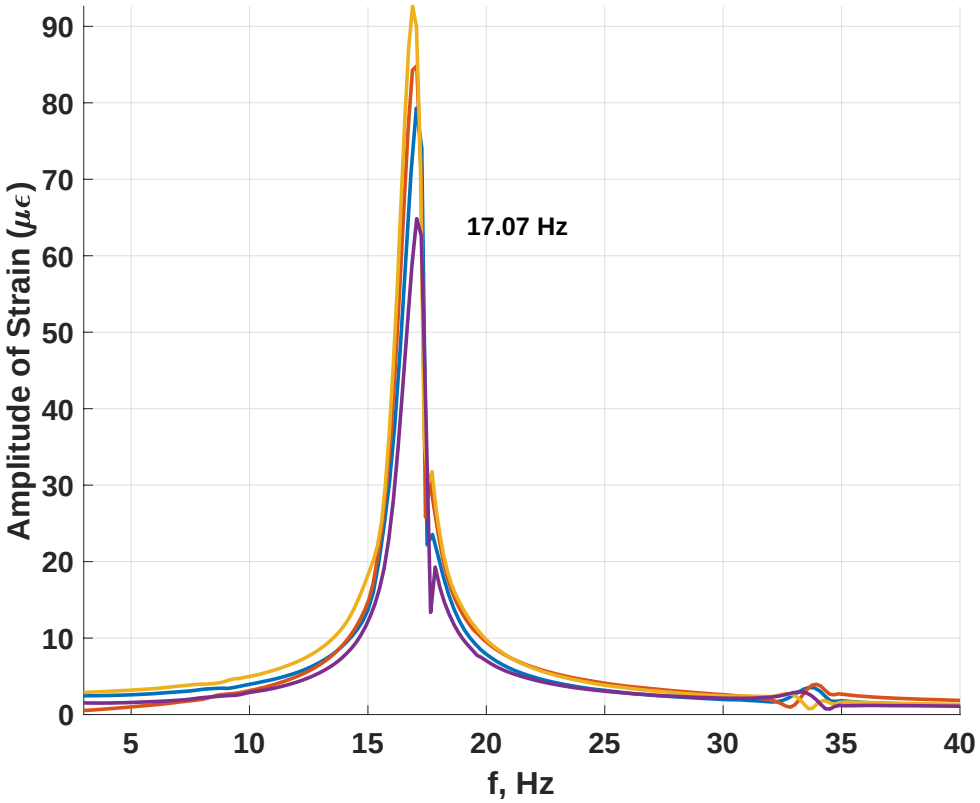

Figure 3.3: Strain magnitude versus frequency for Blade 3

3.3 Stiffness

The flap bending stiffnesses for the straight blades are measured. An accelerometer method is used. In this method, two accelerometers are placed on a blade vertically to obtain the positions based on change in g-level. From there, slopes and curvature of the blade are calculated to obtain the stiffnesses.

For a straight blade, the sectional normal direction N is the same as the flap direction Z, and the sectional chordwise direction C is the same as the lead-lag direction Y. However, in a twisted blade, the normal direction changes over the span of the blade. The Y and Z directions are now related to the normal and

chordwise directions as:

$$\begin{pmatrix} Y \\ Z \end{pmatrix} = \begin{bmatrix} \cos\theta & -\sin\theta \\ \sin\theta & \cos\theta \end{bmatrix} \begin{pmatrix} C \\ N \end{pmatrix}$$

where θ is the sectional nose-up pitch. If a section has no pitch, and Y and Z are assumed to be the principal axes, then the flap and lead-lag bending moments are:

$$M_F = -M_Y = EI_Z w''$$

$$M_L = M_Z = EI_Y v''$$

where w'' is the flap curvature (for small deflections) and v'' is the lead-lag curvature (for small deflections). The flap stiffness EI_Z and the lag stiffness EI_Y are the same at all radial locations, and equal EI_N and EI_C respectively.

If a section has a pitch angle, and N and C are now the principal axes, then

$$M_F = -M_Y = \left(EI_N \cos^2\theta + EI_C \sin^2\theta\right) w'' + \frac{1}{2}\left(EI_C - EI_N\right)\sin 2\theta v''$$
$$M_L = M_Z = -\left(EI_N \sin^2\theta + EI_C \cos^2\theta\right) v'' - \frac{1}{2}\left(EI_C - EI_N\right)\sin 2\theta w''$$

The coupled terms are difficult to measure and highly error prone. After many trials of obtaining non-repeatable stiffnesses on the twisted blades, the attempt was discarded, and it was determined that straight blades would be best suited for property measurement. Accordingly, straight blades were fabricated.

The measured EI_N for the straight blade is 20.1 Nm^2, and the EI_C is 937 Nm^2.

An effective EI_N can also be obtained from non-rotating frequency measurement of the twisted blades using the simple relation

$$w = 3.52\sqrt{\frac{EI}{mR^4}} \text{ rad/s}$$

where $w = 2\pi f$, $f = 17.5$ Hz (Blade 1), $m = 0.3$ kg/m, and $R = 0.533$ m. Solving for EI,

$$EI = \frac{mw^2R^4}{3.52^2} = 24.6\ Nm^2$$

The straight EI_N is close to the effective value obtained from non-rotating frequency measurement of the twisted blade, but softer as expected due to the absence of coupling with lead-lag motion.

Chapter 4: Integration on MTR

This chapter describes the integration of the fabricated blades to the MTR. It covers the testing preparation in lab and the in-tunnel checks that the set-up is working correctly.

4.1 Static Balance

The blades are balanced on a blade-balancer (Figure 4.1). Blade 1 is bolted into one side, and the other blades are rotated through on the opposite side. The blades are balanced if both blades did not touch the table. Electrical tape is added to the tip leading edge to rectify any imbalances. No current blades needed electrical tape added.

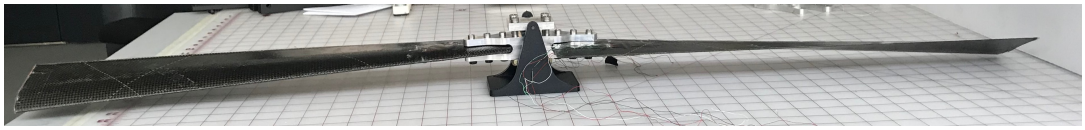

(a) Side view

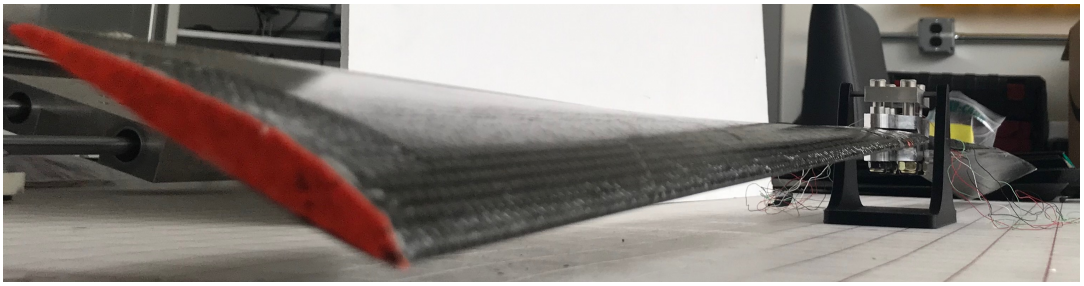

(b) Isometric view

Figure 4.1: Blade balancing

4.2 Preparation for Tracking

A reflective tape is attached with superglue to each blade tip so a strobe light can be used to track them in the tunnel to ensure all of them followed the same trajectory in space. Three different colors are used to distinguish between the three blades. The three taped blades and the additional back-up blades can be seen in Figure 4.2. Blade 1 has orange tape, Blade 2 has green tape, and Blade 3 has gold tape.

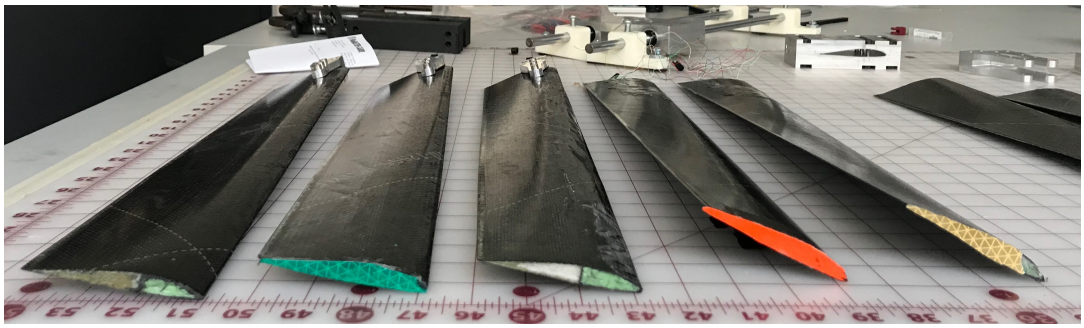

Figure 4.2: Reflective blade tips and extra blades

4.3 Blade Attachment

To attach a blade to the hub, the blade grip is bolted onto the three root insert holes near the root (Figure 4.3). The bolts and nuts are 3/16 inches in diameter. They are tightened using a wrench and Allen wrench.

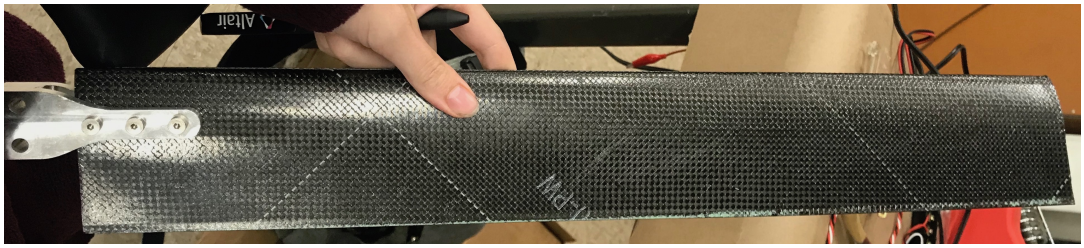

Figure 4.3: Blade grip attached to blade

Once the Maryland Tiltrotor Rig (MTR) is installed in the wind tunnel, a tare run is taken with the blades off to have baseline measurements for the load cell without rotor forces. After the tares runs, the blades are ready to be attached. First, the blades are matched up with their respective pitch case number on the MTR. Blade 1 goes into pitch case 1, Blade 2 goes into pitch case 2, and Blade 3 goes into pitch case 3. The blade grips are bolted into the pitch case using two bolts, a wrench, and an Allen Wrench.

4.4 Strain Gauge Wiring

Once the blades are firmly bolted in, the strain gauge wires are ready to be attached to the printed circuit board (PCB). The PCB transmits the signal to the slip ring, which is then wired under the wind tunnel floor to the DAQ in the control room. There are four channels available in the PCB, so four gauges can be used.

Within each channel, the blade wires are connected as follows (Table 4.1).

Wire Color	Port
Red	Positive Power
Black	Negative Power
Green	Positive Signal
White	Negative Signal

Table 4.1: Strain gauge wire to PCB port list

The flap bending gauges of all three blades are connected, and the torsion gauge of either Blade 1 or Blade 3 is also connected, for a total of four channels used. The correct screwdriver must be used for the small ports of the PCB, and the wires must be clamped into the ports. Once the gauges are wired into the PCB, a multimeter is used to check the voltage across the power ports to make sure it reads the correct voltage, 2.5 V. The multimeter is then used to confirm the correct resistances across the ports. The correct resistance is about 350 Ohm between red and black, and green and white. The correct resistance is about 262 Ohm between red and green or red and white, and black and green or black and white. Once the signal is confirmed, the slack wire is taped with electrical tape to the pitch case so that the wires are not entangled during rotation.

To be prepared for the wind tunnel test, it is important to compile a list of solutions to possible reasons why the signal from the strain gauges are incorrect.

If the correct voltage is not measured across the positive and negative power ports on the PCB on the MTR, the blade is removed, and the voltage is re-checked without the blade. If it is still incorrect, there is a problem with the slip ring connection to those ports in the PCB. If it is correct, the problem must be with the

blade. The non-functional blade blade must be replaced with a back-up blade.

If the correct voltage but the incorrect resistance is measured across the ports on the PCB, the blade is removed, and the resistances are checked at the end of the wires. If the blade shows the correct resistance, the connections are likely bad.

The connection of the strain gauge wires and PCB should be metal only with no plastic casing from the wire obstructing it. If necessary, the wire tips should be cut and stripped to the port length. If the blade still does not show the correct resistance, the non-functional blade is replaced with a back-up blade.

Possible reasons for a non-functional blade are a broken strain gauge, a faulty wiring of the strain gauges, a malfunctioning wire from the Wheatstone bridge.

4.5 Rotor Balance and Track

While the blades are rotating, if the load cell shows a non N_b/rev load, it means that the blade center of gravity is off. This should not happen due to the blades having been tested on the static balance, but if it does, the blades are taken off of the MTR and re-balanced statically.

In addition, the blade tips are tracked by a strobe light to reflect on the tip reflective tapes. The strobe light is set to the frequency of rotation in Hz. If the blades track, the tip colors will all appear at the same location.

Chapter 5: Analysis

This chapter describes the aerodynamic modeling and analysis for the model-scale tiltrotor blades for both a rigid blade and a flexible flapping motion. The concept of autorotation versus freewheeling is discussed, and the trim solution is described in detail.

5.1 Aerodynamic Model

The aerodynamic model consists of uniform inflow and blade element theory coupled with airfoil properties from C81 airfoil decks. The decks cover angle of attacks $\alpha = \pm 180^\circ$ and Mach numbers $M = 0.1 - 1$. The unique trim condition is the axial freewheeling condition. At high inflow ratios typical of tiltrotor, induced inflow vanishes, and a refined wake is unnecessary.

The blade is divided into N number of elements from the root cutout to the tip (R). The radial locations (x) are non-dimensionalized by dividing by the radius R, so the non-dimensional locations of the elements are $r = \frac{x}{R}$ from the non-dimensional root cutout (r_c) to 1. The length of each element is dr. For a uniform distribution, $dr = (1 - r_c)/N$.

The pitch angle θ is calculated at each location r by $\theta = \theta_{75} + \theta_t(r - 0.75)$.

From momentum theory, hover inflow λ_h is defined as $\frac{v_h}{\Omega R} = \sqrt{\frac{C_T}{2}}$. The C_T is initialized to 0.005. Later, inflow and C_T will be iterated until convergence. The tunnel wind speed v_c is non-dimensionalized as cruise inflow $\lambda_c = \frac{v_c}{\Omega R}$. The ratio λ_c/λ_h determines the induced inflow in axial flow (Table 5.1).

λ_c	λ_i	Condition	Solution Method
$\lambda_c \geq 0$	$-\frac{\lambda_c}{2} + \sqrt{\left(\frac{\lambda_c}{2}\right)^2 + \lambda_h^2}$	Climb	Momentum Theory
$-\lambda_h < \lambda_c < 0$	$-\frac{\lambda_c}{2} + \sqrt{\left(\frac{\lambda_c}{2}\right)^2 + \lambda_h^2}$	Vortex Ring State	Extrapolation
$-2\lambda_h < \lambda_c < -\lambda_h$	$\lambda_c\left(0.373\left(\frac{\lambda_c}{\lambda_h}\right)^2 - 1.991\right)$	Windmill Brake State	Empirical
$\lambda_c < -2\lambda_h$	$-\frac{\lambda_c}{2} - \sqrt{\left(\frac{\lambda_c}{2}\right)^2 - \lambda_h^2}$	Descent	Momentum Theory

Table 5.1: Induced inflow equations

A tiltrotor in forward flight is nominally in cruise so $\lambda_c > 0$. The total inflow $\lambda = \lambda_i + \lambda_c$.

To determine the angle of attack of the section, the blade elemental velocities are derived using blade element theory. These velocities can be seen in Figure 5.1.

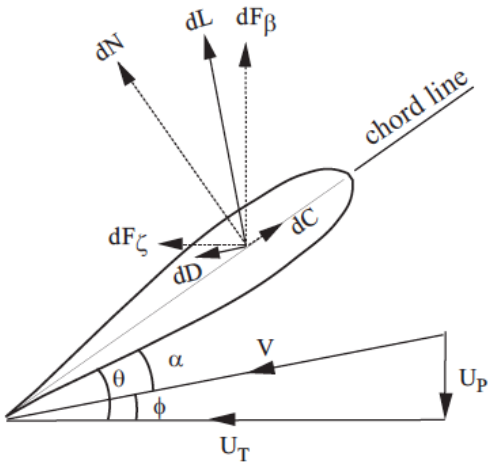

Figure 5.1: Elemental velocity definitions

The tangential velocity (to hub plane) is $U_T = \Omega x$ where x is the radial coor-

dinate in m and Ω is the speed in rad/s. The non-dimensional tangential velocity u_t is r. The perpendicular velocity is $U_P = v_i + v_c$. The non-dimensional perpendicular velocity u_p is λ, where λ is the total inflow. The resultant non-dimensional velocity $u = \sqrt{u_t^2 + u_p^2}$. The inflow angle ϕ of this resultant velocity is $\phi = \tan^{-1} \frac{u_p}{u_t}$. The angle of attack α of the blade is related to the resultant velocity as $\alpha = \theta - \phi$. For linear aerodynamics, the lift coefficient $c_l = 5.73\alpha$ and the drag coefficient c_d is a constant 0.015. For non-linear aerodynamics, C81 airfoil tables are used to get the exact c_l and c_d from a given α and Mach number M. The section Mach number is $M = uM_T$ where M_T is the tip Mach number $\Omega R/a$. ΩR is the tip speed, and a is the speed of sound.

The elemental coefficient of thrust is $dC_T = \frac{1}{2}\sigma u^2 \left(c_l \cos\phi - c_d \sin\phi\right) dr$. The elemental coefficient of power is $dC_P = \frac{1}{2}\sigma u^2 \left(c_l \sin\phi + c_d \cos\phi\right) r dr$. Integration over r produces the total rotor C_T and C_P. This C_T is used to update λ_h and iterate until C_T converges within 1×10^{-4}.

The two-dimensional (2D) CFD deck available from UMD TURNS code was used. The c_l , c_d, and c_m (about the quarter chord) for the CFD VR-7 airfoil are shown in Figures 5.2, 5.3, and 5.4, respectively.

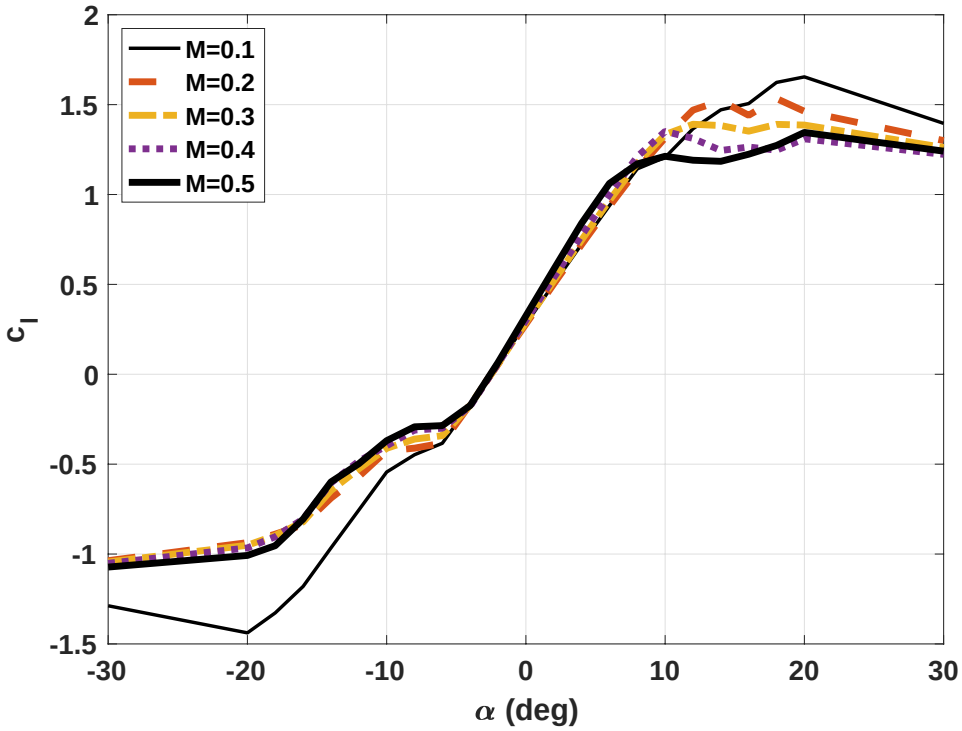

Figure 5.2: CFD VR-7 c_l Versus α at $M = 0.1 - 0.5$

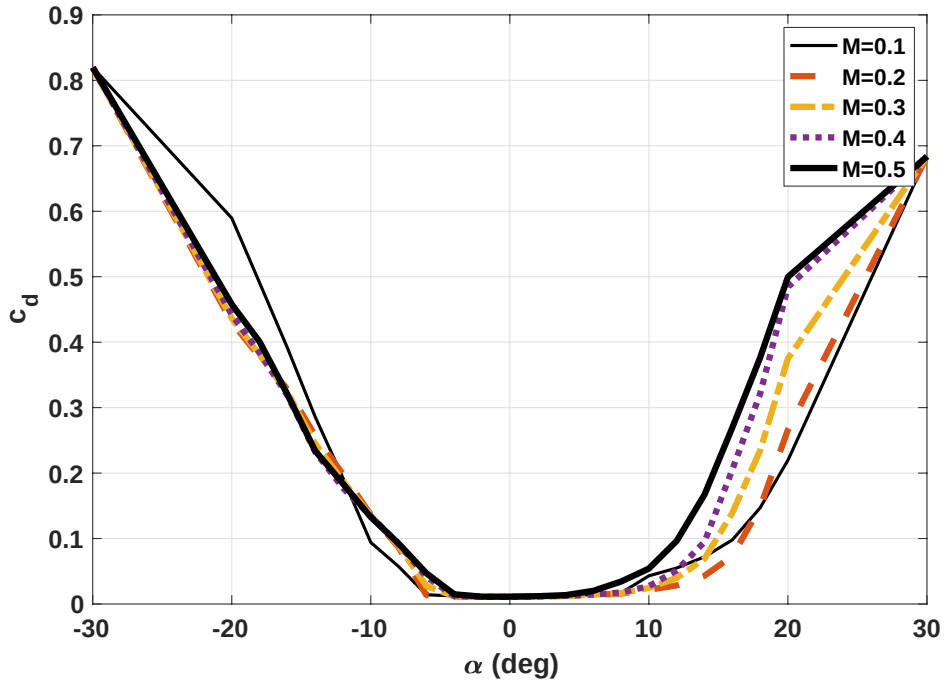

Figure 5.3: CFD VR-7 c_d Versus α at $M = 0.1 - 0.5$

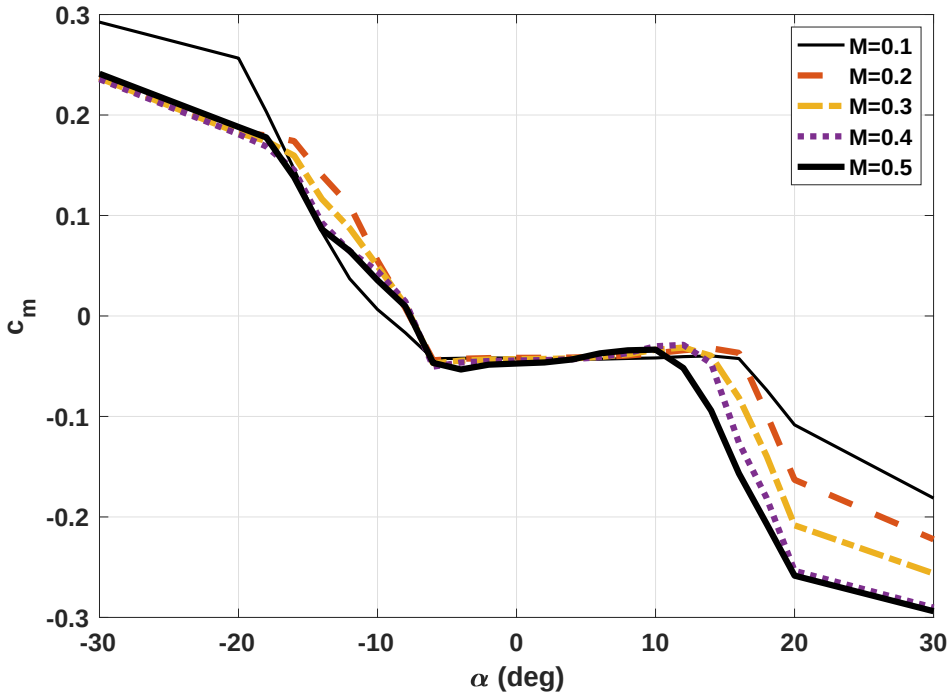

Figure 5.4: CFD VR-7 c_m Versus α at $M = 0.1 - 0.5$

In addition, a 2D VR-7 airfoil deck from NASA Ames was used for comparison, and that deck will now be referred to as the Ames VR-7 airfoil deck. The c_l , c_d, and c_m for the Ames VR-7 airfoil are shown in Figures 5.5, 5.6, and 5.7, respectively.

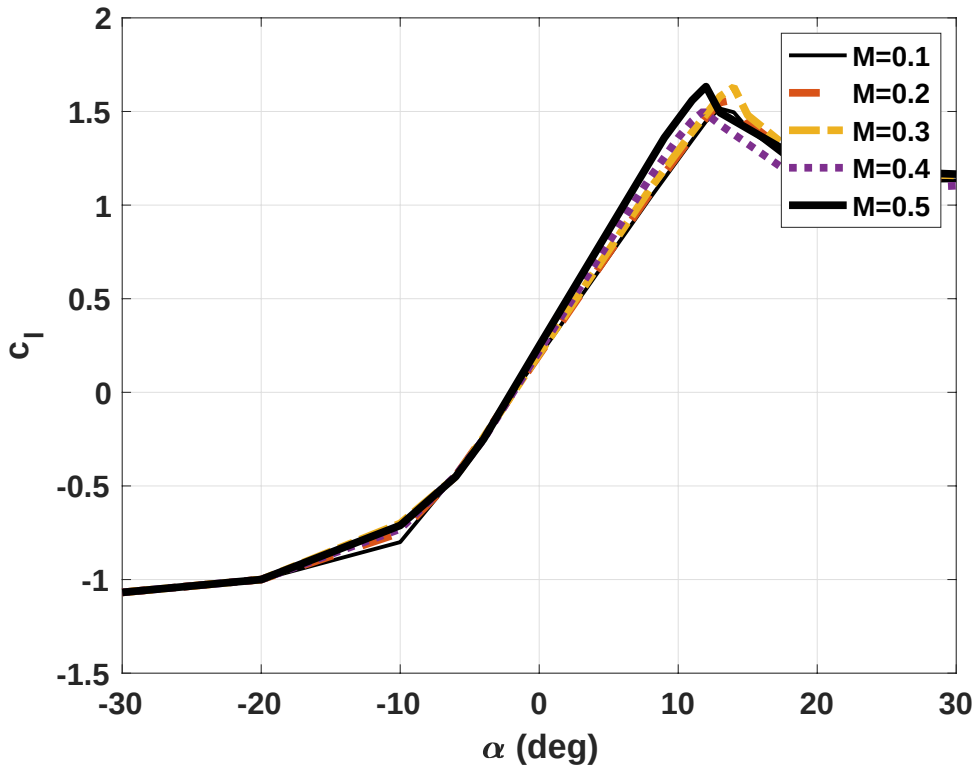

Figure 5.5: Ames VR-7 c_l Versus α at $M = 0.1 - 0.5$

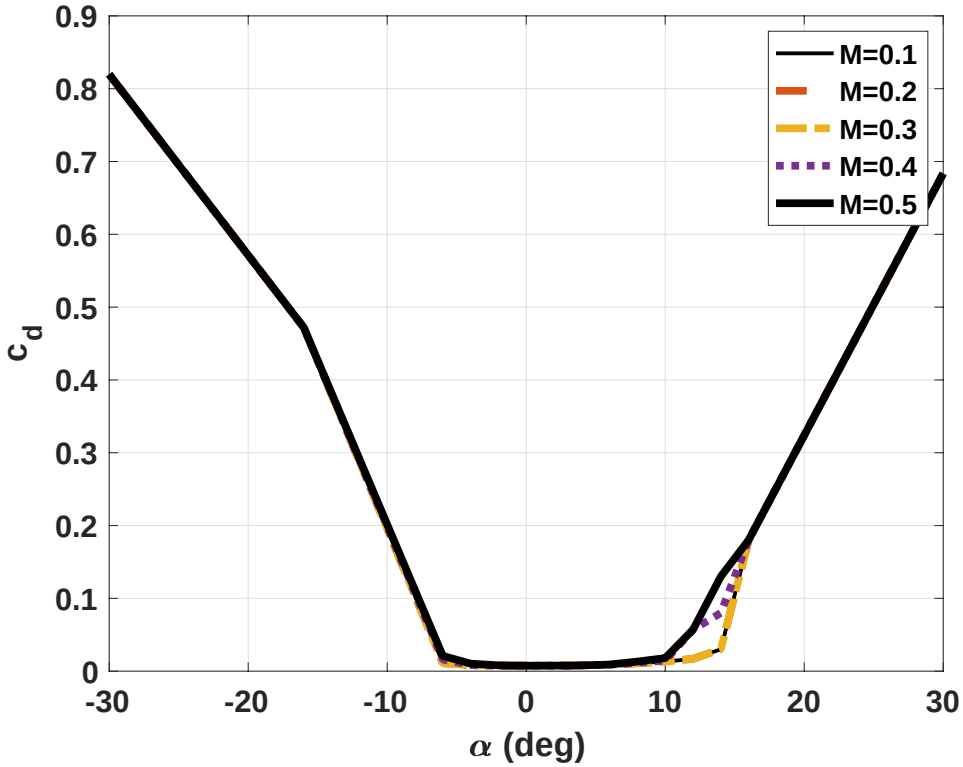

Figure 5.6: Ames VR-7 c_d Versus α at $M = 0.1 - 0.5$

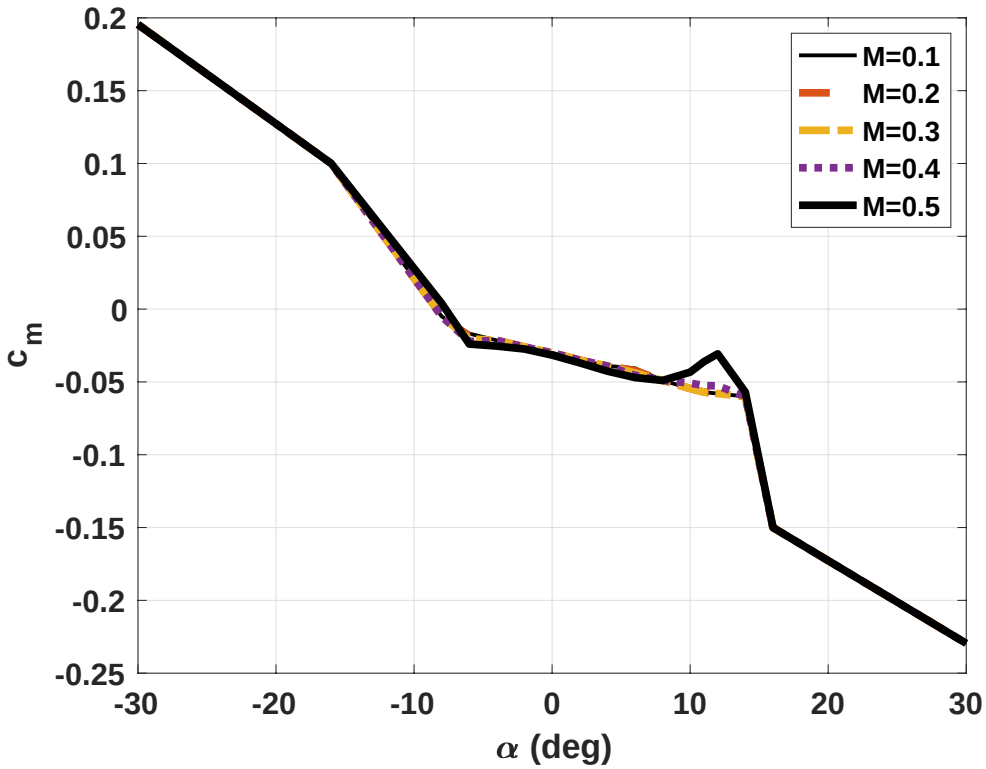

Figure 5.7: Ames VR-7 c_m Versus α at $M = 0.1 - 0.5$

Compared to the CFD VR-7 airfoil deck properties, the Ames VR-7 airfoil deck properties vary much less with Mach number, with almost no variance. The linear portion of the Ames deck c_l covers more collectives than the CFD deck, ranging from $-10° - 10°$ versus $-5° - 7°$ respectively.

5.2 Blade Flapping

The blade is modeled as a beam with only flapping motion. It is divided into N_e finite elements of length l between the dimensional root cutout x_c and the tip R, which can be seen in Figure 5.8.

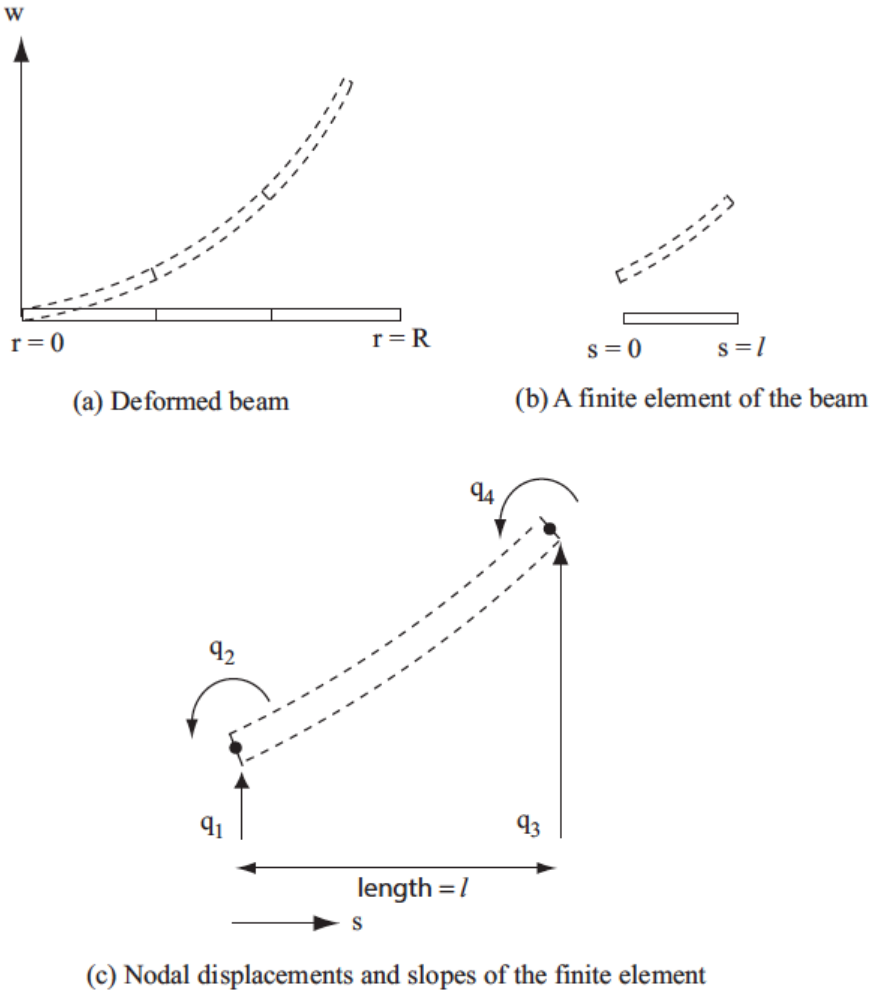

Figure 5.8: Finite element definition

The equation of motion for a rotating beam with flapwise forcing per span f in N/m is

$$m\ddot{w} + (EIw'')'' - (Tw')' = f(x,t)$$

where w is the vertical displacement of the blade as a function of space (x) and time (t). The second time derivative of w is $\ddot{w} = \frac{d^2w}{dt^2}$, and the spatial derivative of w is $w' = \frac{dw}{dx}$. m is the spanwise mass (kg/m), and EI is the flap stiffness in

Nm^2.

A finite element method is used to find the solution to the equation of motion. The displacement within each element is defined as a third order polynomial as:

$$w(s,t) = \alpha_0 + \alpha_1 s + \alpha_2 s^2 + \alpha_3 s^3$$

where t is time and s is the internal distance along the element.

The displacement and slope on one end of the blade are assumed to be q_1 and q_2 respectively, and those on the other are q_3 and q_4 (Figure 5.8(c)). Thus, the spacial boundary conditions are inserted into this equation and its derivative:

$$q_1 = w(0,t) = \alpha_0$$

$$q_2 = w'(0,t) = \alpha_1$$

$$q_3 = w(l,t) = \alpha_0 + l\alpha_1 + l^2\alpha_2 + l^3\alpha_3$$

$$q_4 = w'(l,t) = \alpha_1 + 2l\alpha_2 + 3l^2\alpha_3$$

Then, the coefficients α can be evaluated in terms of q.

$$\alpha_0 = q_1$$

$$\alpha_1 = q_2$$

$$\alpha_2 = \frac{3q_3}{l^2} - \frac{3q_1}{l^2} - \frac{2q_2}{l} - \frac{q_4}{l}$$

$$\alpha_3 = \frac{q_4}{l^2} - \frac{2q_3}{l^3} + \frac{2q_1}{l^3} + \frac{q_2}{l^2}$$

Inserting the coefficients into the polynomial, it can be written as follows:

$$\begin{aligned} w(s,t) &= \left(1 - \frac{3s^2}{l^2} + \frac{2s^3}{l^3}\right) q_1 + \left(s - \frac{2s^2}{l} + \frac{s^3}{l^2}\right) q_2 \\ &+ \left(\frac{3s^2}{l^2} - \frac{2s^3}{l^3}\right) q_3 + \left(\frac{s^3}{l^2} - \frac{s^2}{l}\right) q_4 \\ &= H_1 q_1 + H_2 q_2 + H_3 q_3 + H_4 q_4 \end{aligned}$$

or

$$w(s,t) = \sum_{i=1}^{4} H_i(s) q_i(t)$$

Thus the displacement within each element is expanded as Hermite polynomials in space multiplied by the end displacements and slopes. The displacements and slopes vary with time and are called the states or degrees of freedom.

The mass, stiffness and force matrices are calculated for each element using the Rayleigh-Ritz method.

The kinetic energy of the element is:

$$V_e = \frac{1}{2} \int_0^l m\dot{w}^2 ds = \sum_{i=1}^{4} \sum_{j=1}^{4} m_{ij} \dot{q}_i \dot{q}_j$$

where

$$m_{ij} = \int_0^l m H_i H_j ds$$

are the entries of the element mass matrix M_e.

The potential energy is:

$$U_e = \frac{1}{2}\int_0^l EIw''^2 ds + \frac{1}{2}\int_0^l Tw'^2 ds = \sum_{i=1}^{4}\sum_{j=1}^{4} k_{ij}q_i q_j$$

where

$$k_{ij} = \int_0^l EI\frac{d^2H_i}{ds^2}\frac{d^2H_j}{ds^2}ds + \int_0^l T\frac{dH_i}{ds}\frac{dH_j}{ds}ds$$

are the entries of the element stiffness matrix K_e. The tension force T is an integral on its own:

$$T(s) = \int_{x_i+s}^{R} m\Omega^2\rho d\rho$$

where x_i is the distance from the axis of rotation to the left edge of element i.

The EI term is the bending stiffness, and the T term is the centrifugal stiffness from rotation. The force vector is derived from the external virtual work, which is given as:

$$\delta W = \int_0^l f\delta w(s,t) = \sum_{i=1}^{4} Q_i\delta q_i$$

where

$$Q_i = \int_0^l fH_i ds$$

are the entries to the element force matrix Q_e.

All integrations are performed numerically using the Gaussian quadrature. The Gaussian quadrature is defined as:

$$\int_{-1}^{1} f(x)dx \approx \sum_{i=1}^{n} w_i f(x_i)$$

for exact integration of a polynomial f of the order $2n-1$. Here, $n=4$ is used, that covers up to a 7th order polynomial. For $n=4$, the points x_i are

$$\pm\sqrt{\frac{3}{7}-\frac{2}{7}\sqrt{\frac{6}{5}}}, \pm\sqrt{\frac{3}{7}+\frac{2}{7}\sqrt{\frac{6}{5}}}$$

and the corresponding weights w_i are

$$\frac{18+\sqrt{30}}{36}, \frac{18+\sqrt{30}}{36}, \frac{18-\sqrt{30}}{36}, \frac{18-\sqrt{30}}{36}$$

respectively. To change the limits of the integral from [-1 1] to [a b] (integrating over the length of an element [0 l]), the following shift is performed:

$$\int_a^b f(x)dx \approx \frac{b-a}{2}\sum_{i=1}^{4} w_i f\left(\frac{b-a}{a}x_i+\frac{b-a}{2}\right) = \frac{l}{2}\sum_{i=1}^{4} w_i f\left(\frac{l}{2}x_i+\frac{l}{2}\right)$$

The elemental mass, stiffness, and force matrices are then assembled into their respective global matrices for the entire blade. The mass and stiffness matrices have dimensions $[2N_e+2, 2N_e+2]$, and the force vector has the dimension $[2N_e+2]$, where N_e is the number of elements.

Finally, the boundary conditions are applied depending on the type of rotor. An articulated rotor has zero deflection at the root, so $w(0)=0$, hence $q_1=0$. This means the first row and column of the global mass and stiffness matrices and the first term of the force vector can be deleted. These matrices now have dimensions of $[2N_e+1, 2N_e+1]$ and $[2N_e+1]$ respectively. The q vector for an articulated rotor also therefore has the dimension $[2N_e+1]$.

A hingeless rotor has zero deflection and zero slope at the root so $w(0) = 0$ and $w'(0) = 0$, hence $q_1 = 0$ and $q_2 = 0$. This means that the first and second rows and columns of the mass and stiffness matrices and the first and second terms of the force vector can be deleted. These matrices now have dimensions of $[2N_e, 2N_e]$ and $[2N_e]$ respectively. The q vector for a hingeless rotor has dimensions of $[2N_e]$.

A gimbaled rotor, like the MTR, has a boundary condition that is a combination of articulated and hingeless rotors. It behaves as a hingeless rotor for steady and pN_b/rev deflections and as an articulated rotor for all other harmonics. The focus of the research is in steady flow, where only steady deflections are produced, so a hingeless rotor model suffices.

5.3 Natural Frequency

The final equation to solve is $M\ddot{q} + Kq = Q$, where the matrices have the dimensions $N = 2N_e$ for a hingeless rotor.

The natural frequencies are calculated by setting $Q = 0$ and seeking a solution in the form of $q = q_0 e^{st}$. The eigenproblem to solve is $(K - s^2 M)q_0 = 0$, where s is the eigenvalue and q_0 is the eigenvector or mode. There are N pairs of complex conjugate roots. Both the K and M matrices are symmetric and positive definite, so these roots are purely imaginary and give N natural frequencies.

To reduce the problem size from N to say m, m eigenvectors are taken and are arranged column-wise to construct a matrix V of dimensions [N, m]. New degrees of freedom η are introduced which are related to the original degrees of freedom

by $q = V\eta$. Substituting $V\eta$ into the final equation and pre-multiplying by V^T produces the modal equation with reduced mass and stiffness matrices and reduced force vector. The reduced mass and stiffness matrices become $\overline{M} = V^T M V$ and $\overline{K} = V^T K V$ respectively. The reduced force vector becomes $\overline{Q} = V^T Q$. The new equation to solve is $\overline{M}\ddot{\eta} + \overline{K}\eta = \overline{Q}$. For a symmetric and positive definite system, $\overline{M}$ and $\overline{K}$ are diagonal and create m uncoupled equations. Thus η can be solved for instead of q if only a few modes are of interest.

5.4 Time Response

The time response is found using implicit two-point backward Euler method. The velocity is found at the time $t+1$ by taking the following time derivative of the position.

$$\dot{q}_{t+1} = \frac{q_{t+1} - q_t}{\Delta t}$$

The acceleration is found at $t+1$ by taking the following time derivative of the velocity. It can be rewritten as a function of position and the current time (hence implicit) and two previous time steps (hence two point backward).

$$\begin{aligned}
\ddot{q}_{t+1} &= \frac{\dot{q}_{t+1} - \dot{q}_t}{\Delta t} \\
&= \frac{\frac{q_{t+1}-q_t}{\Delta t} - \frac{q_t - q_{t-1}}{\Delta t}}{\Delta t} \\
&= \frac{q_{t+1} - 2q_t + q_{t-1}}{\Delta t^2}
\end{aligned}$$

The equation then becomes

$$M\left(\frac{q_{t+1}-2q_t+q_{t-1}}{\Delta t^2}\right)+Kq_{t+1}=Q_{t+1}$$

The mass matrix is constant. The stiffness matrix is constant for a constant Ω. The forcing vector is also constant in cruise, but only when steady state is reached. Thus, in general,

$$\left[\frac{M}{\Delta t^2}+K\right]q_{t+1}=Q_{t+1}+\frac{2M}{\Delta t^2}q_t-\frac{M}{\Delta t^2}q_{t-1}$$

Q is a function of q as the response changes the angle of attack and forcing.

Once q is found, it can be reassembled to obtain deflections within each element as $w(s,t)=\sum_{i=1}^{4}H_i(s)q_i(t)$. The strain at a specified location is $\epsilon=zw''$, where ϵ is the bending strain, z is the distance from the neutral axis to the strain gauge location in the flapwise direction and w'' is the second spatial derivative of the deflection with respect to radial location. Since the neutral axis for bending strain is the center of thickness, the distance to the skin where the strain is measured is $z=t/2$ where t is the thickness. The second derivative of the deflection (w'') is found by

$$w''=\frac{d^2w}{dx^2}=\sum_{i=1}^{4}H_i''(s)q_i(t)$$

5.5 Angle of Attack

Blade flexibility changes the angle of attack. It is found as follows.

First, the hub frame H is defined with the origin at the center of rotation. Then, a rotating frame R is defined at an azimuth angle ψ relative to the hub frame aces. This is also the undeformed frame U. The unit vectors of the undeformed frame relate to the unit vectors of the hub frame as

$$\begin{pmatrix} \hat{i} \\ \hat{j} \\ \hat{k} \end{pmatrix} = \begin{pmatrix} \cos\psi & \sin\psi & 0 \\ -\sin\psi & \cos\psi & 0 \\ 0 & 0 & 1 \end{pmatrix} \begin{pmatrix} i_H \\ j_H \\ k_H \end{pmatrix} = C^{UH} \begin{pmatrix} i_H \\ j_H \\ k_H \end{pmatrix}$$

The blade is placed so that its 0.25 c line passes through the x-axis of the undeformed frame. Next, the deformed blade frame is defined with the origin at $(x+u)\hat{i}$. This frame is rotated by local blade pitch (pitch θ_c + twist θ_t) and the flap slope w' relative to the undeformed blade frame. The unit vectors in the deformed frame relate to the undeformed frame as:

$$\begin{pmatrix} i_\xi \\ j_\eta \\ k_\zeta \end{pmatrix} = \begin{pmatrix} \cos w' & 0 & \sin w' \\ -\sin w' \sin\theta & \cos\theta & \cos w' \sin\theta \\ -\sin w' \cos\theta & -\sin\theta & \cos w' \cos\theta \end{pmatrix} \begin{pmatrix} \hat{i} \\ \hat{j} \\ \hat{k} \end{pmatrix} = C^{DU} \begin{pmatrix} \hat{i} \\ \hat{j} \\ \hat{k} \end{pmatrix}$$

A point on the blade cross section has the position of:

$$\overrightarrow{r} = (x+u)\hat{i} + w\hat{k} + \eta j_\eta + \zeta k_\zeta$$

where u is the axial displacement of the section, w is the vertical (flap) displacement, and η and ζ are cross-sectional coordinates. For the angle of attack, the velocity at 0.75 c is needed, so $\zeta = 0$ and $\eta = -0.5c$. The position of this point is

$$\begin{aligned}
\overrightarrow{r} &= \begin{pmatrix} \hat{i} \\ \hat{j} \\ \hat{k} \end{pmatrix}^T \begin{pmatrix} x+u \\ 0 \\ w \end{pmatrix} + \begin{pmatrix} i_\xi \\ j_\eta \\ k_\zeta \end{pmatrix}^T \begin{pmatrix} 0 \\ \eta \\ 0 \end{pmatrix} \\
&= \begin{pmatrix} \hat{i} \\ \hat{j} \\ \hat{k} \end{pmatrix}^T \begin{pmatrix} x+u \\ 0 \\ w \end{pmatrix} + \begin{pmatrix} \hat{i} \\ \hat{j} \\ \hat{k} \end{pmatrix}^T C^{UD} \begin{pmatrix} 0 \\ \eta \\ 0 \end{pmatrix} \\
&= \begin{pmatrix} \hat{i} \\ \hat{j} \\ \hat{k} \end{pmatrix}^T \begin{bmatrix} x+u-\eta \sin w' \sin\theta \\ \eta \cos\theta \\ w+\eta \cos w' \sin\theta \end{bmatrix}
\end{aligned}$$

To get the blade velocities in the undeformed frame, the time derivative of the position is taken.

$$\dot{\overrightarrow{r}} = \begin{pmatrix} \hat{i} \\ \hat{j} \\ \hat{k} \end{pmatrix}^T \begin{bmatrix} \dot{u} - \eta \dot{w}' \cos w' \sin\theta - \eta\dot{\theta} \sin w' \cos\theta \\ -\eta\dot{\theta}\sin\theta \\ \dot{w} - \eta\dot{\theta}\cos\theta \end{bmatrix}$$

u is small, so the u and $\dot{u} = 0$ terms are dropped. There are no cyclics, so $\dot{\theta} = 0$. The blade velocity in the undeformed frame then simplifies to:

$$\dot{\overrightarrow{r}} = \begin{pmatrix} \hat{i} \\ \hat{j} \\ \hat{k} \end{pmatrix}^T \begin{bmatrix} -\eta \dot{w}' \cos w' \sin\theta \\ 0 \\ \dot{w} \end{bmatrix}$$

To transform the blade velocities to the hub frame, the rotation of the frame is incorporated.

$$\begin{aligned} \dot{\overrightarrow{r}}^H &= \dot{\overrightarrow{r}} + \overrightarrow{\Omega} \times \overrightarrow{r} \\ &= \begin{pmatrix} \hat{i} \\ \hat{j} \\ \hat{k} \end{pmatrix}^T \begin{bmatrix} -\eta \dot{w}' \cos w' \sin\theta \\ 0 \\ \dot{w} \end{bmatrix} \\ &+ \begin{pmatrix} \hat{i} \\ \hat{j} \\ \hat{k} \end{pmatrix}^T \begin{bmatrix} 0 \\ 0 \\ \Omega \end{bmatrix} \times \begin{pmatrix} \hat{i} \\ \hat{j} \\ \hat{k} \end{pmatrix}^T \begin{bmatrix} x + u - \eta \sin w' \sin\theta \\ \eta \cos\theta \\ w + \eta \cos w' \sin\theta \end{bmatrix} \end{aligned}$$

In deformed coordinates, it produces

$$\dot{\overrightarrow{r}}^H = \begin{pmatrix} i_\xi \\ j_\eta \\ k_\zeta \end{pmatrix}^T C^{DU} \begin{bmatrix} -\eta \dot{w}' \cos w' \sin\theta - (\eta \cos\theta)\Omega \\ (x + u - \eta \sin w' \sin\theta)\Omega \cos\beta_P \\ \dot{w} \end{bmatrix}$$

In axial flight, the wind velocity is only from inflow. In the hub frame, the

wind velocity is

$$v_{wind}^{H} = \begin{pmatrix} \hat{i} \\ \hat{j} \\ \hat{k} \end{pmatrix}^{T} \begin{bmatrix} 0 \\ 0 \\ -\lambda\Omega R \end{bmatrix}$$

or

$$v_{wind}^{H} = \begin{pmatrix} i_{\xi} \\ j_{\eta} \\ k_{\zeta} \end{pmatrix}^{T} C^{DU} \begin{bmatrix} 0 \\ 0 \\ -\lambda\Omega R \end{bmatrix}$$

The net velocities in deformed coordinates are

$$\begin{pmatrix} U_R \\ U_T \\ U_P \end{pmatrix} = \dot{\overrightarrow{r_P}}^{H} - v_{wind}^{H}$$

where U_R is the radial velocity, U_T is the velocity tangent to the chord, and U_P is the velocity perpendicular to the chord. The angle of attack is then simply

$$\alpha = \tan^{-1} \frac{U_P}{U_T}$$

The Mach number M is calculated using the resultant velocity $U = \sqrt{U_P^2 + U_T^2}$ divided by the speed of sound a.

$$M = \frac{U}{a}$$

Spanwise lift and drag are defined as:

$$dL = \frac{1}{2}\rho U^2 c_l c dr$$

$$dD = \frac{1}{2}\rho U^2 c_d c dr$$

where c_l and c_d are from the airfoil deck and c is the chord. The horizontal and vertical spanwise forces in the deformed frame are defined as:

$$f_\eta = dL \sin\alpha - dD \cos\alpha$$

$$f_\zeta = dL \cos\alpha + dD \sin\alpha$$

In the undeformed frame

$$\begin{pmatrix} f_x \\ f_y \\ f_z \end{pmatrix} = C^{UD} \begin{pmatrix} 0 \\ f_\eta \\ f_\zeta \end{pmatrix}$$

5.6 Autorotation Versus Freewheeling

Autorotation and freewheeling are conditions in descent and cruise (for proprotors) where the rotor operates at zero torque. The coefficient of torque from momentum theory is defined as $C_Q = C_P = \lambda C_T + C_{P0}$. Consider an ideal case—zero drag, so $C_{P0} = 0$. Now given $C_P = \lambda C_T = 0$, there are two cases in which torque (or power) can be zero: $\lambda = 0$ or $C_T = 0$. For an edgewise rotor, $C_T \neq 0$

because $C_T = C_W$ for thrust must equal the weight, so $\lambda = 0$ at zero power. This condition is defined as autorotation. In a proprotor, $\lambda \neq 0$ since $\lambda = \lambda_i + \lambda_c$ where λ_c is the speed ratio, cruise speed divided by tip speed. Therefore, $C_T = 0$. This condition is defined as freewheeling. The MTR rotor operates in cruise and therefore freewheeling represents the zero torque condition. Here, $C_T = 0$ is an ideal case, but slightly negative $C_T = -C_{P0}/\lambda$ is a practical case. Thus, the thrust is negative, and the airfoils are operating at negative angles of attack.

5.7 Prediction of Freewheeling

Using uniform inflow, blade element aerodynamics and the flexible flapping model, the freewheeling prediction is now predicted. At a fixed blade pitch, the rotor thrust and power can be predicted at a range of RPMs. Figure 5.9 shows the thrust predicted by varying RPM from 500-3000. Two cases are shown: for climb of 25 knots and descent of -25 knots. Each case is modeled with two different collectives: $\theta_{75} = 10°$ (solid lines) and $\theta_{75} = 30°$ (dotted lines).

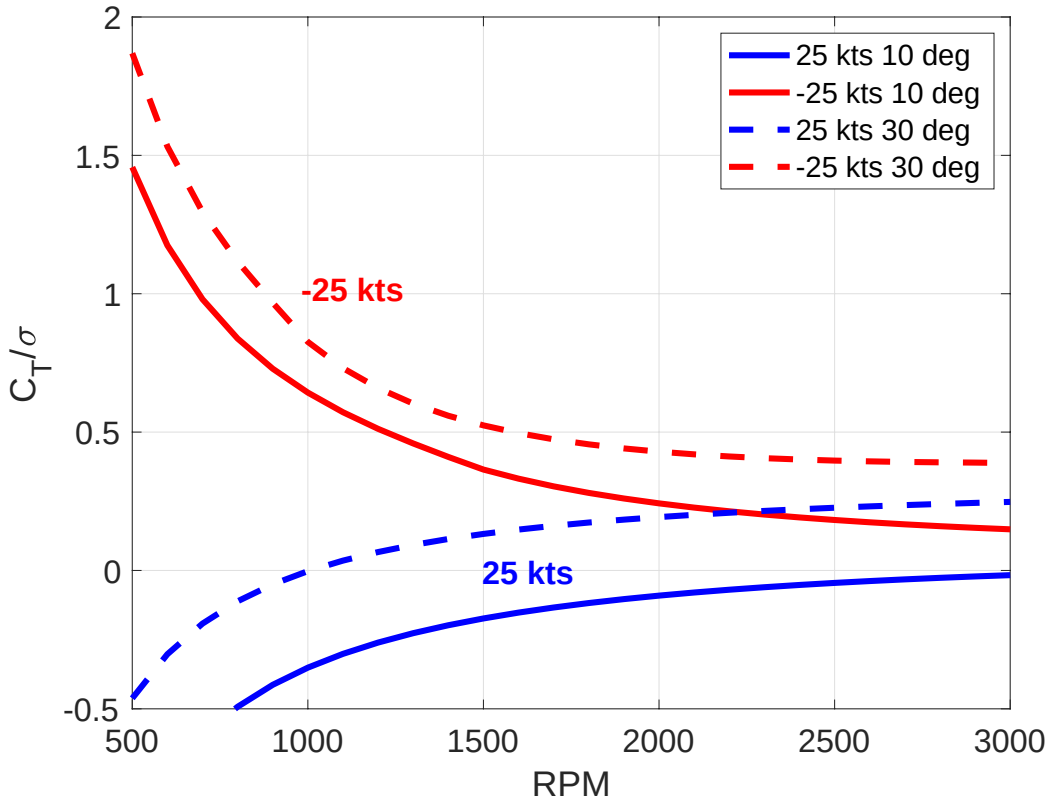

Figure 5.9: C_T/σ versus RPM at ± 25 knots and $\theta_{75} = 10°$ and $30°$

The rotor in climb acts as freewheeling because the climb predictions cross $C_T = 0$ while the descent predictions do not.

Both of these conditions can lead to zero torque, as seen in Figure 5.10. The climb lines represent freewheeling, and the descent lines represent autorotation.

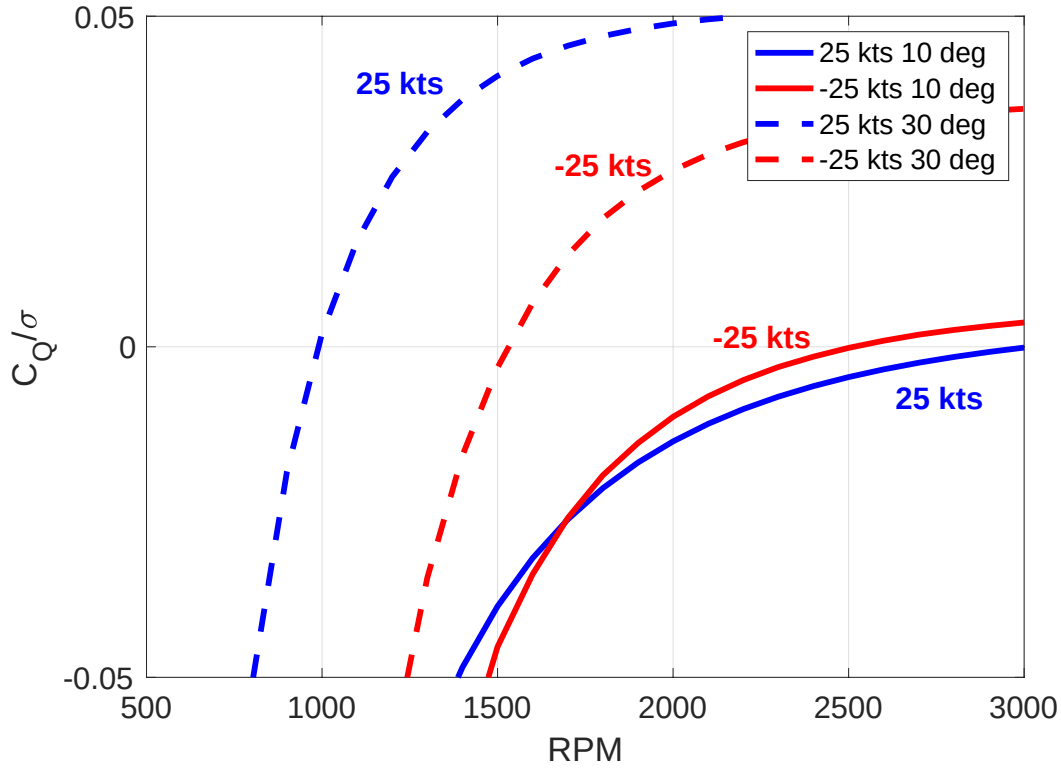

Figure 5.10: C_Q/σ versus RPM at ± 25 knots and $\theta_{75} = 10°$ and $30°$

Only the climb predictions reach zero torque near $C_T = 0$ or a slightly negative C_T. The climb predictions cross C_Q/σ and C_T/σ at similar RPM, confirming that the rotor in climb speeds represents freewheeling.

5.8 Freewheeling Trim Solution

A simple trim solution is developed to calculate the zero torque solution directly instead of sweeping over RPM and finding them manually. This is described below.

At a specified tunnel speed and collective, the zero torque RPM is calculated as follows. First, an initial RPM (RPM_0 of say 1000) is assumed. Iterations are

performed to converge inflow and thrust. Once converged, the rotor power P_0 is calculated. Alternatively, Q_0 could be calculated, but since $P_0 = \Omega Q_0$, the power is more sensitive to Ω, and it is easier numerically to identify zero power.

A second RPM is defined as $RPM_1 = RPM_0 + \Delta$ where Δ is 1% of RPM_0. The new rotor power P_1 is calculated using RPM_1. The change in power is $P_1 - P_0$. The Jacobian, just one term in this case, is $J = \frac{P_1 - P_0}{RPM_1 - RPM_0}$. The error of P_0 to the target power (P_{target}) is $\epsilon = \frac{P_0}{1+P_0}$. This error definition is used because if P_0 was the sole term in the denominator, the error would approach infinity as power approached zero. If the error converges to less than 1×10^{-4}, the loop ends, and the RPM is stored. If $\epsilon > 1 \times 10^{-4}$, the RPM is updated using the Jacobian. The updated RPM is obtained as $RPM + \Delta RPM$ where $P_{target} = P_0 + J\Delta RPM$. Rearranging, this gives $\Delta RPM = \frac{P_{target} - P_0}{J}$. As $P_{target} = 0$, the updated RPM becomes $RPM_0 - \frac{P_0}{J}$. At the updated RPM, the updated power is found and the process repeats. The Jacobian J is kept fixed. Thus, this is the modified Newton method. The Jacobian could be updated if needed, which would then make it the Newton-Raphson method. This was not necessary.

Chapter 6: FSD Results

This chapter discusses the analytical and experimental results of the flutter system development (FSD) rig, which can be seen in the Glenn L. Martin Wind Tunnel in Figure 6.1.

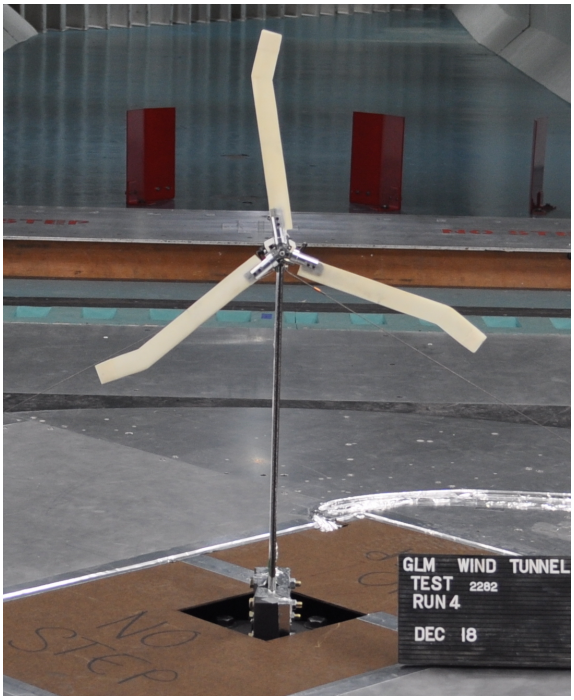

Figure 6.1: FSD in the Glenn L. Martin Wind Tunnel

6.1 Experimental Data

The data collected from the FSD freewheeling test in the Glenn L. Martin Wind Tunnel is listed in Table 6.1 and plotted in Figure 6.2.

θ_{75} (deg)	$v_c = 12$ kts up	$v_c = 12$ kts down	$v_c = 25$ kts	$v_c = 32$ kts
		Ω (RPM)		
0			35	
1			135	613
2			647	625
3	180		580	830
4			630	960
5	460	228	835	1225
6	720	335	1148	1730
7	775	490	1335	1780
8	848	655	1530	
9	850	780		
10	867	850		
11		875		

Table 6.1: FSD freewheeling experimental data for tunnel speeds of 12 kts, 25 kts, and 32 kts

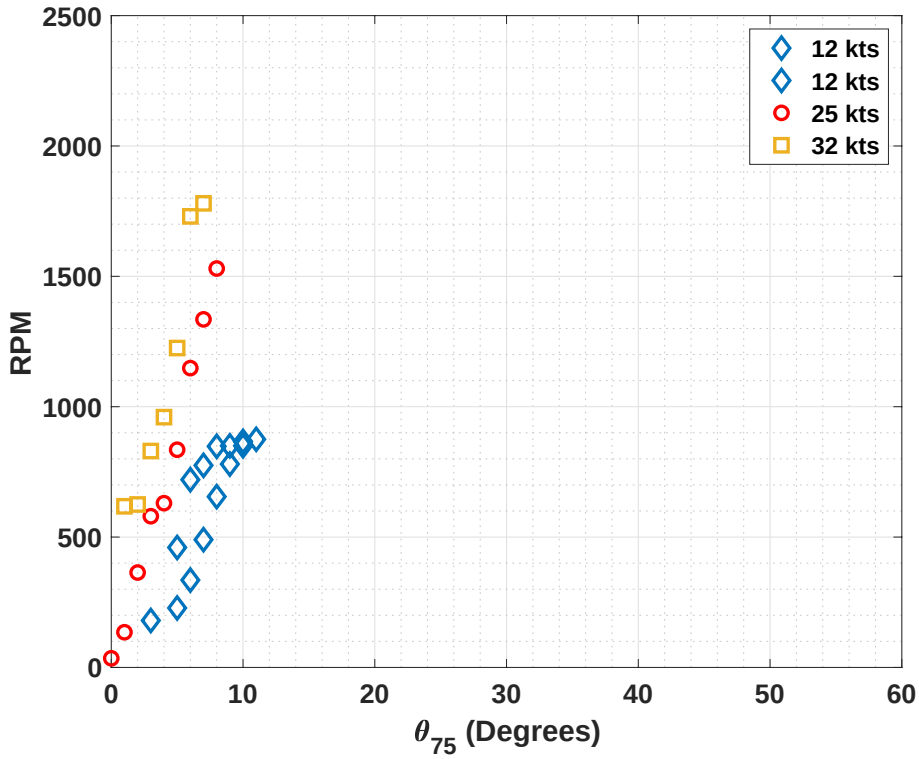

Figure 6.2: FSD freewheeling RPM data for tunnel speeds of 12 kts, 25 kts, and 32 kts

The 12 knot data was taken twice, once going up in collective and then going

down, and the hysteresis from free play in the pitch links gave two sets of RPMs for a given collective. As the collective increases, the RPM increases for all wind speeds. As the wind speed increases, the RPM for a given collective also increases.

6.2 Model Inputs

The FSD was modeled to compare predictions against the experimental data. The model parameters are shown in Table 6.2. EI_N is the blade normal stiffness, N_b is number of blades, R is the rotor radius, x_c is the non-dimensional root cutout, σ is blade solidity, ρ is air density, m is the spanwise mass of the blades, θ_t is the spanwise twist, and c is the chord measurement.

Parameters	**Value**
EI_N (Nm^2)	
N_b	3
R (m)	0.3048
x_c	0.1
σ	0.1
ρ (kg/m^3)	1.225
m (kg/m)	
θ_t $(^\circ/span)$	-45
c (m)	0.0355
Hub Type	Spherical Joint
Airfoil	VR-7

Table 6.2: Model inputs for Flutter System Development (FSD) rig

The FSD was analyzed with aerodynamics only. The EI_N and m measurements were not available.

6.3 Model Results

First, all predictions are calculated at a tunnel speed of 25 knots. For a specified collective θ_{75}, the RPM is swept from 500 to 3000. At each condition, the inflow is iterated to converge the thrust C_T. The predicted torque C_Q/σ for $\theta_{75} = 5°, 10°, 20°, 30°$ versus RPM can be seen in Figure 6.3.

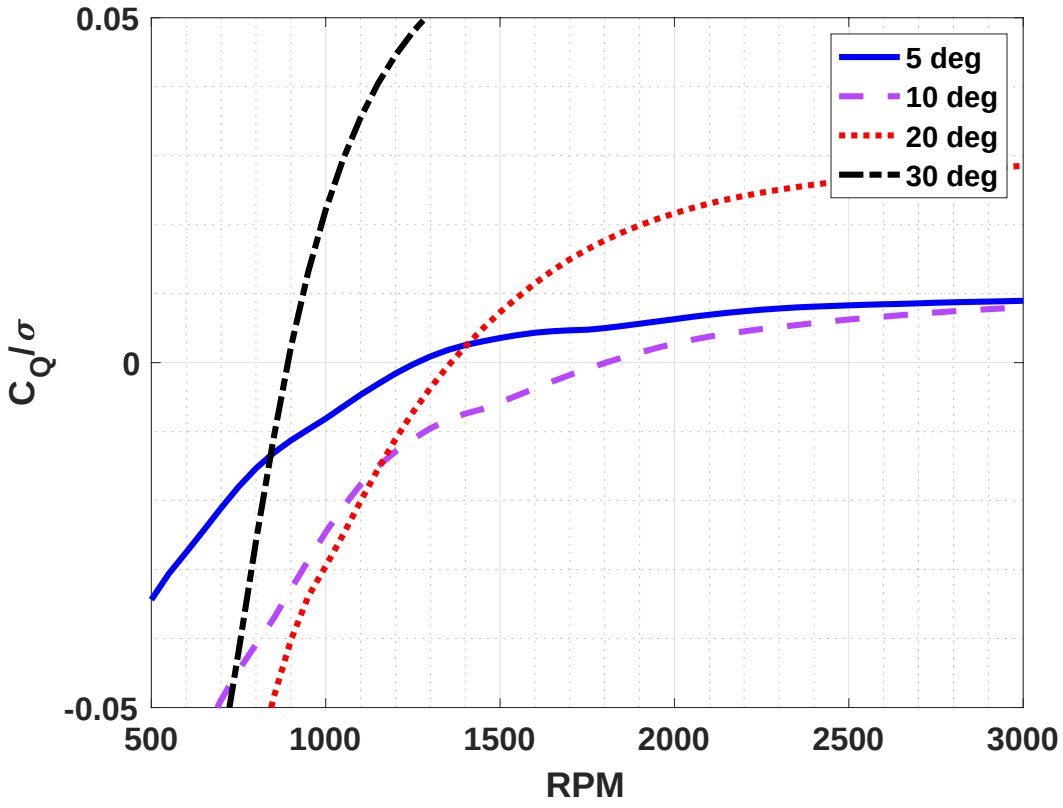

Figure 6.3: FSD C_Q/σ Versus RPM

All collectives have increasing C_Q/σ as RPM increases, though 5° has the lowest slope while 30° has the highest slope. As collective increases, the RPM at which C_Q/σ crosses zero first increases from the collective 5° until 10°, but then decreases as collective increases. The 5° collective line starts at negative torque, crosses

$C_Q/\sigma = 0$ at 1250 RPM, and continues positively thereafter. The 10° collective line starts at negative torque, crosses $C_Q/\sigma = 0$ at 1800 RPM, and continues positively thereafter. Similarly, the 20° collective line starts negative, crosses $C_Q/\sigma = 0$ at 1400 RPM, and continues positively thereafter. The 30° collective line also follows the same trend. It crosses $C_Q/\sigma = 0$ at 900 RPM, and continues positively thereafter.

The corresponding C_T/σ is plotted versus RPM for $\theta_{75} = 5°, 10°, 20°, 30°$ in Figure 6.4.

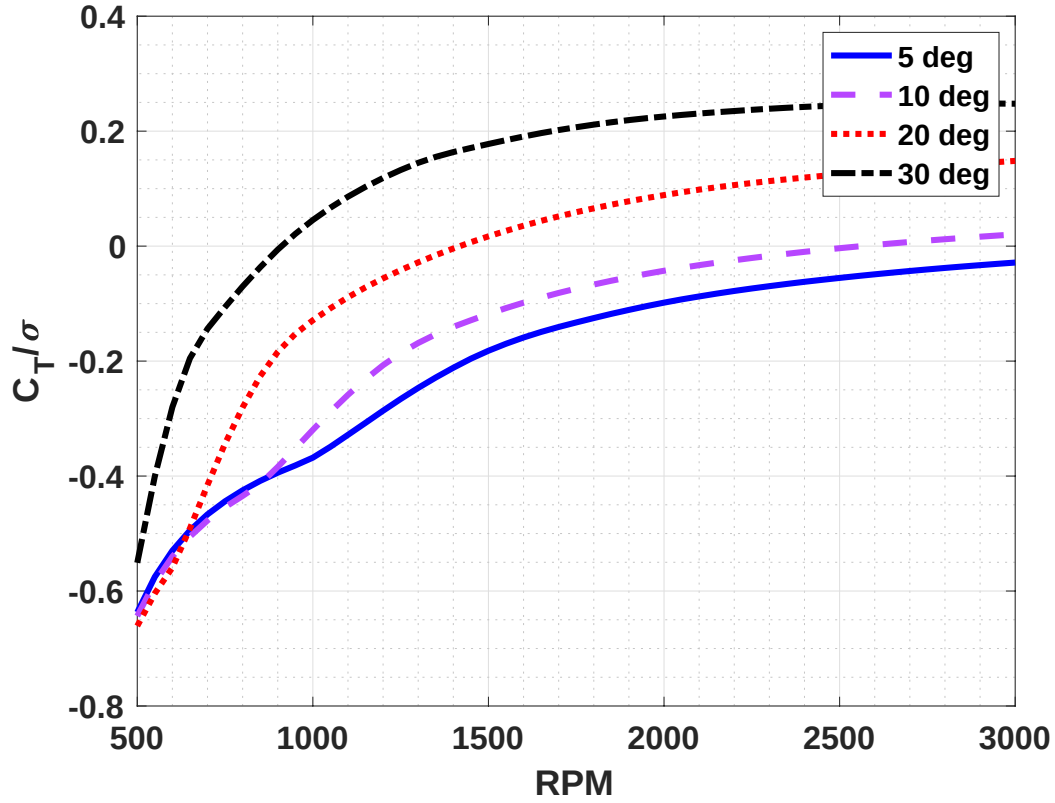

Figure 6.4: C_T/σ versus RPM

All collectives have increasing C_T/σ as RPM increases. As collectives increase, the RPM at which C_T/σ crosses zero decreases. The 5° line collective starts at negative thrust and does not cross $C_T/\sigma = 0$ at all. The 10° collective line starts at

negative thrust, crosses $C_T/\sigma = 0$ at 2600 RPM, and continues positively thereafter. Similarly, the 20° collective line starts at negative thrust, crosses $C_T/\sigma = 0$ at 1450 RPM, and continues positively thereafter. The 30° collective line starts at negative thrust, crosses $C_T/\sigma = 0$ at 900 RPM, and continues positively thereafter.

The hover inflow $\lambda_h = sign(C_T)\sqrt{\frac{|C_T|}{2}}$ is plotted versus RPM for $\theta_{75} = 5°, 10°, 20°, 30°$ in Figure 6.5. These naturally follow the same trend as C_T except for the square root. The trends are re-iterated for completeness.

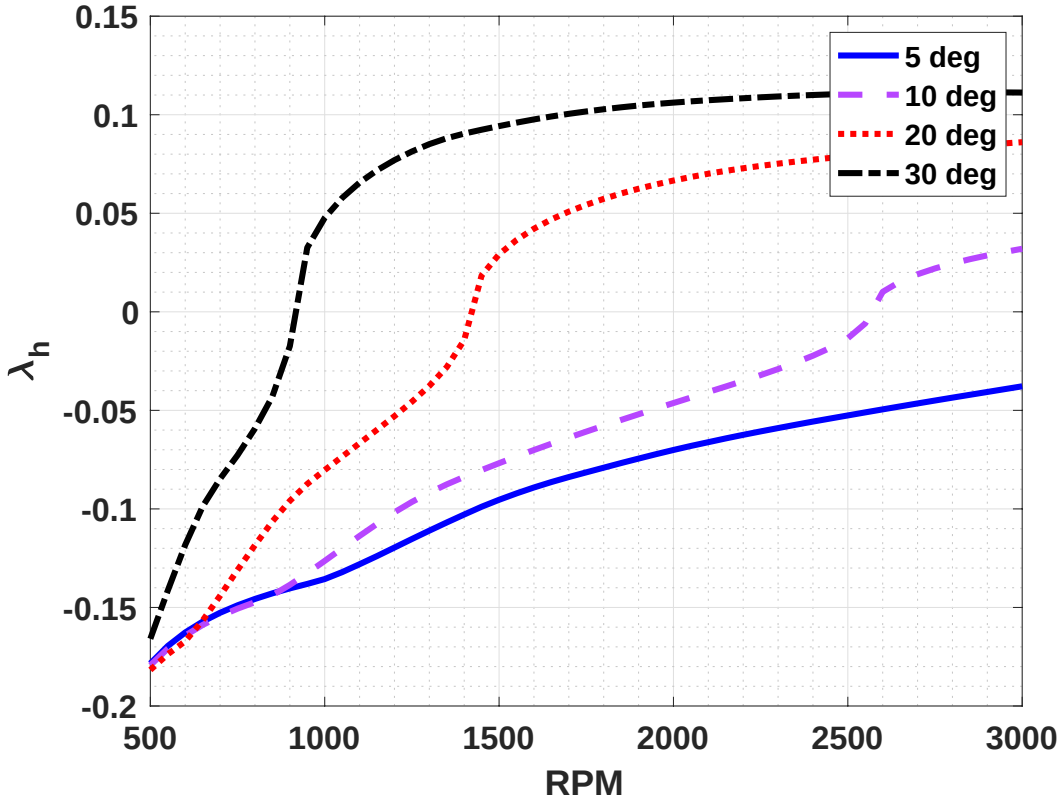

Figure 6.5: FSD λ_h versus RPM

All collectives have increasing λ_h as RPM increases. As collective increases, the rate of increasing λ_h per RPM increases as well. As collective increases, the RPM at which λ_h crosses zero decreases. The 5° collective line starts at negative

λ_h and does not cross $\lambda_h = 0$ at all. The 10° collective line starts at negative λ_h, crosses $\lambda_h = 0$ at 2600 RPM, and continues positively thereafter. The 20° collective line starts at negative λ_h, crosses $\lambda_h = 0$ at 1450 RPM, and continues positively thereafter. The 30° collective line starts at negative λ_h, crosses $\lambda_h = 0$ at 900 RPM, and continues positively thereafter.

The induced inflow λ_i is then plotted versus RPM at $\theta_{75} = 5°, 10°, 20°, 30°$ in Figure 6.6. The induced inflow is the opposite direction of thrust; thus, negative λ_i means the induced inflow moves up through the rotor disk, whereas positive λ_i means the induced inflow moves down through the rotor disk.

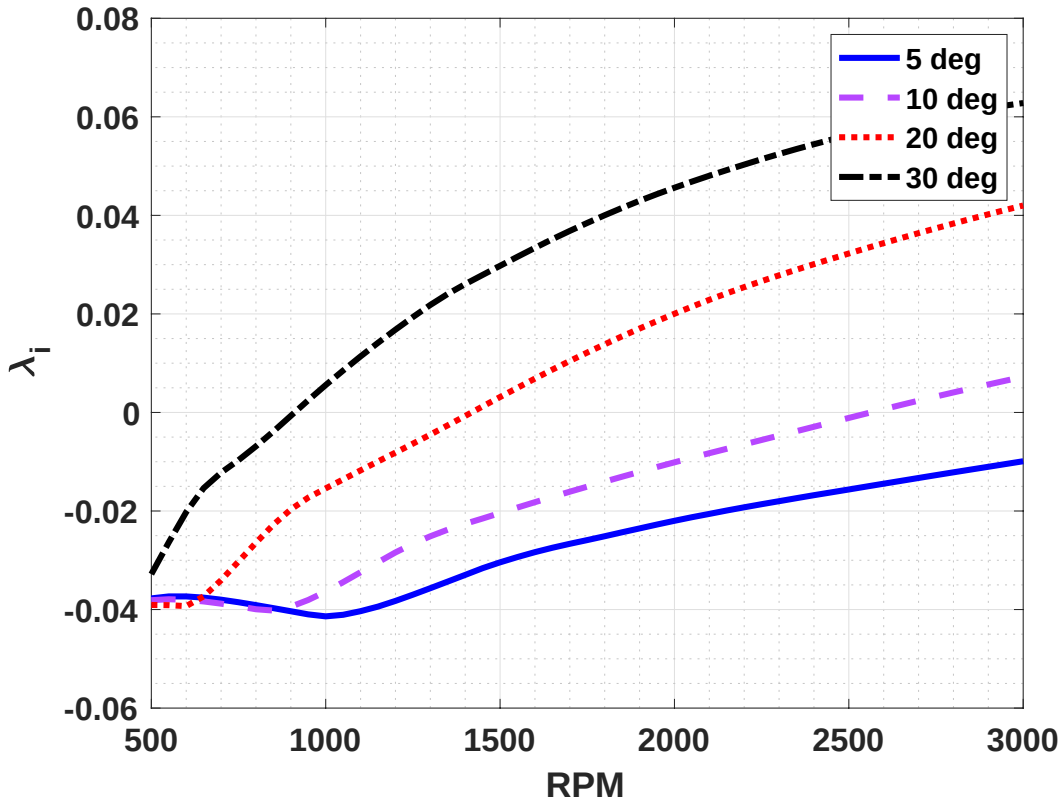

Figure 6.6: FSD λ_i versus RPM

For $\theta_{75} = 5°$ and 10°, λ_i more or less stays constant until about 1000 RPM,

where λ_i begins to increase and continues to increase as RPM increases. For $\theta_{75} = 20°$ and $30°$, λ_i always increases as RPM increases. As collective increases, the RPM at which λ_i crosses zero decreases. The $5°$ collective line starts at negative λ_i and remains negative for the entirety of the plot, though λ_i decreases until 1000 RPM where it then begins to increase but always remains negative. The $10°$ collective line starts at negative λ_i, decreases until 800 RPM where it begins to increase, crosses $\lambda_i = 0$ at 2600 RPM, and continues positively thereafter. Similarly, the $20°$ collective line starts at negative λ_i, crosses $\lambda_i = 0$ at 1400 RPM, and continues positively thereafter. The $30°$ collective line also starts at negative λ_i, crosses $\lambda_i = 0$ at 900 RPM, and continues positively thereafter. Thus, these crossover points are also consistent with C_T.

The cruise inflow λ_c is plotted versus RPM in Figure 6.7.

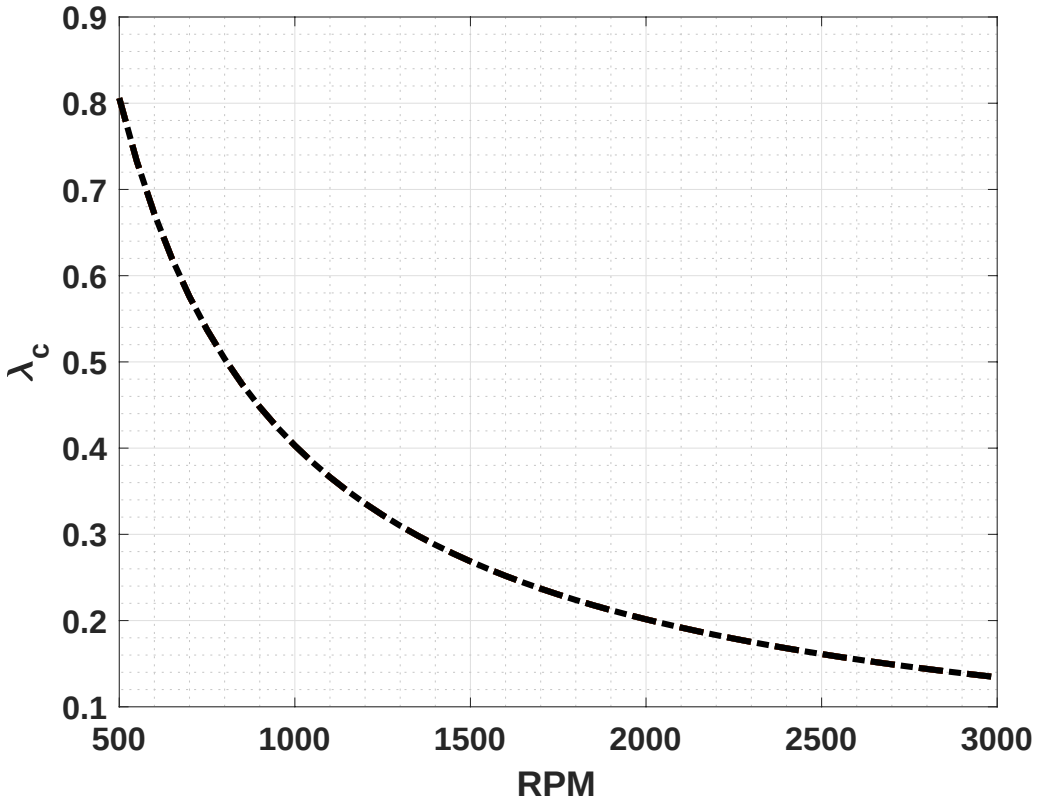

Figure 6.7: FSD λ_c versus RPM; same for all collectives

The cruise inflow is only dependent on the wind tunnel speed ($\lambda_c = \frac{v_c}{\Omega R}$), and because the tunnel speed v_c is specified, λ_c is the same for all collectives. The only variation is with RPM. The line follows a $1/RPM$ trend. As RPM increases, λ_c decreases, along with the rate at which it decreases.

The universal inflow, a plot of $\frac{\lambda_i}{\lambda_h}$ versus $\frac{\lambda_c}{\lambda_h}$, is then predicted at $\theta_{75} = 5°, 10°, 20°, 30°$ in Figure 6.8. The collectives all collapse to the same curve, which is expected— hence the name universal. First, this verifies the soundness of the analysis. Second, and more importantly, it reiterates that freewheeling is not autorotation. Autorotation occurs at $\lambda_c/\lambda_h \approx -1.7$. Freewheeling occurs where $\lambda_h \approx 0$. It occurs at $\lambda_c/\lambda_h \approx -\infty$, and at freewheeling, RPM jumps to $+\infty$. Thus, it is a very special

condition of the rotor and unique to tiltrotors.

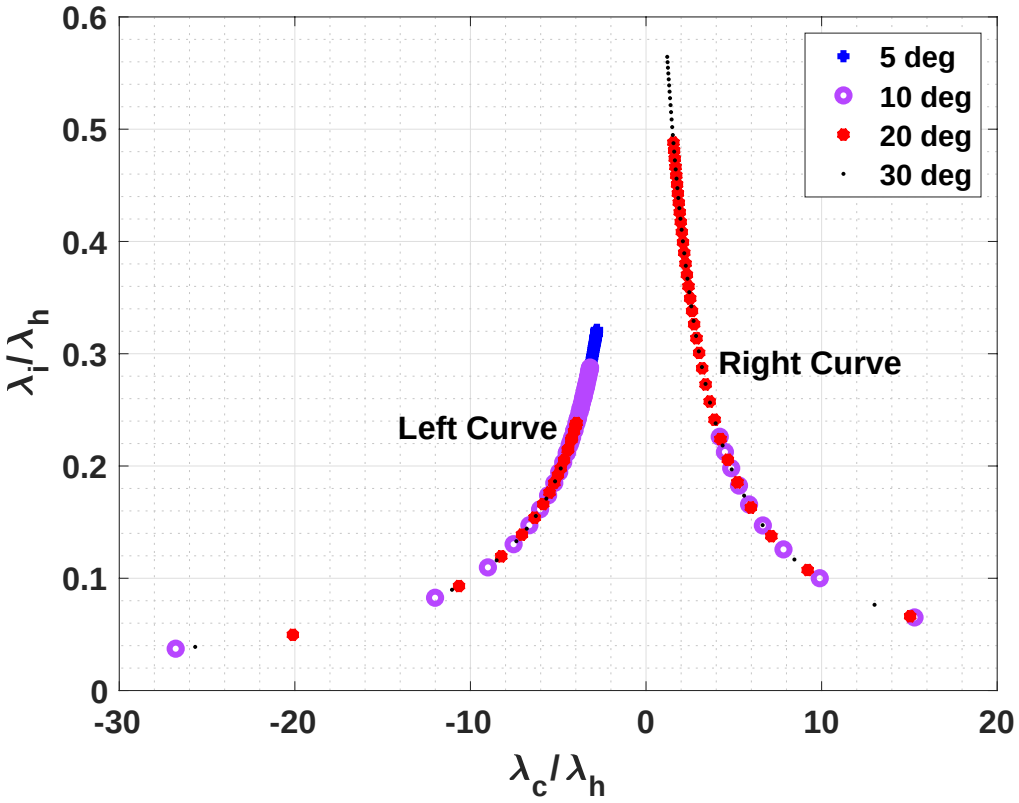

Figure 6.8: FSD λ_i/λ_h versus λ_c/λ_h

Looking back to the individual plots of the variables, λ_i starts negative, λ_h starts negative, and λ_c is always positive but decreasing as RPM increases. All collectives collapse on the left and right curves of the universal inflow plot (Figure 6.8). At 500 RPM, the inflow values begin at at the top of the left curve. As λ_i and λ_h increase, becoming less negative as RPM increases, they move along the curve to increasingly negative λ_c/λ_h since λ_h is in the denominator. As λ_i and λ_h increase as RPM increases, while λ_c decreases, the curve moves to less positive λ_i/λ_h since λ_h has a greater magnitude than λ_i. As λ_h approaches zero, the curve flattens out because λ_c/λ_h decreases much faster than λ_i/λ_h since λ_i is also approaching zero.

Once λ_h crosses zero, the solutions jump from the lower left to the lower right since the denominator cannot be zero in both λ_c/λ_h and λ_i/λ_h. λ_i crosses zero almost at the same RPM as λ_h, with small differences, so the ratio λ_i/λ_h remains positive and defined. As λ_i and λ_h increase positively as RPM increases and λ_c still decreases, the values then move along the curve from bottom right up to top right. The 5° collective has the highest λ_i/λ_h because at 5°, λ_i starts the most negative and λ_h starts at a comparable value for all collectives. The 30° ends at the highest λ_i/λ_h on the right curve because at 30°, λ_i is the highest at the end of the RPM range than for the other collectives. Thus the collective points are offset from each other even though they fall on the same universal curve.

6.4 Trim Solution Results

First, the predictions for 25 knots are plotted along with the experimental data across a sweep of $\theta_{75} = 0° - 60°$ (Figure 6.9). The CFD VR-7 airfoil deck is used for baseline results.

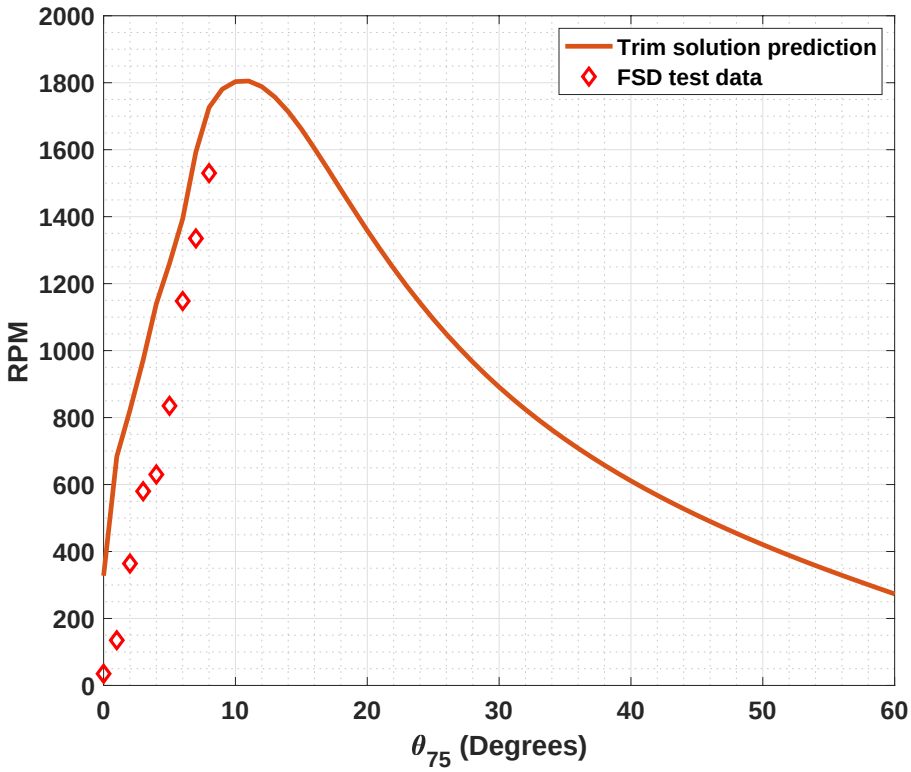

Figure 6.9: FSD 25 knots freewheeling trim solution and experimental results

As observed earlier in the C_Q/σ plot (Figure 6.3), the RPM for $C_Q/\sigma = 0$ increases from $0° - 10°$, where it hits a peak, then decreases from $10° - 60°$. The test data is correct but only covers the left side of the curve. After careful examination of the data and the analysis, it was determined that the right side of the curve is where test data should be collected because the higher collectives are proper representatives of a tiltrotor in high-speed cruise. However, the left side of the curve provides excellent candidates for analysis validation. This is because it is very sensitive to airfoil properties beyond stall, especially on the negative angle of attack side.

To compare the CFD aifoil deck to the Ames airfoil deck, the trim solution

process was repeated but now with the Ames airfoil deck (Figure 6.10).

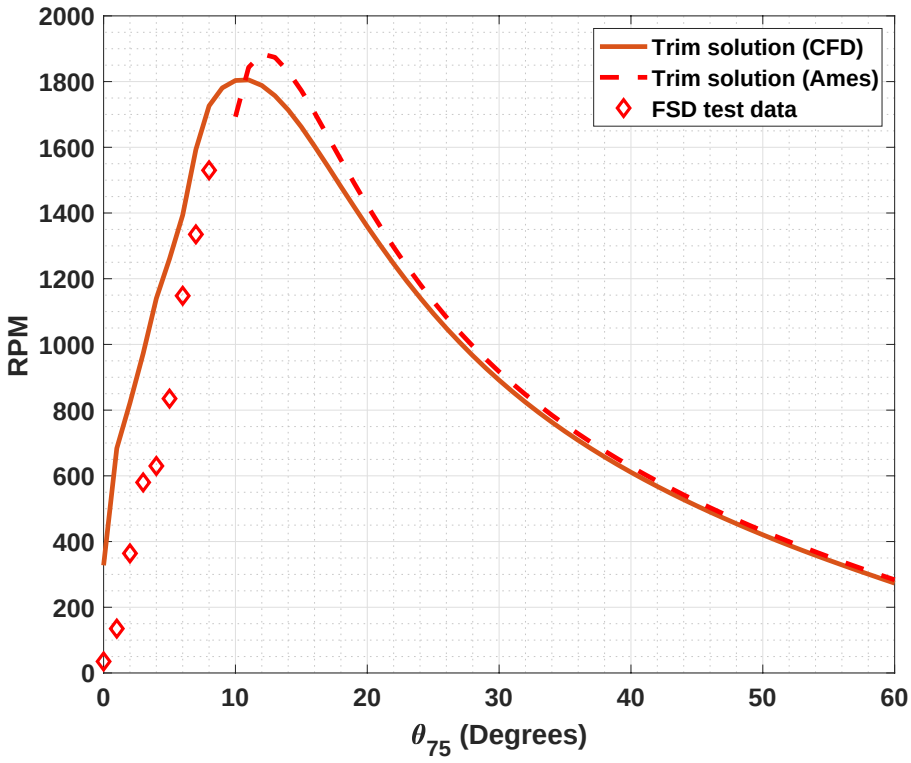

Figure 6.10: FSD 25 knots freewheeling trim solution and experimental results; CFD and Ames airfoil decks

Though the trend is similar at $10° - 60°$, the solution does not even converge at $\theta_{75} < 10°$. In addition, the peak is shifted about $+4°$ to the right and occurs at +100 RPM. It is clear that the Ames deck does not represent the negative stall region correctly.

To prove the importance of airfoil stall, the trim solution process is repeated but now using only linear aerodynamics.

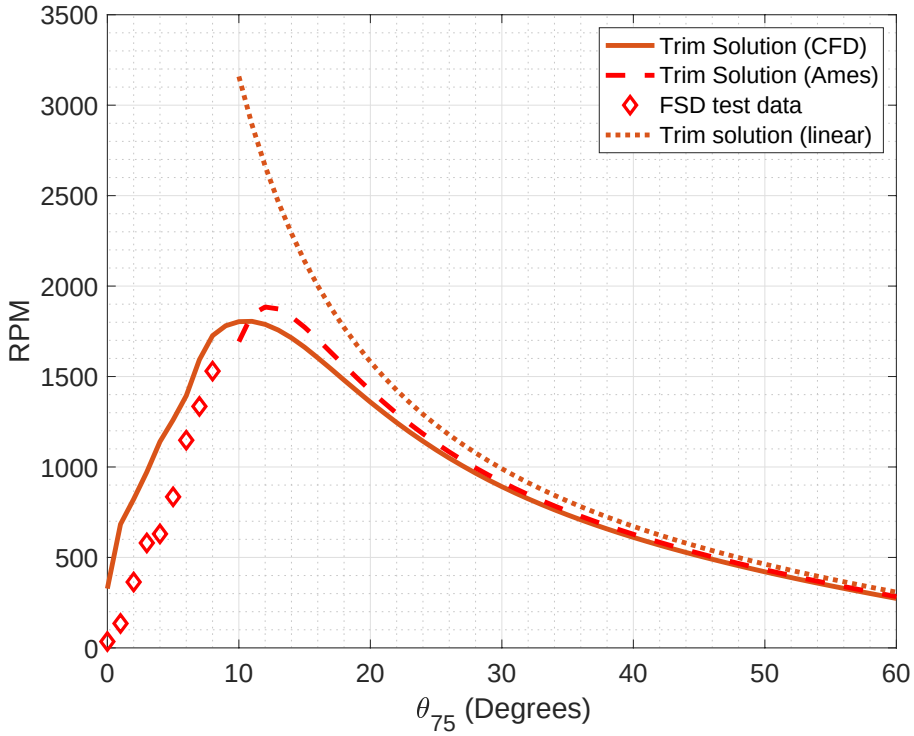

Figure 6.11: FSD 25 knots freewheeling trim solution and experimental results; CFD and Ames airfoil decks and linear aerodynamics

The linear aerodynamics do not predict the left side of the curve at all, so without the airfoil tables, the predicted results would not follow the measured trend at all. The airfoil stall properties create the peak which gives two collectives for a given RPM where $C_Q/\sigma = 0$. These results also show that for high-speed cruise, however, the linear aerodynamics will suffice.

Next, the trim solutions for 12 knots, 25 knots, and 32 knots, are shown together in Figure 6.12. The collectives are swept from $0 - 60°$ for all wind speeds as before. The VR-7 CFD airfoil deck, now established as the correct deck, is used. The symbols represent the same experimental data as Figure 6.2 earlier, and the lines are the predictions.

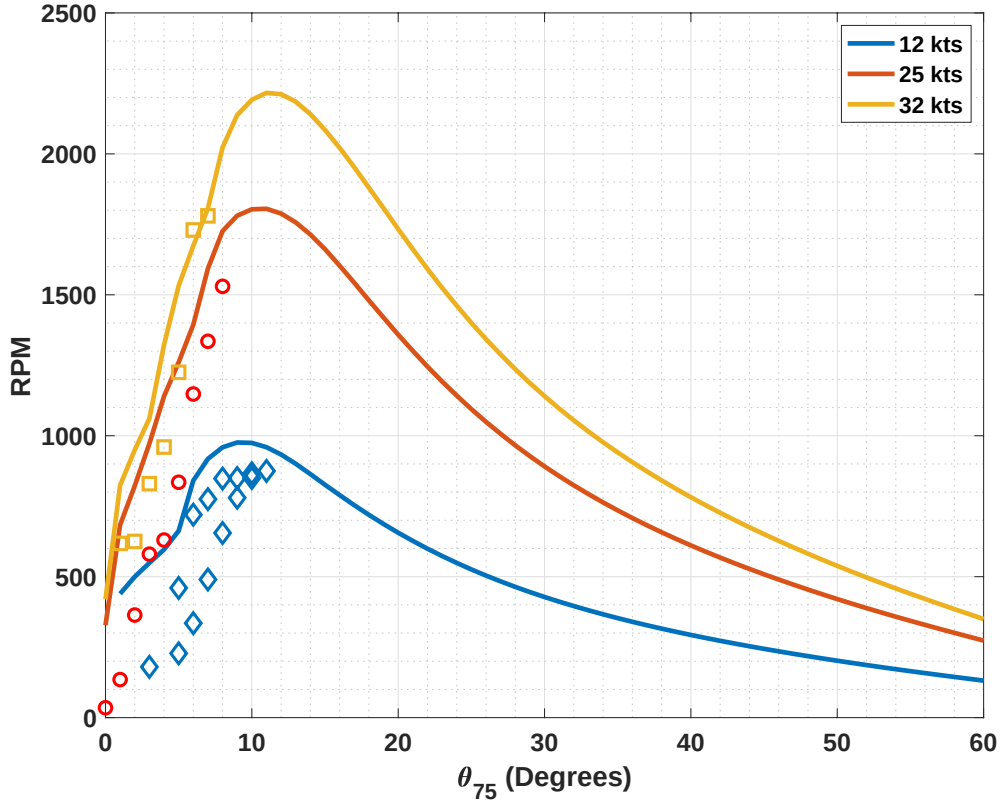

Figure 6.12: FSD freewheeling trim solution and experimental results (12, 25, and 30 kts); CFD airfoil deck

For all tunnel speeds, as collective increases, the predicted values become closer to the experimental data. As tunnel speed increases, the RPM at which the peak occurs also increases and so does the collective, though this change is small. The 12 knot prediction line begins at 500 RPM at 0° collective, increases until 9° where it peaks at 900 RPM, and then decreases until 60° where ends at 100 RPM. The 25 knot tunnel speed prediction line begins at 500 RPM at 0°, increases until 10° where it peaks at 1800 RPM, and then decreases until 60° where ends at 250 RPM. The 32 knot tunnel speed prediction line begins at 500 RPM at 0°, increases until 12° where it peaks at 2200 RPM, and then decreases until 60° where ends at 350

RPM.

The same trim solution is now predicted using the VR-7 Ames deck, shown as the dashed lines in Figure 6.13.

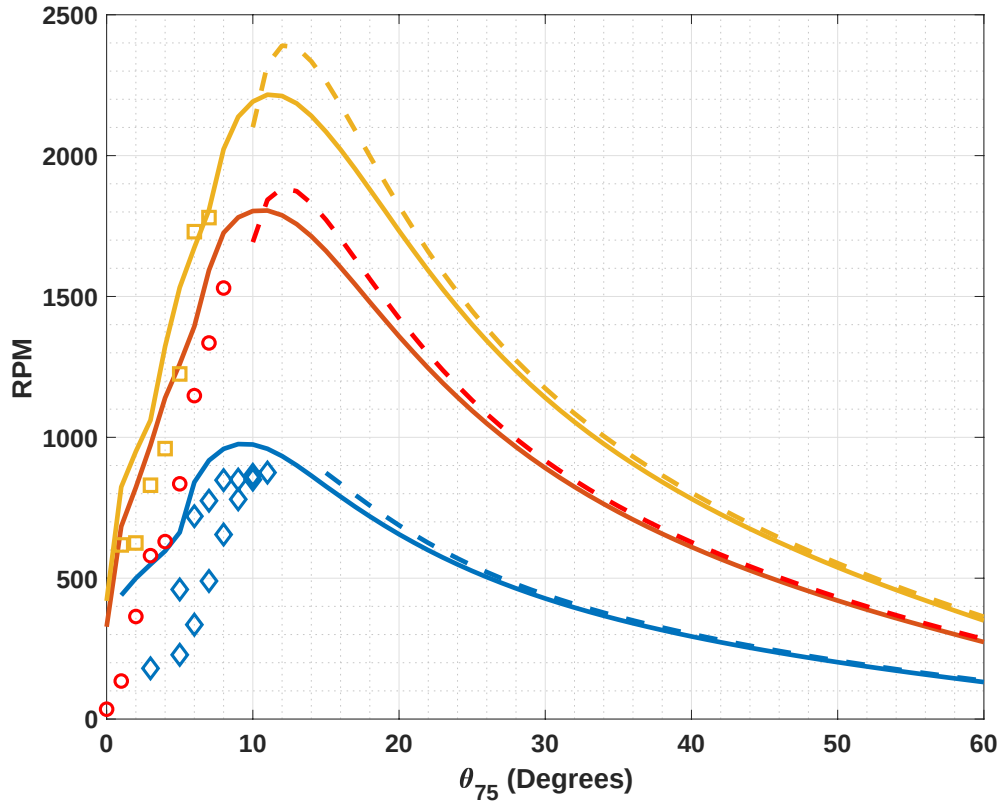

Figure 6.13: FSD freewheeling trim solution and experimental results; CFD and Ames airfoil decks

The Ames airfoil deck solution for 12 knots does not converge below $\theta_{75} = 15°$. As in the 25 knots results, the solution for 32 knots does not converge below $\theta_{75} = 10°$. The peak of the curves are also shifted to a higher collective and higher RPM than the solutions using the CFD deck. Thus, the CFD airfoil deck is determined to be likely more accurate than the Ames airfoil deck.

For completeness, the linear aerodynamic solutions for all speeds are shown as

the dotted lines in Figure 6.14.

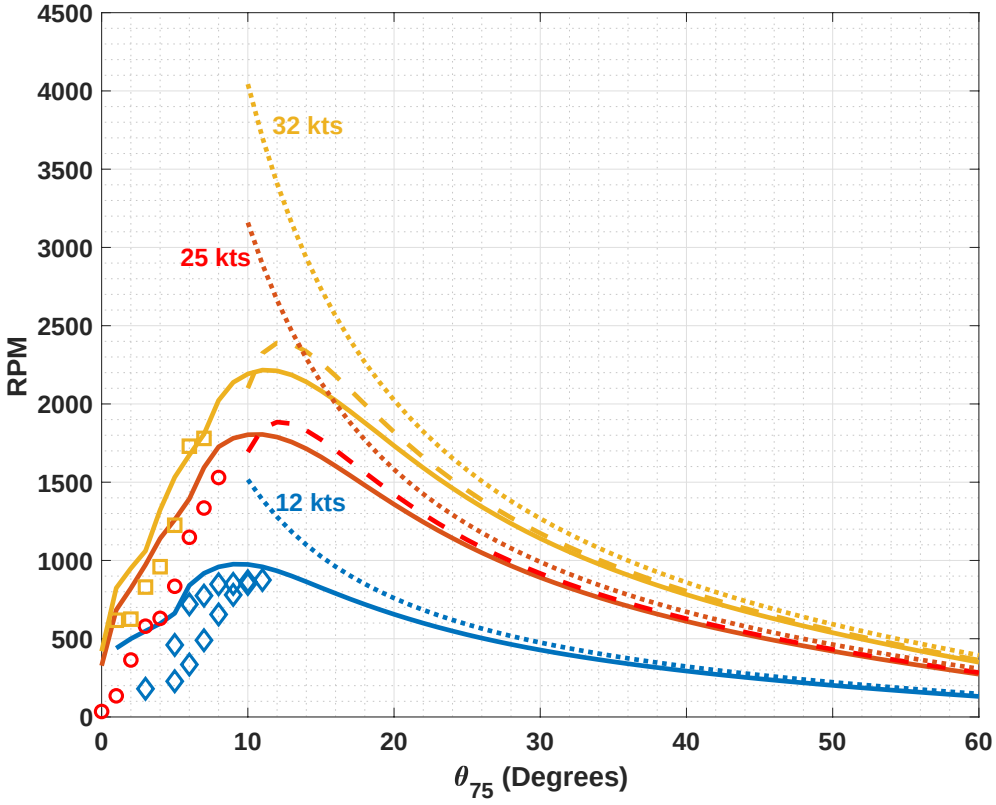

Figure 6.14: FSD freewheeling trim solution and experimental results (12, 25, and 30 kts); CFD and Ames airfoil decks and linear aerodynamics

As in the 25 knots results, the results do not converge below $\theta_{75} = 10°$ for any of the tunnel speeds. The linear data does not predict a peak at all as before because it has no stall. Thus, in summary, airfoil tables are necessary for predicting the correct results at lower collectives, and the CFD deck is likely more accurate than the Ames deck available in public.

Chapter 7: MTR Results

This chapter discusses the analytical and experimental results of the Maryland tiltrotor rig (MTR), which can be seen in the Glenn L. Martin Wind Tunnel in Figure 7.1.

(a) MTR with blades integrated

(b) The author with the MTR rig

Figure 7.1: The Maryland tiltrotor rig (MTR) installed in the Glenn L. Martin Wind Tunnel, September 2019

7.1 Experimental Data

The data collected from the MTR freewheeling test in the Glenn L. Martin Wind Tunnel is listed in Table 7.1 and plotted in Figure 7.2.

	$v_c = 25$ kts	$v_c = 35$ kts	$v_c = 40$ kts
θ_{75} (deg)		Ω (RPM)	
0		250	590
1		453	780
2		647	
3		696	960
4	400	820	1130
5		1127	1461
6	591	1220	1525
7		1222	1235
8	780		1524

Table 7.1: Freewheeling RPM for the MTR at various wind speeds and collectives

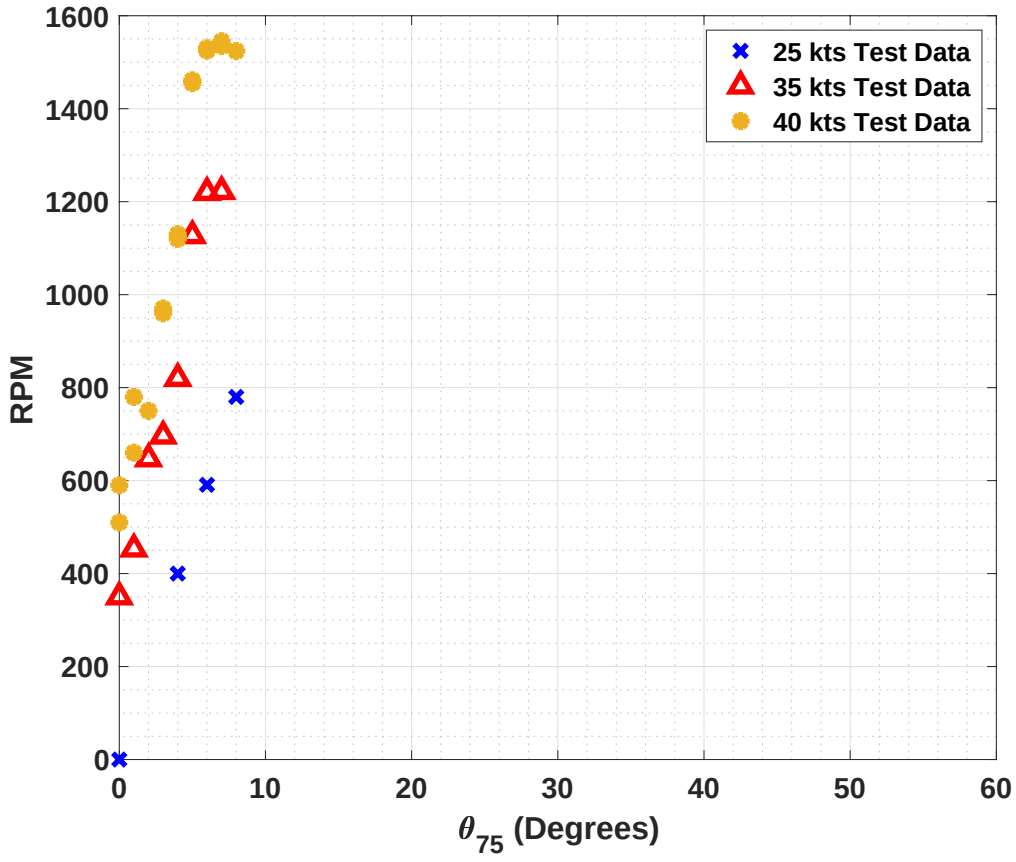

Figure 7.2: MTR freewheeling RPM data for tunnel speeds of 25 kts, 35 kts, and 40 kts

As the collective increases, the RPM increases for all wind speeds. As the wind speed increases, the RPM for a given collective also increases.

7.2 Model Inputs

The Maryland Tiltrotor Rig (MTR) was modeled to compare against the experimental data. The model parameters are shown in Table 7.2. EI_N is the blade normal stiffness, N_b is number of blades, R is the rotor radius, x_c is the non-dimensional root cutout, σ is blade solidity, ρ is air density, m is the spanwise mass

of the blades, θ_t is the spanwise twist, and c is the chord measurement.

Parameters	**Value**
EI_N (Nm^2)	20.1
N_b	3
R (m)	0.723
x_c	0.263
σ	0.1
ρ (kg/m^3)	1.225
m (kg/m)	0.3
θ_t $(^\circ/span)$	-37
c (m)	0.1029
Hub Type	Gimbaled
Airfoil	VR-7

Table 7.2: Model inputs for the Maryland Tiltrotor Rig (MTR)

The MTR was analyzed with aerodynamics and blade flexibility in flapping. All mass and stiffness measurements are available.

7.3 Model Results

First, all predictions are calculated at a tunnel speed of 25 knots. For a specified collective θ_{75}, the RPM is swept from 500-3000. At each condition, the inflow is iterated to converge the thrust C_T. The predicted torque C_Q/σ for $\theta_{75} = 5^\circ, 10^\circ, 20^\circ, 30^\circ$ versus RPM can be seen in Figure 7.3.

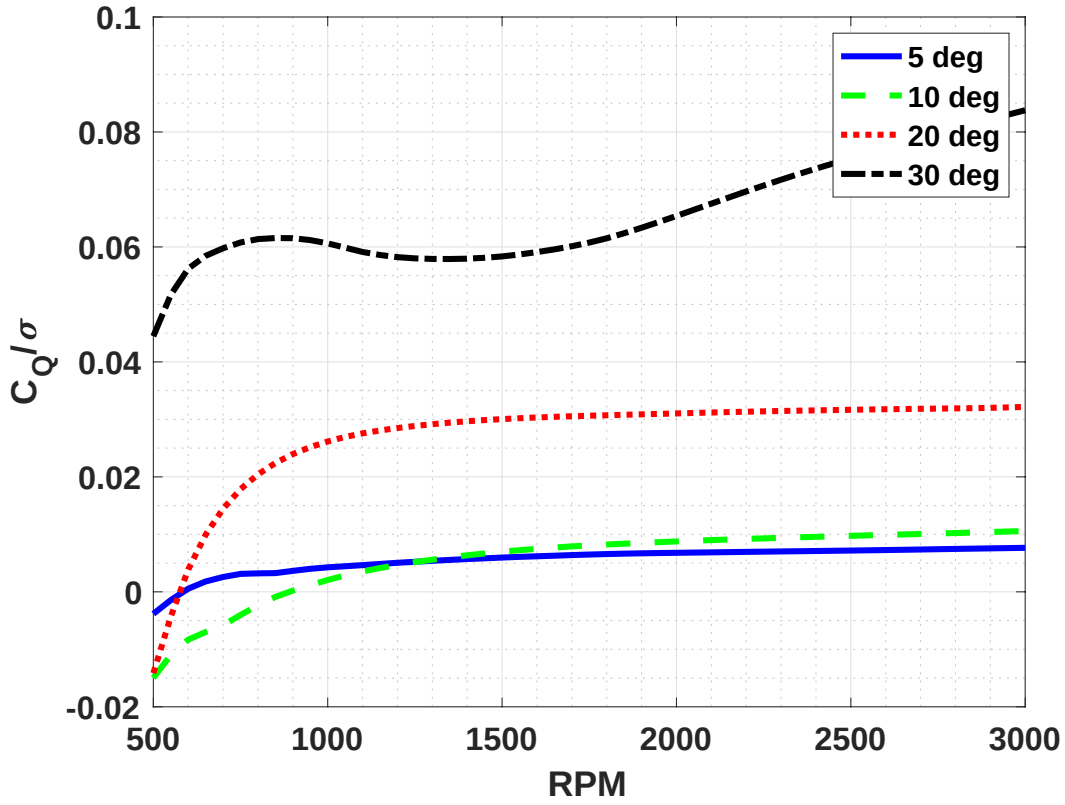

Figure 7.3: MTR C_Q/σ versus RPM

For collectives of $\theta_{75} = 5°, 10°, 20°$, as RPM increases, C_Q/σ also increases. As collective increases, the RPM at which C_Q/σ crosses zero first increases from the collective 5° until 10°, but then decreases as collective increases. The 5° collective line starts at negative torque, crosses $C_Q/\sigma = 0$ at 600 RPM, and continues positively thereafter. The 10° collective line starts at negative torque, crosses $C_Q/\sigma = 0$ at 900 RPM, and continues positively thereafter. Similarly, the 20° collective line starts at negative torque, crosses $C_Q/\sigma = 0$ at 600 RPM, and continues positively thereafter. The 30° collective line starts at positive torque, increases until 800 RPM, where it decreases until 1400 RPM, and continues increasing thereafter. It does not cross $C_Q/\sigma = 0$ at all on the plot, but projecting the trend, it would cross before

500 RPM.

The corresponding C_T/σ is plotted versus RPM for $\theta_{75} = 5°, 10°, 20°, 30°$ in Figure 7.4.

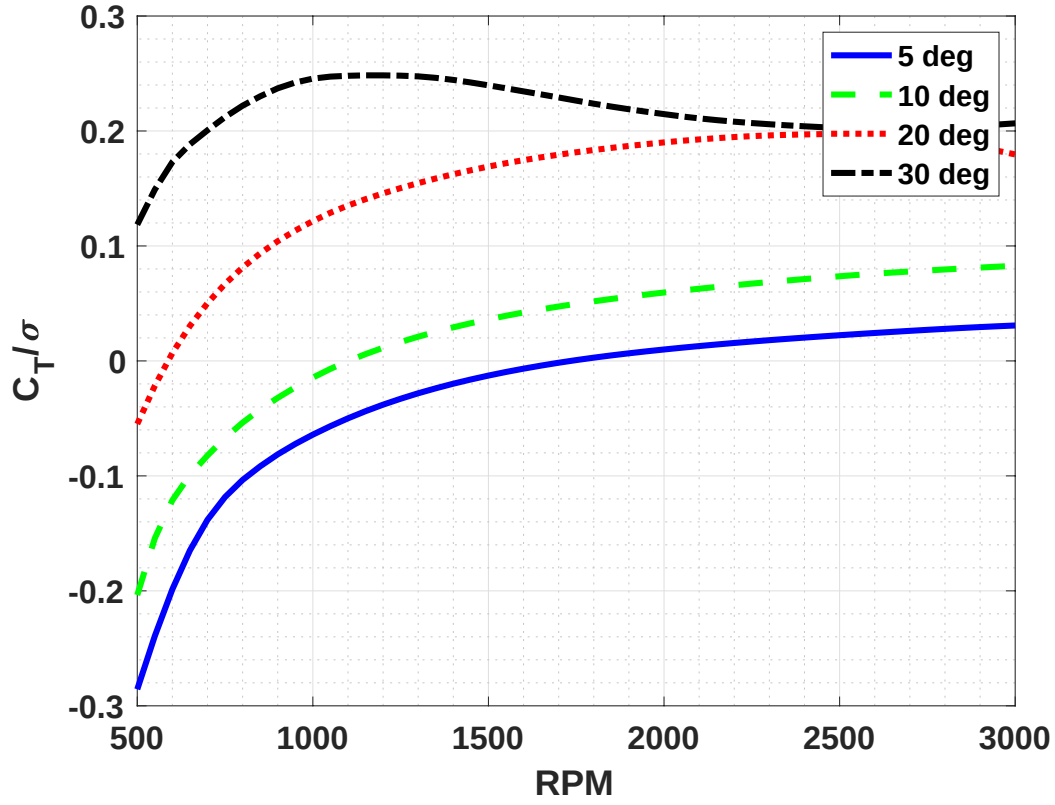

Figure 7.4: MTR C_T/σ versus RPM

For the collectives of $\theta_{75} = 5°, 10°, 20°$, as RPM increases, C_T/σ also increases. As collective increases, the RPM at which $C_T/\sigma = 0$ decreases. The 5° collective line starts at negative thrust, crosses $C_T/\sigma = 0$ at 1700 RPM, and continues positively thereafter. The 10° collective line starts at negative thrust, crosses $C_T/\sigma = 0$ at 1100 RPM, and continues positively thereafter. Similarly, the 20° collective line starts at negative thrust, crosses $C_T/\sigma = 0$ at 600 RPM, and continues positively thereafter. The 30° collective line starts at positive thrust, increases until 1100 RPM where it

decreases thereafter, though staying positive. It does not cross $C_T/\sigma = 0$ at all on the plot, but projecting the trend, it would cross before 500 RPM.

The hover inflow $\lambda_h = sign(C_T)\sqrt{\frac{|C_T|}{2}}$ is plotted versus RPM for $\theta_{75} = 5°, 10°, 20°, 30°$ in Figure 7.5. These naturally follow the same trend as C_T except for the square root. The trends are re-iterated for completeness.

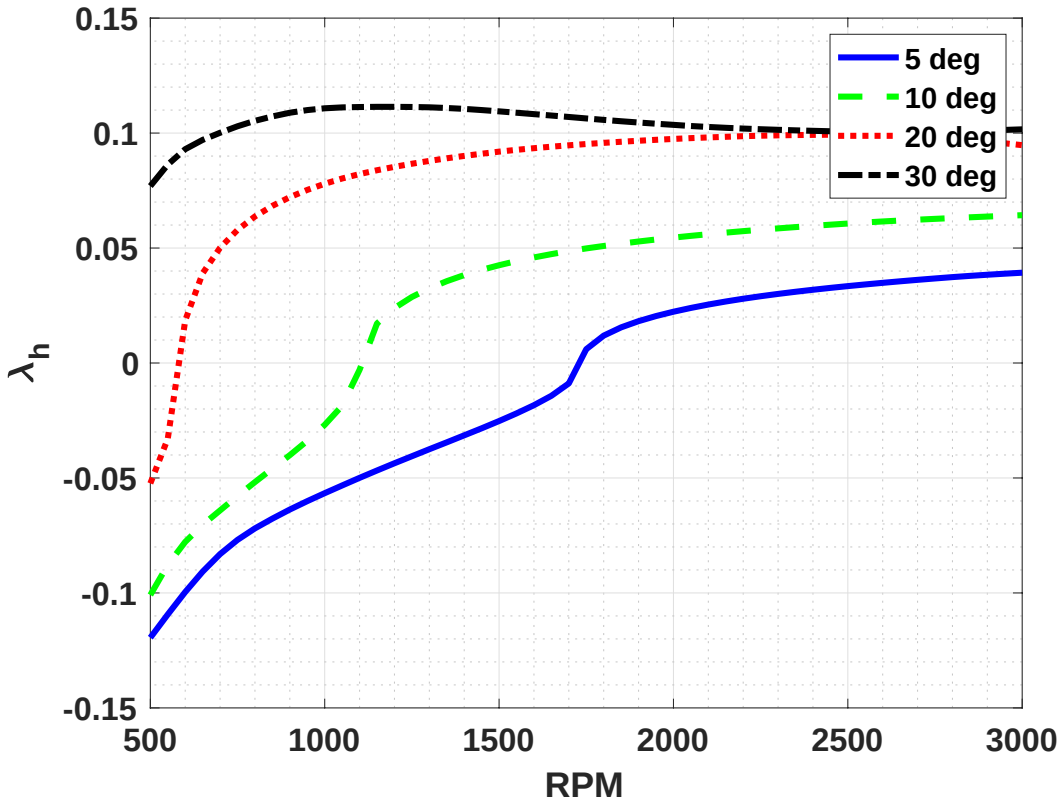

Figure 7.5: MTR λ_h versus RPM

Like C_T/σ, for collectives of $\theta_{75} = 5°, 10°, 20°$, λ_h increases as RPM increases. As collective increases, the RPM at which λ_h crosses zero decreases. The 5° collective line starts at negative λ_h, crosses $\lambda_h = 0$ at 1700 RPM, and continues positively thereafter. The 10° collective line starts at negative λ_h, crosses $\lambda_h = 0$ at 1100 RPM, and continues positively thereafter. The 20° collective line starts at negative λ_h,

crosses $\lambda_h = 0$ at 600 RPM, and continues positively thereafter. The 30° collective line starts at positive λ_h, increases until 1100 RPM where it decreases slowly after, though staying positive. It does not cross $\lambda_h = 0$ at all on the plot, but projecting the trend, it would cross before 500 RPM.

The induced inflow λ_i is then plotted versus RPM at $\theta_{75} = 5°, 10°, 20°, 30°$ in Figure 7.6. The induced inflow is the opposite direction of thrust; thus, negative λ_i means the induced inflow moves up through the rotor disk, whereas positive λ_i means the induced inflow moves down through the rotor disk.

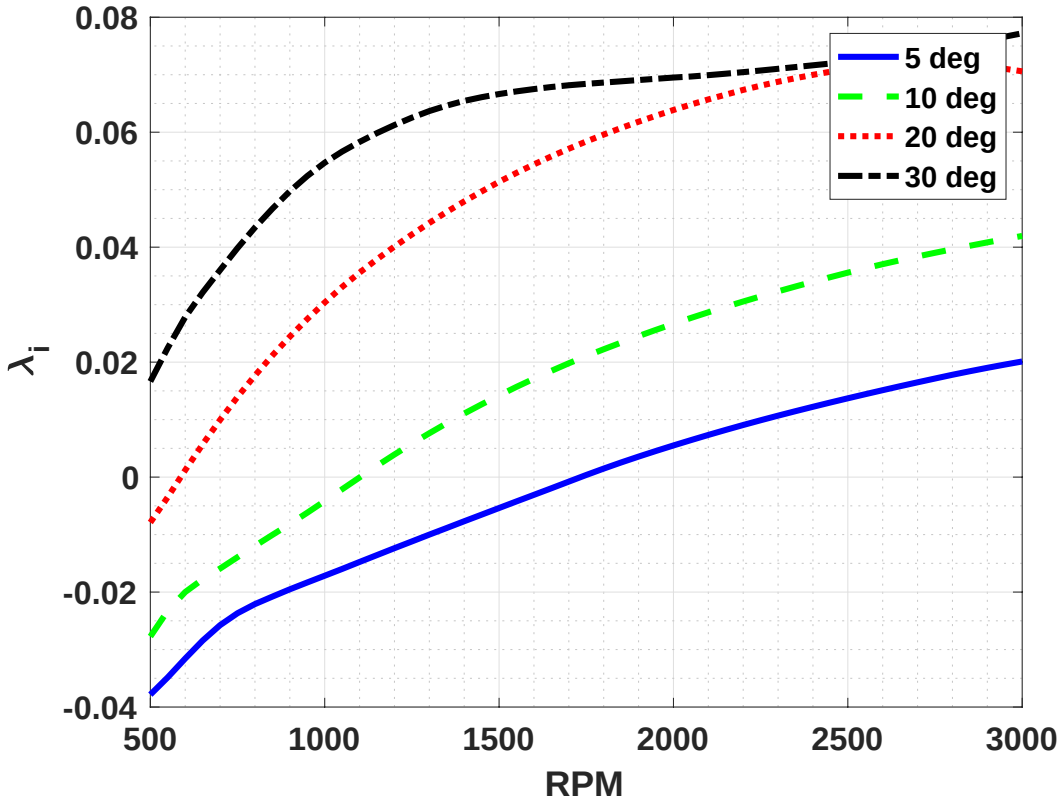

Figure 7.6: MTR λ_i versus RPM

For all collectives, λ_i always increases as RPM increases. As collective increases, the RPM at which λ_i crosses zero decreases. As collective increases, the λ_i

at for each RPM also increases. The 5° collective line starts at negative λ_i, crosses $\lambda_i = 0$ at 1700 RPM, and continues positively thereafter. The 10° collective line begins at negative λ_i, crosses $\lambda_i = 0$ at 1100 RPM, and continues positively thereafter. Similarly, the 20° collective line starts at negative λ_i, crosses $\lambda_i = 0$ at 600 RPM, and continues positively thereafter. The 30° collective line starts at positive λ_i and increases as RPM increases. It does not cross $\lambda_i = 0$ at all on the plot, but projecting the trend, it would cross before 500 RPM.

The cruise inflow λ_c versus RPM in Figure 7.7.

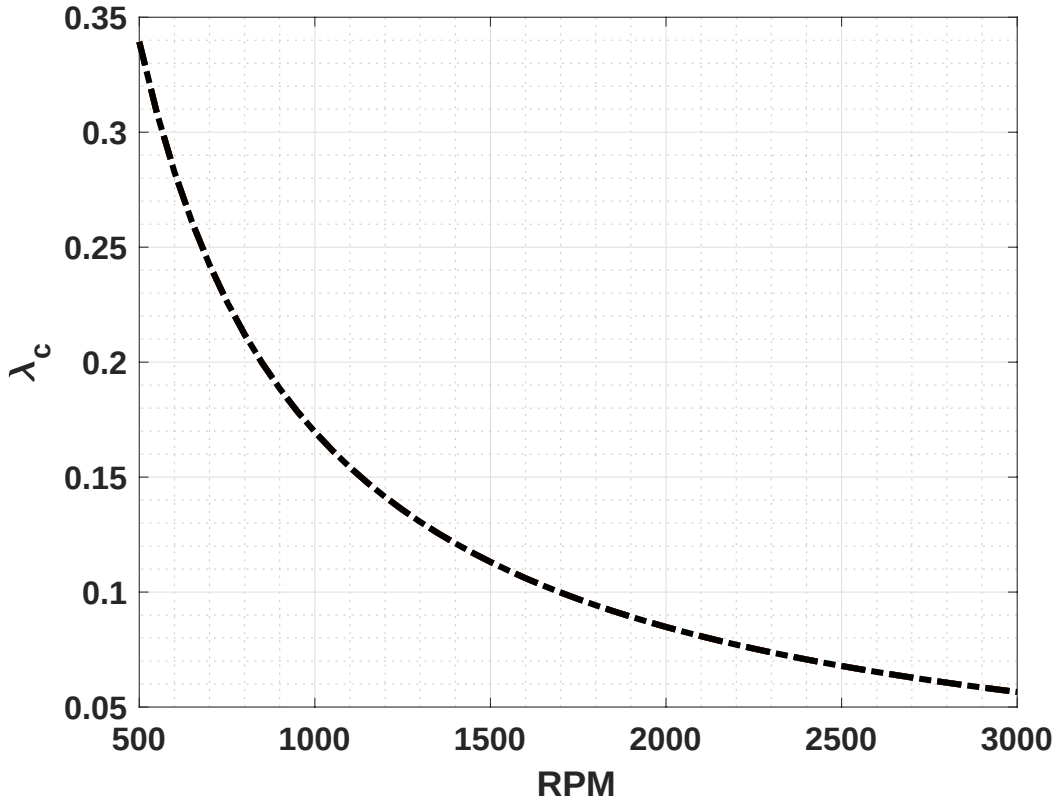

Figure 7.7: MTR λ_c versus RPM; same for all collectives

The cruise inflow is only dependent on the wind tunnel speed ($\lambda_c = \frac{v_c}{\Omega R}$), and because the tunnel speed v_c is specified, λ_c is the same for all collectives. The only

variation is with RPM. The line follows a $1/RPM$ trend. As RPM increases, λ_c decreases, along with the rate at which it decreases.

The universal inflow, a plot of $\frac{\lambda_i}{\lambda_h}$ versus $\frac{\lambda_c}{\lambda_h}$, is then predicted at $\theta_{75} = 5°, 10°, 20°, 30°$ in Figure 7.8. The collectives all collapse to the same curve, which is expected— hence the name universal. First, this verifies the soundness of the analysis. Second, and more importantly, it reiterates that freewheeling is not autorotation. Autorotation occurs at $\lambda_c/\lambda_h \approx -1.7$. Freewheeling occurs where $\lambda_h \approx 0$. It occurs at $\lambda_c/\lambda_h \approx -\infty$, and at freewheeling, RPM jumps to $+\infty$. Thus, it is a very special condition of the rotor and unique to tiltrotors.

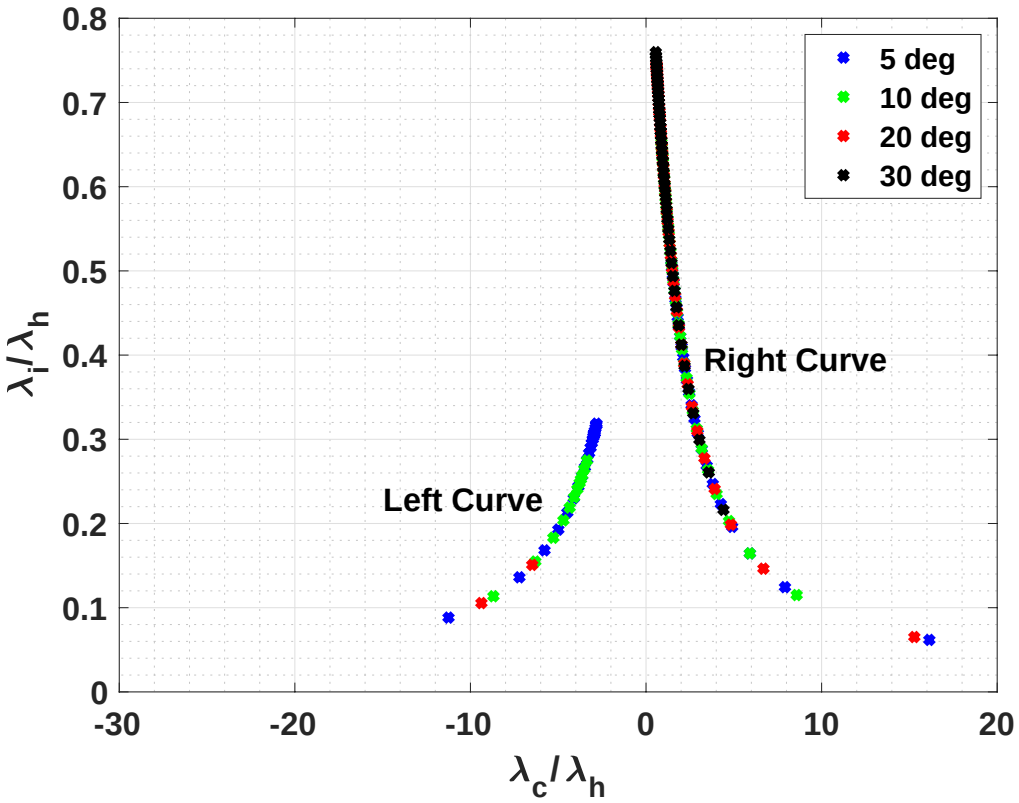

Figure 7.8: MTR $\frac{\lambda_i}{\lambda_h}$ versus $\frac{\lambda_c}{\lambda_h}$

Looking back to the individual plots of the variables, for collectives of $\theta_{75} =$

$5°, 10°, 20°$, λ_i starts negative, λ_h starts negative, and λ_c is always positive but decreasing as RPM increases. For a collective of 30°, all three variables are positive throughout. All collectives collapse on the left and right curves of the universal inflow plot (Figure 7.8). At 500 RPM, at collectives of $\theta_{75} = 5°, 10°, 20°$, the inflow values begin at the top of the left curve, since λ_i/λ_h is positive and λ_c/λ_h is negative. As λ_i and λ_h increase, becoming less negative as RPM increases, they move along the curve to increasingly negative λ_c/λ_h since λ_h is in the denominator. As λ_i and λ_h increase as RPM increases, and λ_c decreases, the curve moves to less positive λ_i/λ_h since λ_h has a greater magnitude than λ_i. As λ_h approaches zero, the curve flattens out because λ_c/λ_h decreases much faster than λ_i/λ_h since λ_i is also approaching zero. Once λ_h crosses zero, the solutions jump from the lower left to the lower right since the denominator cannot be zero in both λ_c/λ_h and λ_i/λ_h. λ_i crosses zero almost at the same RPM as λ_h with a small difference, so the ratio λ_i/λ_h remains positive and defined. As λ_i and λ_h increase positively as RPM increases and λ_c still decreases, the values now move up along the curve from bottom right up to top right.

For a collective of 30°, the data points will only be in the positive quadrant since all variables are positive. At 500 RPM, λ_c is at its highest point, λ_i is at its lowest point, and λ_h fluctuates as RPM changes. This starts the data points at the bottom right of the right curve. As RPM increases, λ_c decreases and λ_i increases, so it follows the curve from bottom right up to top right.

The 5° collective has the highest λ_i/λ_h starting point on the left curve because at 5°, λ_i starts the most negative, and though λ_h also starts the most negative, the

5° λ_i/λ_h has a higher magnitude than other collectives. The 30° ends at the highest λ_i/λ_h on the right curve because at 30°, λ_i is the largest at 3000 RPM.

7.4 Trim Solution Results

First, the predictions for 25 knots, using rigid blade aerodynamics only, are plotted along with the experimental data for 25 knots across a sweep of $\theta_{75} = 0° - 60°$ (Figure 7.9). The CFD VR-7 airfoil deck is used for baseline results.

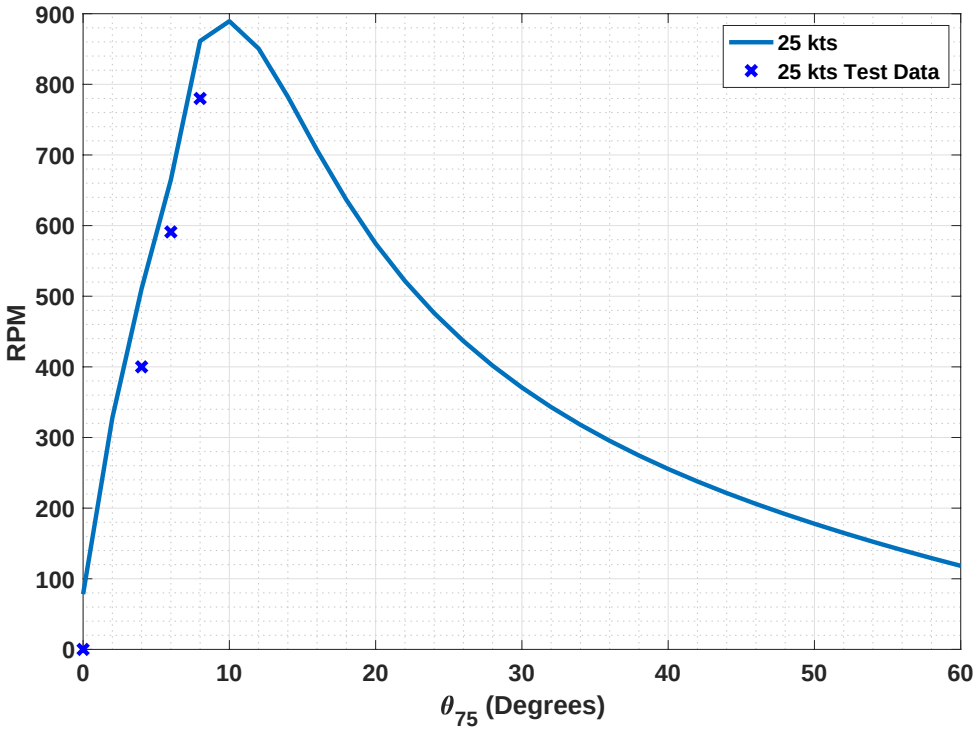

Figure 7.9: MTR freewheeling at 25 kts; prediction versus test

As observed earlier in the C_Q/σ plot (Figure 7.3), the RPM for $C_Q/\sigma = 0$ increases from $0° - 10°$, where it hits a peak, then decreases from $10° - 60°$. The test data is correct, but only covers the left side of the curve. The prediction line follows the trend of the test data with a slightly higher RPM offset. As in the FSD

(Figure 6.9), it was determined that the right side of the curve is where test data should be collected because the higher collective values are proper representatives of a tiltrotor in high-speed cruise.

To compare the CFD airfoil deck to the Ames airfoil deck, the trim solution process was repeated with the Ames airfoil deck (Figure 7.10).

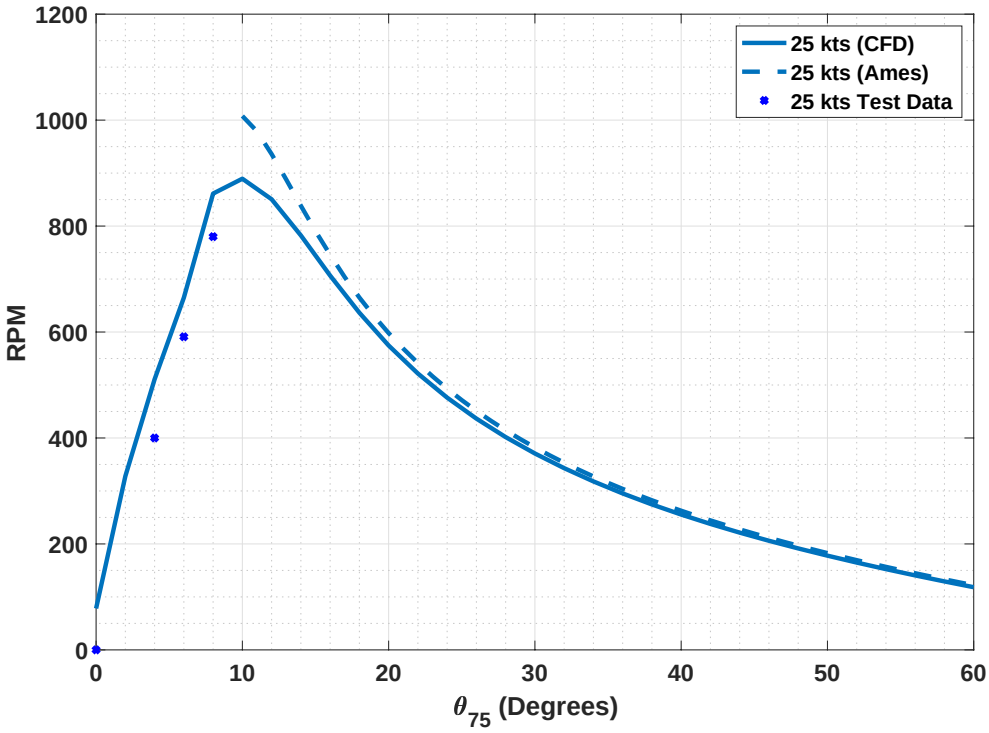

Figure 7.10: MTR freewheeling at 25 kts; prediction versus test; CFD and Ames airfoil decks

Though the trend is similar at $10° - 60°$, the solution does not even converge at $\theta_{75} < 10°$. The beginning of the prediction at $10°$ looks as if it is curving, but does not fully form the peak. It is clear that the Ames deck does not represent the negative stall region correctly.

Next, flap code is used to model a flexible flapping blade. The CFD VR-7

airfoil deck again is used. This trim solution prediction, shown as a dotted line, is compared to only rigid blade aerodynamics in Figure 7.11.

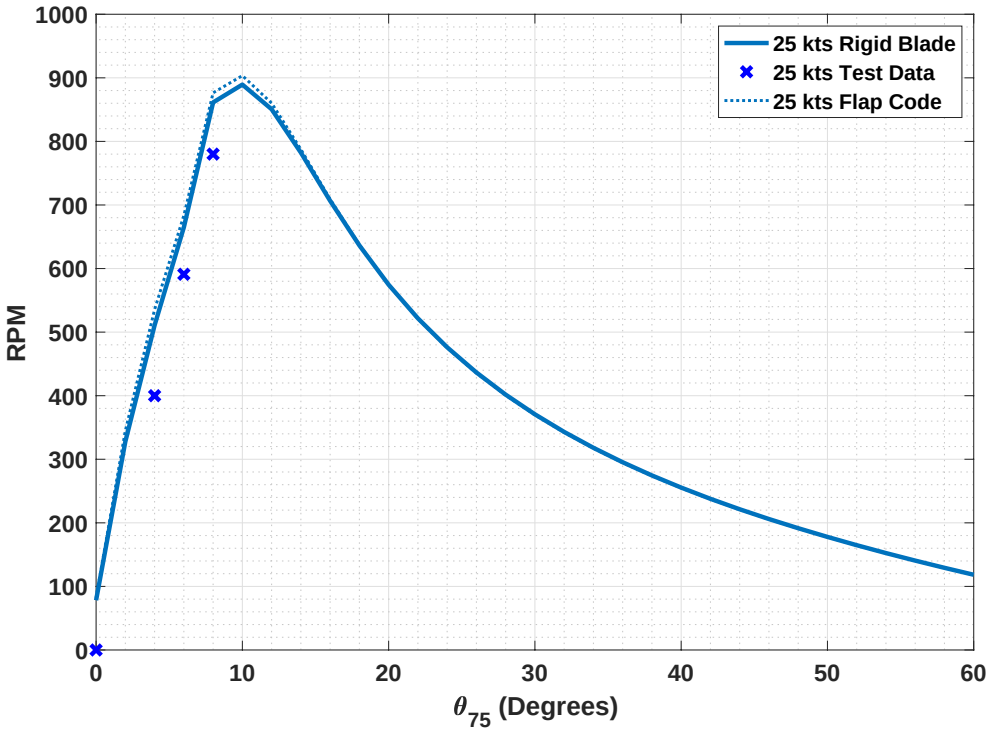

Figure 7.11: MTR freewheeling at 25 kts; prediction versus test; prediction with and without flapping motion

Both prediction lines are very similar on the left side of the curve, but they are identical for the right side of the curve. The peak is where the most difference between the rigid blade solution and the flexible flapping solution is, but only about +10 RPM is added to the peak.

The trim solution is then used for 25 knots, 35 knots, and 40 knots using rigid blade aerodynamics, shown in Figure 7.12. The collective is swept from $0 - 60°$ for all tunnel speeds as before. The CFD VR-7 airfoil deck, established as the correct deck, was used. The symbols show the same experimental data as Figure 7.2 earlier.

The lines are the predictions.

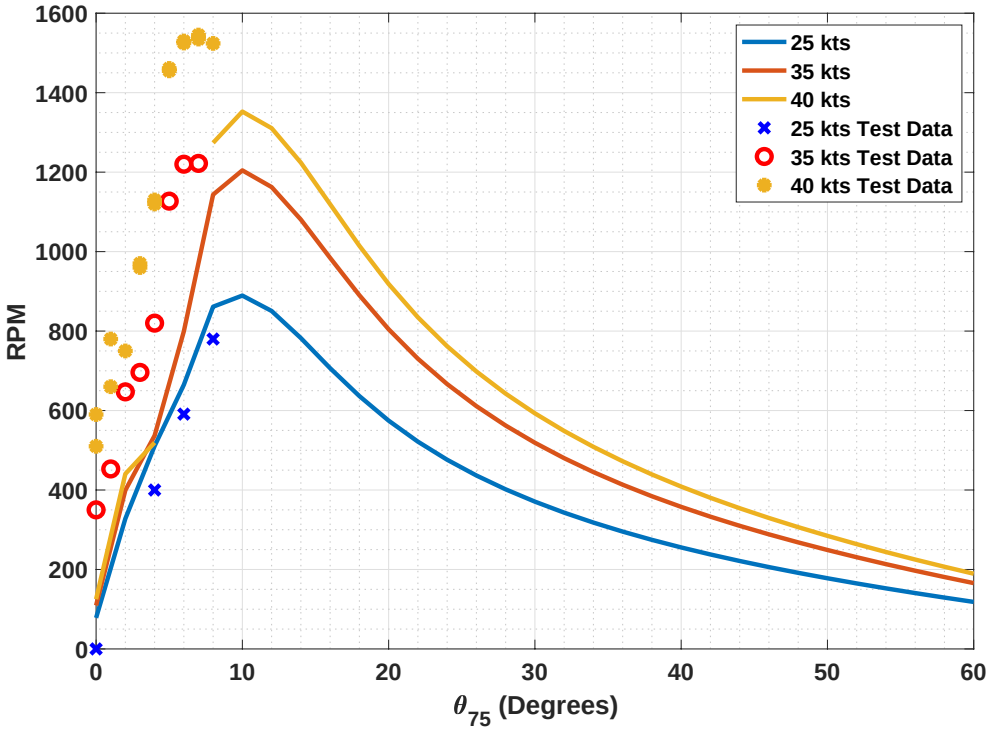

Figure 7.12: MTR freewheeling; prediction versus test

As can be seen in the plot, the 40 knots prediction does not converge from $4-6°$. As tunnel speed increases, the RPM for a given collective also increases. As tunnel speed increases, the trim predictions become further away from the experimental data and under-predict the experimental RPM for a given collective. The 25 knot prediction line begins at 100 RPM, increases until 10° where it peaks at 890 RPM, and then decreases in RPM until 60° where it ends at 100 RPM. The 35 knot prediction line begins at 100 RPM, increases until 10° where it peaks at 1200 RPM, and then decreases in RPM until 60° where it ends at 170 RPM. The 40 knot prediction line begins at 100 RPM, increases until 4° where it doesn't converge until 8°, continues increasing to 10° where it peaks at 1350 RPM, and then decreases in

RPM until 60° where it ends at 200 RPM.

The same trim solution is now predicted using the VR-7 Ames deck, shown as the dashed lines in Figure 7.13.

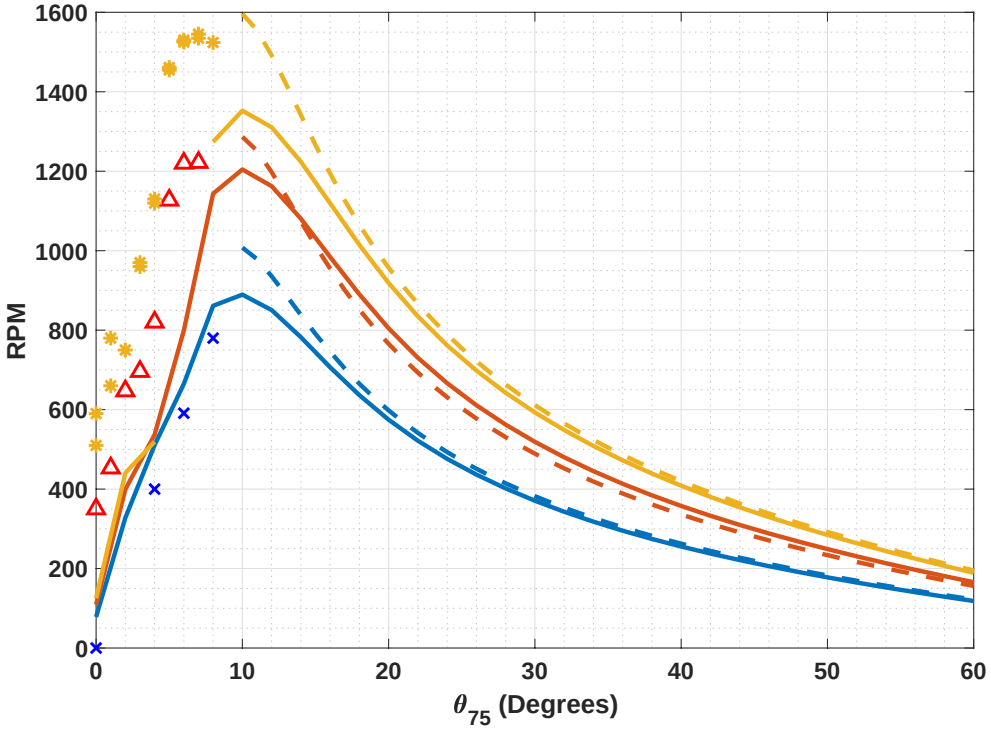

Figure 7.13: MTR freewheeling; prediction versus test; CFD and Ames airfoil decks

As in the 25 knots prediction (Figure 7.10), all tunnel speeds do not converge for $\theta_{75} < 10°$. The beginning of the predictions at 10° look as if it is curving, but does not fully form the peak as there is no convergence for the negative stall. Thus, the CFD airfoil deck is determined to be likely than the Ames airfoil deck.

To verify the flapping analysis, it is performed with the deflections forced to zero through a high stiffness input using only the aerodynamics. That data is compared to the rigid blade aerodynamic predictions in Figure 7.14.

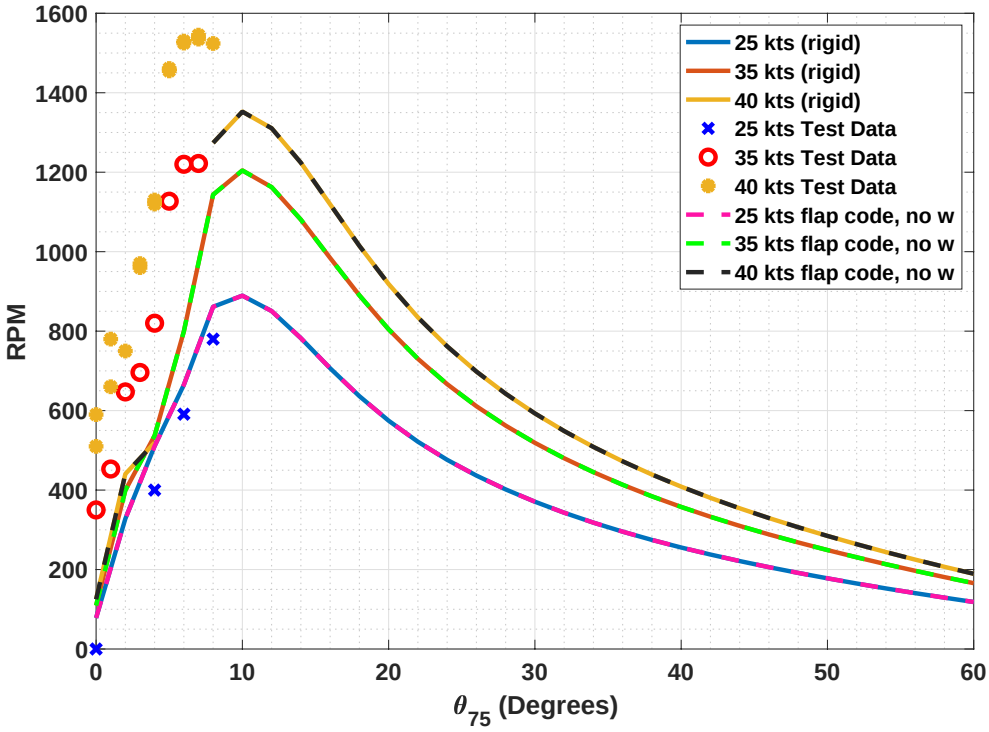

Figure 7.14: MTR freewheeling; predictions versus test; prediction with rigid blade and zero deflections

The flap code with deflections set to zero predictions fall exactly on top of the rigid blade aerodynamics predictions. This proves the flap code is working properly.

The deflections are then turned on ($w \neq 0$), and the trim solutions are predicted for all wind speeds. These predictions are shown in Figure 7.15. The flexible flap trim solutions are the dashed lines and the rigid blade aerodynamics solutions are solid lines.

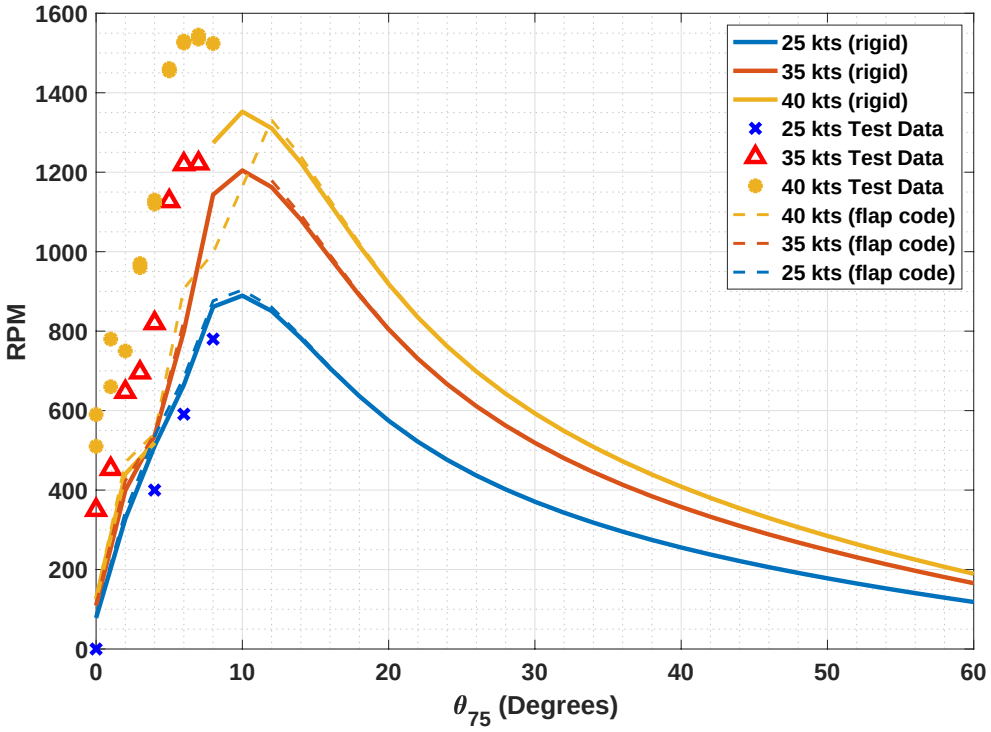

Figure 7.15: MTR freewheeling at 25 kts; prediction versus test; prediction with and without flapping motion

As in the 25 knots prediction (Figure 7.11), the 35 knots prediction is very close to the rigid blade aerodynamics prediction, with only a slight offset to the right of the peak. For 40 knots, the prediction is very close for $\theta_{75} \geq 12°$. At lower collectives, the flexible flap prediction has a lower offset than the rigid blade aerodynamic prediction. For 35 knots and 40 knots, for $\theta_{75} \leq 12$, the predictions are less smooth due to problems with convergence, a result of the negative angle of attack stall at those collectives.

In addition to aerodynamic predictions, the flap bending strain at $x = 0.4R$ is predicted for $\theta_{75} = 0 - 30°$ at 3 RPMs and 3 tunnel speeds (Figure 7.16). The blue lines represent 500 RPM, the red lines represent 1000 RPM, and the yellow

lines represent 1500 RPM. The solid lines of all colors represent a tunnel speed of 25 knots, the short dotted lines represent 35 knots, and the long dashed lines represent 40 knots. The strain is measured in $\mu\epsilon$.

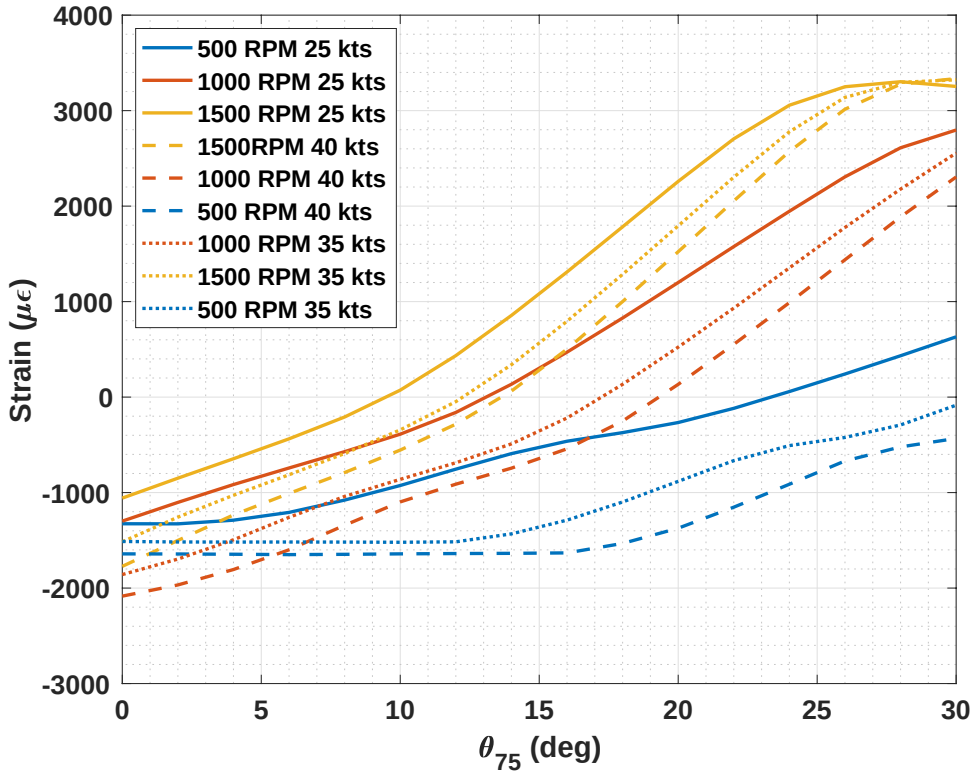

Figure 7.16: MTR flap bending strain Predictions at 0.4 R; pre-test predictions, no test data available yet

As wind speed increases for a given collective and RPM, the bending strains increase as well; however, before 5°, all bending strains are very similar for all RPMs and wind speeds. As the collective increases, for the a given RPM and wind speed, the bending strains increase. As RPM increases, for a given wind speed and collective, the bending strains are lower.

Chapter 8: Summary and Conclusions

This chapter summarizes the research performed, describes the key conlcusions, and highlights the main contributions of the research. It also envisions the future work that needs to be performed.

8.1 Summary

This thesis describes the development of the first set of Froude-scale tiltrotor blades for the MTR. The blades have a -37° twist/span, a VR-7 profile, a D-spar, and $\pm 45^\circ$ quasi-isotropic plies of carbon fiber. Titanium leading-edge weights bring the center of gravity to near the pitch axis at 0.25 c. The root cutout is until 0.263 R. The stiffness properties loosely follow the NASA-Bell XV-15 aircraft. The blades were instrumented and then integrated on the MTR in the Glenn L Martin Wind Tunnel and powered check out tests were conducted up to 2400 RPM ($M_{tip} = 0.53$) to test for tracking, balance, and structural integrity. Zero torque freewheeling tests were conducted to simulate future whirl flutter conditions. These tests produced 0-1500 RPM for $\theta_{75} = 0 - 8^\circ$ at various tunnel speeds. A flexible flapping rotor analysis was developed to understand the freewheeling condition and to predict the test data. The freewheeling condition is unique to proprotors and is where wind

tunnel tests are traditionally performed for whirl flutter, so it was the principal focus of the analysis.

8.2 Conclusions

It was established that high twist model-scale tiltrotor blades can be fabricated with good precision and tolerance for repeatability between blades.

Based on attempts to measure stiffness properties, the conclusion was made that an equivalent straight blade is best suited for measurements. The twisted blade presented many practical challenges for measuring accurate and repeatable structural properties and center of gravity. However, mass and non-rotating frequencies were easily measured on the twisted blade.

When preparing for integration to the MTR, it was important to have the blades balanced and blade tips colored in preparation for tracking. It was also very important to have a list of solutions to possible problems that might arise during the tests.

The flapping rotor analysis showed, for both the full FSD and the full MTR blades, that to obtain the best prediction, the 2D CFD airfoil deck (VR-7) must be used. The stall region, on the negative angle of attack, was crucial for freewheeling predictions. Using only linear aerodynamics (no airfoil tables), only one side of the freewheeling curve θ_{75} vs RPM was predicted. While this was the more relevant side, representative of cruise flight, the stall side was an excellent test case for analysis validation. The airfoil negative stall data created the peak and the full θ_{75} vs RPM

curve. The CFD deck predicted the experimental data much better than the Ames deck, so the CFD deck is considered more reliable. In addition, to have a complete model, flexible flapping motion was required. Even though aerodynamics alone was sufficient to predict the freewheeling RPM, the flexible flapping model would be essential for blade bending moments and strains in the future.

From the trim solution of the freewheeling analysis, it was shown that there are two collectives for each RPM— a low and a high collective. The lower collective represented the negative stall side. The higher collective represented the natural operation in cruise. The only experimental data obtained during the initial loads check out was on the lower collective side, which though not representative of a full-scale tiltrotor in cruise, provided a challenging validation test case. The actual whirl flutter data must be collected at the higher collective side.

8.3 Contributions

The main contributions of this work are listed as follows:

1. Fabrication of the first set of twisted model-scale tiltrotor blades at the Alfred Gessow Center. A twisted mold is sufficient with minor fine tuning of the layup process.

2. Observed accurate blade properties on a twisted blade still a challenge. The flap-lag coupling and their continuous variation across span makes it difficult to measure the change in slope accurately. Hence a suurogate straight blade is desired.

3. Analysis of tiltrotor freewheeling predictions must use an airfoil deck with good negative stall data, blade flapping, and zero torque RPM trim. The negative stall region of the airfoil deck is important particularly for the low collective region.

4. Discovered the correct collectives to operate in the future to simulate high-speed tiltrotor flight. There are two collective solutions for any RPM. The higher collectives should be used during whirl flutter tests.

8.4 Future work

Testing was cut short by COVID-19, and the effort was refocused towards pre-test analysis.

The future work for this research would be to first test at higher collectives to acquire accurate experimental data that is applicable to full-scale tiltrotor cruise. In addition to freewheeling test data, it is important to carry out whirl flutter tests since mitigating or eliminating whirl flutter is the principal objective of the MTR research. Frederick Tsai is working on this problem.

Future work also includes advanced blade shapes. James Sutherland is currently working on aft-swept blade tips. Another important geometry blade to explore will be a double swept blade, with fore- and aft-sweeps to control inertial and aerodynamic coupling to reduce control loads at the pitch links.

Finally, the analysis developed here, while an important first step, is still elementary, focused only on the freewheeling condition, with only flapping and 2D

airfoils. The analysis should be expanded to a full-fledged rotor model with wing and pylon dynamics and coupled with CFD. Seyhan Gül is currently working on this topic.

The blades developed in this thesis will serve as the baseline for the development and validation of all these future efforts and beyond.

Bibliography

[1] Hall, W. E., "Prop-Rotor Stability at High Advance Ratios," *Journal of the American Helicopter Society*, v 11, (2), April 1966, pp. 11-26.

[2] Gaffey T. M., "The Effect of Positive Pitch-Flap Coupling (Negative δ_3) on Rotor Blade Motion Stability and Flapping," *Journal of the American Helicopter Society*, v 14, (2), April 1969, pp. 49-67.

[3] Johnson, W., "Dynamics of Tilting Proprotor Aircraft in Cruise Flight," NASA TN D-7677, May 1974.

[4] Johnson, W., Lau, B. H. and Bowles, J. V., "Calculated Performance, Stability, and Maneuverability of High Speed Tilting Proprotor Aircraft," NASA TM 88349, September 1986; also in European Rotorcraft Forum 12, Garmisch-Partenkirchen, Germany, September 1986.

[5] Srinivas, V., Chopra, I., and Nixon, M. W. "Aeroelastic Analysis of Advanced Geometry Tiltrotor Aircraft," *Journal of the American Helicopter Society*, v 43, (3), July 1998, pp. 212-221.

[6] Srinivas, V. and Chopra, I., "Validation of a Comprehensive Aeroelastic for a Tiltrotor Aircraft," *Journal of the American Helicopter Society*, Vol. 43, No. 4, October 1998, pp. 333-341.

[7] Barkai, S. M. and Rand, O., "The Influence of Composite Induced Couplings on Tiltrotor Whirl Flutter Stability," *Journal of the American Helicopter Society*, v 43, (2), April 1998, pp. 133-145.

[8] Nixon, M. W. et al, "Aeroelastic Tailoring for Stability Augmentation and Performance Enhancements of Tiltrotor Aircraft," *Journal of the American Helicopter Society*, v 45, (4), October 2000, pp. 270-279.

[9] Acree, C.W., Peyran, R. J. and Johnson, W., "Improving Tiltrotor Whirl-mode Stability with Rotor Design Variations," European Rotorcraft Forum 26, Hague, The Netherlands, September 2000.

[10] Acree, C. W., "Effects of V-22 Blade Modifications on Whirl Flutter and Loads," *Journal of the American Helicopter Society*, v 50, (3), July 2005, pp. 269-278.

[11] Maisel, M. D., Guilianetti, D. J. and Dugan D. C., "The History of the XV-15 Tilt Rotor Research Aircraft: From Concept to Flight," NASA SP-2000-4517, 2000.

[12] Magee, J.P., et al, "Wind Tunnel Tests of a Full Scale Hingeless Prop/Rotor Design for the Boeing Model 222 Tiltrotor Aircraft." Report No. D222-10059-1, Contract NAS2-6505, April, 1973.

[13] Magee, J.P., and Alexander, H.R., "Wind Tunnel Test on a 1/4.622 Froude Scale, Hingeless Rotor, Tilt Rotor Model," NASA CR 151936, CR 151937, CR 151938, CR 151939, September 1976.

[14] Popelka, D., Sheffler, M., Bilger, J., "Correlation of Test and Analysis for the 1/5-Scale V-22 Aeroelastic Model," *Journal of the American Helicopter Society*, v 32, (2), April 1987, pp.21-33.

[15] Piatak, D.J., Kvaternik, R.G., Nixon, M.W., Langston, C.W., Singleton, J.D., Bennett, R.L., and Brown, R.K., "A Parametric Investigation of Whirl-Flutter Stability on the WRATS Tiltrotor Model," *Journal of the American Helicopter Society*, v 47, (2), April 2002, pp. 134-144.

[16] Nixon, M.W., et al, "Aeroelastic Stability of a Four-Bladed Semi-Articulated Soft-Inplane Tiltrotor Model," American Helicopter Society Annual Forum 59, May 6-8, 2003, Phoenix, AZ; see also 2003 International Forum on Aeroelasticity and Structural Dynamics, June 4-6, Amsterdam, The Netherlands.

[17] Matuska, D., Dale, A., and Lorber, P., "Wind tunnel test of a variable-diameter tiltrotor (VDTR) model," NACA CR 177629, 1994.

[18] Datta, A., Tsai, F., and Sutherland-Foggio, J. "Design of a New Tiltrotor Test Facility at the University of Maryland," 2019 American Institute of Aeronautics and Astronautics SciTech Forum, San Diego, California, January 7-11, 2019.

[19] Susan, G., Lopez, I. and Theodore, C, "NASA Technology for Next Generation Vertical Lift Vehicles," Paper AIAA 2015-0949, 56th AIAA/ASCE/AHS/ASC Structures, Structural Dynamics, and Materials Conference, Kissimmee, Florida, January 5-8, 2015.

[20] Stabellini, A., et al, "First NICETRIP Powered Wind Tunnel Tests Successfully Completed in DNW-LLF," AHS Annual Forum 70, Montreal, Quebec, Canada, May 20-22, 2014.

[21] Popelka, D., Sheffler, M., Bilger, J., "Correlation of Test and Analysis for the 1/5-Scale V-22 Aeroelastic Model," *Journal of the American Helicopter Society*, v 32, (2), April 1987, pp. 21–33.

[22] Ham, N. D., Bauer, P. H., Lawrence, T. H. and Yasue, M., "A Study of Gust and Control Response of Model Rotor-Propellers in a Wind Tunnel Airstream," NACA CR-137756, August 1975.

[23] Ham, N. D. and Whitaker, H. P., "A Wind-Tunnel Investigation of Tilt-Rotor Gust Alleviation System," NASA CR-152264, January 1978.

[24] Johnson, J. L. and Young, L. A., "Tilt Rotor Aeroacoustic Model Project," Confederation of European Aerospace Societies (CEAS) Forum on Aeroacoustics of Rotorcraft and Propellers, Rome, Italy, June 9-11, 1999.